Hybrid Superconducting/Ferromagnetic Thin Films for Super-Spintronics

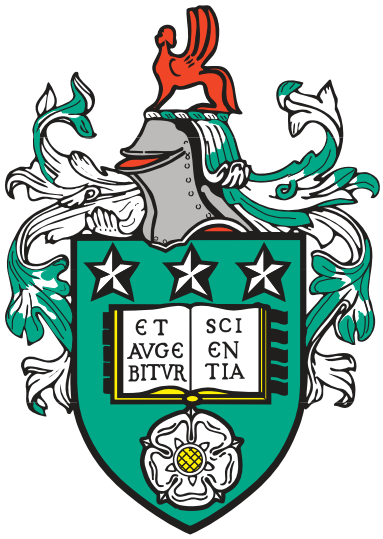

Nathan David Satchell

University of Leeds

School of Physics and Astronomy

Submitted in accordance with the
requirements for the degree of

Doctor of Philosophy

July 2016

For my parents

Intellectual Property Statement

The candidate confirms that the work submitted is his/her own, except where work which has formed part of jointly authored publications has been included. The contribution of the candidate and the other authors to this work has been explicitly indicated below. The candidate confirms that appropriate credit has been given within the thesis where reference has been made to the work of others.

Work from the following jointly authored papers is in this thesis:

"Remotely induced magnetism in a normal metal using a superconducting spin-valve" M. G. Flokstra, N. Satchell, J. Kim, G. Burnell, S. J. Bending, P. J. Curran, S. Langridge, C. J. Kinane, J.F.K. Cooper, M. Eschrig, A. Isidori, N. Pugach, H. Luetkens, A. Suter, T. Prokscha, and S. L. Lee *Nature Physics* ***doi:10.1038/nphys3486****, (2015).*

This work forms the muon experimental work in chapter 6.

- **Work attributed to the candidate**: Sample prep, development and deposition. Experimental work at LEμSR beamline.
- **Work attributed to others**: M. G. Flokstra: Experimental work at LEμSR beamline. Data analysis and simulations. J. Kim: Sample deposition. J.F.K. Cooper: Experimental work at LEμSR beamline. G. Burnell: Support and management for N Satchell and J Kim. Discussion and initial sample design. M. Eschrig, A. Isidori and N. Pugach: Theoretical modelling. H. Luetkens, A. Suter and T. Prokscha: Support on LEμSR beamline. S. J. Bending and P. J. Curran: sample characterisation. S. Langridge and C. J. Kinane: Support and management for N Satchell and J.F.K. Cooper. S. L. Lee: Overall management of project.

"Irreversible magnetization switching at the onset of superconductivity in a superconductor ferromagnet hybrid" P. J. Curran, J. Kim, N. Satchell, G. Burnell, M. G. Flokstra, S. L. Lee, J.F.K. Cooper, C.J. Kinane, S. Langridge, A. Isidori, N. Pugach, M. Eschrig, and S. J. Bending *App. Phys. Lett.* ***107****, 262602 (2015)*

This work forms the interpretation of work in chapter 6, but is not explicitly presented in the results chapter. The findings of this work are presented as part of the literature review in chapter 2.

- **Work attributed to the candidate**: Sample prep, development and deposition.
- **Work attributed to others**: P. J. Curran: Scanning Hall Probe experimental work and analysis. J. Kim: Sample deposition. M. Eschrig, A. Isidori and

N. Pugach: Theoretical input. G. Burnell, M. G. Flokstra, S. L. Lee, J.F.K. Cooper, C.J. Kinane and S. Langridge: Support and input to the manuscript. S. J. Bending: Overall management of project. Interpretation of SHP data.

"Controlled suppression of superconductivity by the generation of polarized Cooper pairs in spin-valve structures" M. G. Flokstra, T. C. Cunningham, J. Kim, N. Satchell, G. Burnell, P. J. Curran, S. J. Bending, C. J. Kinane, J. F. K. Cooper, S. Langridge, A. Isidori, N. Pugach, M. Eschrig, and S. L. Lee *Phys. Rev. B* ***91****, 060501 (2015) (Editors' Suggestion)*

This work forms the interpretation of work in chapter 6, but is not explicitly presented in the results chapter. The findings of this work are presented as part of the literature review in chapter 2.

- **Work attributed to the candidate**: Sample prep, development and deposition. Interpretation and analysis.
- **Work attributed to others**: M. G. Flokstra: Experimental work, analysis, writing of manuscript. T. C. Cunningham: Initial measurements. J. Kim: Sample deposition. M. Eschrig, A. Isidori and N. Pugach: Theoretical modelling. S. J. Bending and P. J. Curran: sample characterisation. S. Langridge and C. J. Kinane: Support and management for N Satchell and J.F.K. Cooper. S. L. Lee: Overall management of project.

"Magnetic phases of sputter deposited thin-film erbium" J. D. S. Witt, J. F. K. Cooper, N. Satchell, C. J. Kinane, P. J. Curran, S. J. Bending, S. Langridge, L. J. Heyderman, and G. Burnell *Submitted to Scientific Reports*

This work is included in the first half of chapter 4.

- **Work attributed to the candidate**: Sample prep, materials development, all depositions, neutron experimental work and interpretation, initial x-ray, transport and magnetometry data.
- **Work attributed to others**: J. D. S. Witt: Final magnetometry and transport data, interpretation. J. F. K. Cooper, C. J. Kinane, P. J. Curran and S.

Langridge: Support experimental work on neutron beamline. L. J. Heyderman: Supervision for J. D. S. Witt. G. Burnell: Overall management of project. Supervision for N. Satchell and J. D. S. Witt.

"Revealing the Spiral Magnetic Phase in 6 nm Textured Erbium using Polarised Neutron Reflectometry" N. Satchell, J. D. S. Witt, G. Burnell, P. J. Curran, C. J. Kinane, S. Langridge and J. F. K. Cooper *Submitted to Journal of Physics: Condensed Matter*

This work is included in the second half of chapter 4.

- **Work attributed to the candidate**: Sample prep, materials development, all depositions, neutron experimental work and interpretation, x-ray experimental work, initial magnetometry data, writing of manuscript.
- **Work attributed to others**: J. D. S. Witt: Final magnetometry data, assitance in the interpreatation of data. J. F. K. Cooper, C. J. Kinane, P. J. Curran and S. Langridge: Support experimental work on neutron beamline. G. Burnell: Overall management of project. Supervision for N. Satchell and J. D. S. Witt.

Acknowledgements

Firstly, I would like to thank my supervisors, Dr. Gavin Burnell and Prof. Sean Langridge, for all the advice and support they have given me during this work. I am especially thankful for Gavin's general love of all things superconducting, which at times provided much needed motivation, and his willingness to write the software needed for my measurements.

I am extremely grateful for all the help and support received from the Condensed Matter group at Leeds. From invaluable feedback during the group meetings, to the equally important discussions over a pint in the Fenton, it has been a privilege to work in such a collaborative and friendly environment. Special thanks must be paid to Dr. Mannan Ali. Without him the group wouldn't function. Also to Dr. Nicholas Porter and Dr. Mark Elkin for providing support and training early in my PhD.

During this work I spent many late nights counting muons and neutrons with Dr. Machiel Flokstra, Prof. Steve Lee, Dr. Jos Cooper and Dr. Christy Kinane. Without their good company, collective knowledge and experimental assistance this thesis would have never been finished. I must also thank the other members of the SFM Consortium; Dr. Peter Curran, Prof. Simon Bending, Dr. Aldo Isidori, Prof. Matthias Eschrig, Dr. Jangyong Kim and especially Dr. James Witt.

My insatiable helium thirst was somehow always met by Luke Bone, Brian Gibbs, John Turton and the late Phil Cale. Additionally, John Turton's ability to find the right tools and fittings to fix almost anything has been a huge help during my PhD.

On a personal note, I must thank all the friends I have made along the way. My time in Leeds simply wouldn't have been the same without all of you. Special thanks must go to my office mate Philippa, and Joe, Sophie, Rowan, May and Dan, who have particularly got me through the ups and downs.

Abstract

This thesis examines the interaction between superconductivity and inhomogeneous ferromagnetism. Through careful engineering of the interface, it is possible to unlock a new spin aligned triplet Cooper pair, which is capable of penetrating and modifying the magnetisation of a ferromagnet in proximity to a singlet, *s*-wave, BCS, superconductor. This triplet state is the building block for the new class of super-spintronic devices.

Two candidate ferromagnetic systems in which to study the spin aligned triplet are considered. Firstly, the rare-earth ferromagnet erbium is fabricated using sputter deposition. Neutron diffraction measurements show the retention of the conical magnetic state in the thin film form for the first time. This conical state makes it an ideal candidate material for triplet Cooper pair generation. Placing erbium next to superconducting niobium has a drastic effect on the critical temperature of the superconductor, causing a suppression and oscillation of T_c with erbium thickness. In addition the remanent state of erbium at a single thickness can be used as a control to switch the niobium from the superconducting state into the normal state.

The second system studied is the superconducting spin valve. In this system the inhomogeneity is engineered in a multi-layer structure using exchange biased Co. To study the nature and extent of the triplet Cooper pair in this structure, large scale facility techniques are employed to look for expected changes to the magnetic state of the heterostructure, with the onset of superconductivity. Surprisingly, no observation directly attributable to the triplet Cooper pair was observed. Instead a new type of induced ferromagnetism in a normal metal coupled to the superconducting spin valve was discovered.

Abbreviations

S	Superconductor	LRTC	Long Range Triplet Component
F	Ferromagnet	SRTC	Short Range Triplet Component
N	Normal Metal	T_c	Superconductor's Critical Temperature
P	Parallel	T_{Curie}	Curie Temperature
AP	Antiparallel	VSM	Vibrating Sample Magnetometer
Perp	Perpendicular	JJ	Josephson Junction
VTI	Variable Temperature Insert	SQUID	Superconducting Quantum Interference Device
XRR	X-ray Reflectometry	PNR	Polarised Neutron Reflectometry
XRD	X-ray Diffraction	ND	Neutron Diffraction
LEμSR	Low Energy Muon Spin Rotation	FFLO	Fulde Ferrell Larkin Ovchinnikov
CAR	Crossed Andreev Reflection	EC	Elastic Co-Tunnelling
BCS	Bardeen Cooper Schrieffer	GL	Ginzburg Landau
RE	Rare Earth	RMS	Root Mean Square

CONTENTS

Chapter 1

Introduction

Work on this thesis began in 2012. In that year the world produced 22,202 TWh of electricity [1]. In the same year the ICT ecosystem used 1,500 TWh, or about 7% of all electricity produced (at a conservative estimate) [2]. Fossil fuels accounted for 80% of total energy supply, where some of the largest cloud computing providers source over 50% of their electricity from coal power stations (considered to be the most polluting of all commercial energy supplies) [3].

The dissipation of heat in traditional silicon (CMOS) based electronics is a major source of inefficiency in energy usage. Superconductors are, by nature, dissipationless. Computing via logic circuits based on Josephson junctions is also faster (circuits operating at 770 GHz were shown in the 90's) [4]. Even including refrigeration, the earliest test circuits did not require more power than conventional technologies [5]. The increased efficiency of both chip design and refrigeration over the last 20 years have made superconducting computers orders of magnitude more efficient than their conventional counterparts. Where efficiency is presented in gigaFLOP (floating-point operations) per Joule, the most efficient supercomputers achieve 2 GFLOP/J, while an equivalent superconducting computer could deliver 500 GFLOP/J [5]. While not practical for the average home or office user, adoption of superconducting technologies for cloud and supercomputers could significantly increase processor speed and reduce the power consumption of ICT systems. The largest remaining problem to building such a computer is low-temperature memory, which is not as well developed as logic circuits. To achieve the promised increase in efficiency, a new type of low-temperature memory architecture is needed.

While traditionally considered competing phenomena, when artificially juxtaposed there is a wealth of physics at the interface between superconductors and ferromagnets. By placing an inhomogeneous magnetic texture at the superconductor/ferromagnet interface, it is possible to create the so-called long ranged triplet component (LRTC) or finite spin Cooper pair. This Cooper pair has both electron spins aligned in the same direction, hence creating a dissipationless spin current. The LRTC is less susceptible to magnetic scattering and can therefore penetrate further into a proximitised ferromagnetic layer [6]. The LRTC is the manifestation of complete synergy between the otherwise antagonistic phenomena.

Spintronics (spin transport electronics) aims to take advantage of the electrons spin degree of freedom (in addition to charge) in order to perform logic operations. In doing so logic operations controlled by spin currents can be performed faster and with greater energy efficiency than the charge only CMOS technologies [7].

Incorporation of superconductors into spintronic device structures opens the exciting possibility of performing logic operations on a dissipationless spin current [6]. This new field is given the portmanteau super-spintronics [8]. Three such mechanisms have been proposed. The injection of a normal spin current into a superconducting logic gate [9, 10]. Extracting spin polarised LRTC Cooper pairs for injection into established spintronic logic gates [11]. Or a new class of all superconducting logic circuits via magnetic Josephson junctions [12, 13].

In addition to performing logic operations, spintronics has found application as magnetic sensors in the read heads of hard disk drives. Several breakthroughs in complex heterostructures containing superconducting and ferromagnetic elements show promise as potential cryogenic memory elements. In such a scheme, information could be stored by the state of the system (superconducting or normal) where the T_c of the superconductor can be tuned [14]. It is also possible to store information in the phase difference between two superconducting layers in a 0-π Josephson junction [13, 15–17] or two such junctions coupled as a SQUID [18].

1.1 Thesis Outline

As the field of super-spintronics is still in its infancy, the experimental work as part of this thesis attempts to address two aims. The first aim is the characterisation and incorporation into devices of new candidate ferromagnetic materials. The second aim is to examine the nature of the LRTC and interactions at the S/F interface in the prototypical super-spintronic device, the superconducting spin valve.

In chapter 2, a theoretical overview of ferromagnetism and superconductivity is presented, as well as the theoretical description of proximity effects between the two phenomena. A detailed literature review of experimental developments in the field of super-spintronics follows.

Chapter 3 details the experimental procedures used throughout this thesis, as well as a discussion of how techniques can be combined to provide a complete description of a samples properties.

The rare-earth ferromagnet erbium is sputter deposited onto heated substrates in chapter 4. The characterisation of the films using lab based as well as facility based neutron diffraction and reflectometry show that a conical ferromagnetic state is retained in the thin film for the first time.

In chapter 5, erbium is incorporated into superconducting devices. Placing erbium next to superconducting niobium has a drastic effect on the critical temperature of the superconductor, causing a suppression and oscillation of T_c with erbium thickness of over 2.5 K. In addition, the remanent state of erbium at a single thickness is used as a control to switch the niobium from the superconducting state into the normal state. These two control mechanisms make it a promising candidate material for low temperature memory devices.

The superconducting spin-valve is studied in chapter 6. In this device, control of the magnetic state of the two F-layers in an S/F/F or F/S/F heterostructure can be used to tune the generation of the LRTC [19–22]. The generation of the LRTC—opening an additional "leakage" channel for Cooper pairs—is believed to result in the lowering of the T_c of the system. Neutron and muon techniques are employed to search for expected changes to the magnetic state of the heterostructure, with the onset of triplet superconductivity. Surprisingly, no observation directly attributable to the LRTC is observed. Instead a new type of induced ferromagnetism is seen inside a normal metal coupled to the heterostructure.

Finally in chapter 7 all the results from experiments are summarised. An outlook for future experimental work is also presented.

CHAPTER 2

Background Theory and Literature Review

2.1 Introduction

This chapter aims to offer a brief introduction to the theories of magnetism and superconductivity. The mechanism of ferromagnetism in the itinerant metals is introduced. The relevant phenomenological theories of superconductivity, as well as the microscopic theory and important results are discussed. The interplay of proximity effects at the superconductor/ferromagnet interface is outlined theoretically followed finally by a detailed review of recent theoretical and experimental advances in this field.

The theory and application of magnetism and magnetic materials is covered in detail in the books of Ashcroft & Mermin [23] and Blundell [24]. The theory and application of superconductivity is covered in detail in the books of Tinkham [25] and Annett [26].

2.2 Magnetism

"The study of magnetism is possibly the second-oldest profession in the world. Unlike the oldest, interest has waxed and waned over the centuries" [27]. Recent advances in spintronics have lead to renewed interest in ferromagnetism as a source of spin polarised carriers. A ferromagnet has a spontaneous magnetisation even in the absence of an applied field. In this section the mechanism for ferromagnetism for the itinerant ferromagnets is outlined. The rare earth ferromagnet erbium is introduced in Chapter 4 where the mechanism for its conical ferromagnetism is also discussed.

Materials which do not exhibit magnetic ordering fall broadly into two categories, diamagnetic and paramagnetic, governed by the sign of their magnetic susceptibility (χ) where the magnetisation $\mathbf{M}$ of the material induced by an applied magnetic field $\mathbf{H}$ is given by $\mathbf{M} = \chi\mathbf{H}$. When χ is negative the material exhibits diamagnetism. That is, the magnetic field induces magnetic moment which opposes the applied field which caused it. Of particular interest is the description of bulk superconductors as 'perfect diamagnets' with $\chi = -1$. Physically this means the superconductor will expel all flux from inside it, an effect called Meissner screening.

Paramagnetism corresponds to a positive susceptibility so that the applied field induces magnetisation which aligns parallel with the applied field which caused it. Typically these materials have unpaired electrons which, in the absence of a field, point in random directions. An external field can line up these electrons inducing a net magnetisation along the field direction.

2.2.1 Exchange Interaction

The exchange interaction is the fundamental reason for spontaneous alignment of spins along a common direction in a ferromagnet. As a result of the Pauli exclusion principle for fermionic electrons, spins which are aligned parallel cannot occupy the same spatial state as one another. For fermions the total wave function must be antisymmetric.

In the simplest case, consider only two electrons with spacial coordinates $\mathbf{r}_1$ and $\mathbf{r}_2$ respectively. The two individual electron states are $\psi_a(\mathbf{r}_1)$ and $\psi_b(\mathbf{r}_2)$. The wave function of the joint state cannot be a product of the two states, as the product state does not obey exchange symmetry. Therefore, the only states which are allowed are a antisymmetric spin, symmetric spatial (S=0, singlet) or a symmetric spin, antisymmetric spatial (S=1, triplet) combination of the product.

Therefore, the total wave function for the singlet Ψ_S and triplet Ψ_T can be written as [24]:

$$\Psi_S = \frac{1}{\sqrt{2}}[\psi_a(\mathbf{r}_1)\psi_b(\mathbf{r}_2) + \psi_a(\mathbf{r}_2)\psi_b(\mathbf{r}_1)]\chi_S \tag{2.1a}$$

$$\Psi_T = \frac{1}{\sqrt{2}}[\psi_a(\mathbf{r}_1)\psi_b(\mathbf{r}_2) - \psi_a(\mathbf{r}_2)\psi_b(\mathbf{r}_1)]\chi_T \tag{2.1b}$$

Assuming that both the spin parts are normalised the difference in the electrostatic energies of the two states is:

$$E_S - E_T = 2\int \psi_a^*(\mathbf{r}_1)\psi_b^*(\mathbf{r}_2)V\psi_a(\mathbf{r}_2)\psi_b(\mathbf{r}_1)d\mathbf{r}_1 d\mathbf{r}_2, \tag{2.2}$$

where V denotes the potential due to the Coulomb interaction. This difference in energy is an electrostatic term due to the exchange of two identical particles and is used to define the exchange constant:

$$J = \frac{E_S - E_T}{2}. \tag{2.3}$$

The Heisenberg model provides a way to generalise the interaction to all neighbouring atoms, such that the exchange interaction between two spins i and j ($\mathbf{S}_i, \mathbf{S}_j$) is given by the Heisenberg Hamiltonian:

$$E_{Ex} = -2J\mathbf{S}_i \cdot \mathbf{S}_j. \tag{2.4}$$

Stoner showed that if the gain from this exchange energy is greater than the increase in kinetic energy from altering the band structure, a spontaneous magnetisation would occur

[28]. This becomes stable when the product of the exchange constant and the density of states at the Fermi surface $N(\epsilon_F)$ is greater than one and is known as the Stoner criterion:

$$JN(\epsilon_F) > 1 \tag{2.5}$$

In the transition metals, the 3d electrons form a narrow band with a large density of states. The complex structure within this 3d band means that only three elements Fe, Co and Ni have peaks in $N(\epsilon_F)$ at, or sufficiently near, ϵ_F, which fulfils the Stoner criterion at room temperature.

2.2.2 Domains and Domain Walls

A ferromagnet typically contains many small regions called domains, within which the local magnetisation reaches the saturation value. The direction of the magnetisations of different domains need not be parallel, and in fact the most energetically favourable alignment is often not parallel. This is due to the breakup into domains being favourable to satisfy demagnetisation effects. The application of an applied field will counteract this, and work to align the domains. The domain wall is the most basic type of magnetic inhomogeneity, the topic of magnetic inhomogeneity and its interaction with superconductivity will be considered in detail in this work.

The domain wall is the region which connects adjacent domains. Domain walls can be classified according to the angle between the magnetisation of the two domains. A 180° domain wall separates antiparallel magnetisations, a 90° domain wall separates perpendicular magnetisations. In a thin film where competition between competing electronic orders becomes more prevalent, more complicated magnetic structures can form. In-plane magnetic films of the type used in this work can form 360° domain walls at defect sites, or around individually pinned moments. In general is not uncommon to expect some combination of domain walls, defects, vortices, dislocations and other singularities in a film. Huge amounts of work has been undertaken to characterise such features, with the aim of incorporation into magnetic storage devices. A review of this field can be found in reference [29].

2.3 Superconductivity

As is traditional in all PhD theses on superconductivity, it is noted that H. Kamerlingh Omnes is credited with the discovery of superconductivity in 1911, while cooling mercury to liquid

He temperatures [30]. Next the two properties most identifiable with superconductivity are stated: zero resistivity and perfect diamagnetism. In this section successful phenomenological theories and their associated length scales are defined, as these results are of particular relevance to practical situations. To give validation of the phenomenological theories, the microscopic theory is introduced. Finally, the specific extension of triplet superconductivity to this theory and its consequences are discussed. For more detail on this section the books of Annett [26] and Tinkham [25] are recommended.

Before proceeding it is worthwhile defining the two typical length scales used throughout this work. Firstly the coherence length (ξ) which characterises the distance over which superconductivity can vary without undue energy increase. Physically this length scale can be considered the effective size of the superconducting Cooper pair. This is also the length scale associated with the proximity effect. Secondly the penetration depth (λ) which characterises the distance taken for superconductivity to recover to bulk behaviour away from a perturbation, physically this perturbation could be a vortex core. λ is the length scale associated to the Meissner effect, and is hence often referred to as the magnetic screening length.

2.3.1 Phenomenological Theories

While the microscopic theory of Bardeen, Cooper and Schrieffer (BCS) provides a detailed description for the underling mechanism of superconductivity, it is the independently developed phenomenological theories that most accessibly describe the macroscopic behaviour of superconductors.

The London Equation

The first theory to account for the Meissner effect was developed by the London brothers in 1935 [31]. They assumed some fraction of conduction electrons become superfluidic with the others remaining normal. Those with superfluid properties can carry the dissipationless current. The London equation links the critical current density inside a superconductor, **j**, to the magnetic vector potential, **A**, via the London parameter, Λ,

$$\mathbf{j} = -\mathbf{A}/\Lambda, \tag{2.6}$$

and

$$\Lambda = \frac{m_s}{n_s e^2}, \tag{2.7}$$

where e, n_s and m_s are the charge, number density and mass of the superfluid electrons respectively.

Considering the London equation and Ampère's circuital law, spatially inside a superconductor an external field $\mathbf{B}_0$ will vary as

$$\mathbf{B}(x) = \mathbf{B}_0 \exp\Big(-\frac{x}{\lambda_L}\Big), \tag{2.8}$$

where λ_L is the London penetration depth, or the distance over which the external magnetic field is screened. λ_L can be related back to London parameter as

$$\lambda_L = \left(\frac{\Lambda}{\mu_0}\right)^{1/2}. \tag{2.9}$$

The Ginzburg-Landau Theory

For cases where the superconducting condensate is not constant in space, for example in proximity effects, the microscopic BCS theory becomes very difficult to apply. In these situations it is the solutions to the Ginzburg-Landau (G-L) theory which are more readily applicable. For macroscopic behaviour it is the free energy of the system which holds information about the critical fields and the spatial structure of superconductivity. While classically considered a phenomenological description of superconductivity, the work of Gor'kov showed that the theory was derivable as a limiting case of the full BCS theory [32].

The G-L theory is an extension to the Landau theory of second order phase transitions. Substituting the complex Ψ for the order parameter Q, where Ψ is the G-L order parameter, one first meets the G-L free energy functional [25]

$$\Delta G = \alpha\Psi^*\Psi + \frac{\beta}{2}\big(\Psi^*\Psi\big)^2 + \frac{1}{2m_s}\left[\left(\frac{\hbar}{i}\nabla - e^*\mathrm{A}\right)\Psi\right]^2 + \frac{1}{2\mu_0}B_m^2, \tag{2.10}$$

where ΔG is the change in energy of the phase transition, α and β are values to be found, $\Psi^*\Psi = n_s$ the density of superconducting charge carriers, m_s and e^* are the mass and charge of the carriers (now known to be the Cooper pair so $2m_e$ and $2e$) and B_m is the flux to cancel applied magnetic field.

When fields and gradients are absent and we consider T close to T_c [25]

$$\Delta G = \alpha \Psi^* \Psi + \frac{\beta}{2}\left(\Psi^* \Psi\right)^2, \tag{2.11}$$

where β is necessarily positive (to avoid divergence). For $\alpha < 0$ the minimum in free energy occures when $\Psi^* \Psi = 0$, that is the condensate is non-existant and the material is in the normal state. For $\alpha > 0$ the minimum occurs when $\Psi^* \Psi = -\alpha/\beta$, which describes a uniform superconducting state of lower overall free energy.

By considering the case where Ψ may not be uniform everywhere, and instead imposing fields, currents, or gradients one can minimise the G-L free energy functional with respect to Ψ (or Ψ^*) or A, the magnetic vector potential. This leads to the two G-L differential equations [25]

$$\alpha \Psi^* \Psi + \frac{\beta}{2}\left(\Psi^* \Psi\right)^2 + \frac{1}{2m_s}\left[\left(\frac{\hbar}{i}\nabla - e^* \mathrm{A}\right)\right]^2 \Psi = 0 \tag{2.12}$$

and

$$\mathrm{J}_s = \frac{i e^* \hbar}{2m_s}\left[\Psi^* \nabla \Psi - \Psi \nabla \Psi^*\right] - \frac{e^{*2}\mathrm{A}}{m_s}\Psi^* \Psi, \tag{2.13}$$

respectively, where Ψ now varies in space with $\Psi(\mathbf{r}) = |\Psi(\mathbf{r})|\mathbf{e}^{\mathbf{i}\varphi(\mathbf{r})}$.

From these two differential equations it is possible to come to useful experimental parameters which are used throughout this work. Where a coherence length or penetration depth are referred to, they correspond to the following G-L results [25]

$$\xi_{GL} = \sqrt{\frac{\Phi_0}{2\pi H_{c2}}} \tag{2.14}$$

and

$$\lambda_{GL} = \sqrt{\frac{m_s}{\mu_0 n_s e^{*2}}} \tag{2.15}$$

where H_{c2} is the upper critical field and Φ_0 the flux quantum. These two quantities are linked by the dimensionless $\kappa = \lambda_{GL}/\xi_{GL}$. If $\kappa < 1/\sqrt{2}$ the superconductor is defined as type I. When $\kappa > 1/\sqrt{2}$ the superconductor is type II [26]. While determining an estimate for ξ_{GL} is simple, determination of λ_{GL} is typically performed with muon spin rotation experiments. To give some typical numbers for thin film polycrystalline Nb, at T well below T_c, $\xi_{GL} \approx 10$ nm and $\lambda_{GL} \approx 90$ nm [33, 34]. This gives $\kappa = 9$ and makes thin film Nb type II.

2.3.2 Bardeen, Cooper and Schrieffer (BCS) Theory

In 1957, Bardeen, Cooper and Schrieffer proposed a microscopic model of superconductivity [35, 36]. The principle is that in a metal, electrons with an energy near the Fermi energy could form a bound state and condense to a lower energy level. This bound state of the electrons is referred to as a Cooper pair after the 1956 work of Cooper showing that two electrons, which were added to a metal above the Fermi surface, could become bound through the phonon mediated interaction [37].

Cooper Pairs

The physical explanation to support this attractive force between electrons comes by considering the motion of ions in the lattice. In a simple view, the first electron in the pair polarises the medium by attracting positive ions towards it. The first electron moves from this site leaving excess ions, which in turn attract the second electron in the pair. When this interaction is strong enough to overcome the repulsive Coulomb interaction, a net attractive force between the electrons is created and hence the superconducting state is formed. As a solid is necessarily stiff and ions cannot significantly be moved, this electron-electron interaction is mediated instead by virtual lattice vibrations (phonons) rather than the physical displacement of ions.

The consequence of this new bound pair of electrons is the shift from the behaviour of individual spin 1/2 Fermions to a sea of new Cooper pairs which can be treated approximately with Bose-Einstein statistics. The most notable property of this new electron sea is the ability to exist at the same energy level.

The Superconducting Gap

In a superconductor there exists a gap in the distribution of energy levels available to the electrons. The superconducting electrons exist with a lower energy than the Fermi energy. The consequence of this is that a finite amount of energy, Δ, must be supplied to excite the electron. This means, to break a Cooper pair, Δ must be applied to each electron in the pair. If a Cooper pair is broken, then two electrons are created, but the first available state for these Fermionic electrons is above the Fermi energy. Δ is described the same way as the macroscopic function Ψ in the G-L theory, the value of Δ increases with decreasing temperature, i.e. the higher the T_c a material has the larger Δ will be at 0 K. The existence of this energy gap places an upper limit in the BCS theory on T_c of about 30 K. Any higher than

this and thermal fluctuations are much larger than the size of Δ. At T_c, $\Delta = 0$. Physically this means it is no longer energetically favourable for electrons to form Cooper pairs. The gap can be defined as [26]

$$2\Delta_{0K} = 3.53 k_B T_c, \tag{2.16}$$

independent of material, under the assumption that the mechanism for superconductivity in the material has *s*-wave symmetry. For these conventional superconductors at temperatures T<T_c, the value of Δ is large enough to prevent the normal scattering events which would give rise to electrical resistance.

2.3.3 Triplet Superconductivity

The BCS theory assumes the electron-electron interaction is via isotropic virtual phonons. If virtual phonons are involved then the spatial part of the wavefunction for the pair should have a maximum when the separation is close to zero. This implies a symmetric spatial wavefunction. But, overall the wavefuncton must be antisymmetric on particle exchange due to the electrons in the Cooper pair both being Fermions. Therefore the spin part must also be antisymmetric leading to the description of BCS superconductivity as spin singlet and the writing of the wavefunction as,

$$|\Psi\rangle = |0,0\rangle = \frac{1}{\sqrt{2}}\big(|\uparrow\downarrow\rangle - |\downarrow\uparrow\rangle\big). \tag{2.17}$$

It is now known that this is not the only symmetry that can sustain a superconducting condensate and the study of unconventional non-BCS superconductivity is a very active field. Unconventional superconductors can form the superconducting state with essentially identical properties as the conventional superconductors. This is because properties such as Meissner screening and zero-resistivity are dependent on the macroscopic coherence of the state, rather than the specific mechanism which allows the state to form.

The symmetric spin-triplet states, $|\uparrow\downarrow + \downarrow\uparrow\rangle$, $|\uparrow\uparrow\rangle$ or $|\downarrow\downarrow\rangle$ are found in only a handful of superconductors, where Sr_2RuO_4 is currently the best candidate material [38]. In these materials the antisymmetry requirements are satisfied by the condensates of these superconducting materials being spatially antisymmetric, that is, odd in angular momentum (l). These materials exhibit spatially anisotropic superconductivity and the condensate is therefore highly susceptible to crystallographic irregularities, impurities and non-magnetic scatter-

ing. For these reasons fabrication in thin film form is highly difficult and hence the system is not a candidate for potential device applications.

The type of superconductivity studied in this thesis is the spin aligned triplet state ($|\uparrow\uparrow\rangle$ or $|\downarrow\downarrow\rangle$). The processes by which this state is generated will be considered later, but for now the meaning of this state is considered. The spin aligned triplet state exists with quantum numbers l=0 and S=1, however under the Pauli Exclusion Principle it appears forbidden. In order to overcome this, the result of a theoretical paper written by Berezinskii in 1974, concerning a proposed odd frequency phase in superfluid ^{3}He, is employed [39]. While this phase was never found and the work of Berezinskii was relatively unnoticed, in 2001 Bergeret *et al.* recognised a Berezinskii state could create a triplet state in BCS superconductors which avoids violating quantum mechanics [40]. The widely accepted proposal is that while the triplet order parameter is symmetric in angular momentum, it is now antisymmetric in frequency. Cooper pair interaction is now asymmetric under a time reversal.

2.4 Proximity Effects

In the broadest terms, a proximity effect is the influence of one long-range order parameter on another, when two systems of differing orders are forced to share an interface. In this work it is the influence, competition and co-existence of superconducting and magnetic orders within proximity structures which are of interest. Traditionally considered competing phenomena, their differences are such that they can drastically alter each others properties, or suppress one ordering altogether. There are several comprehensive reviews on this topic, such as Buzdin [41], Bergeret [42] and Eschrig [43].

2.4.1 S/N

Key to this thesis is the understanding of the superconducting proximity effect. Considering first the case where the adjacent material is a normal metal, some of the Cooper pairs from the superconductor are able to extend a certain distance across the interface, into the normal metal. They retain their superconducting properties inside the normal metal. Inside the normal metal, no new Cooper pairs are formed, rather the superconductor donates its existing Cooper pairs. This extension of Cooper pairs close to the interface results in the superconducting order parameter becoming weaker at the interface (referred to in some literature as the *inverse* proximity effect) [42]. This is the first example of the way in which,

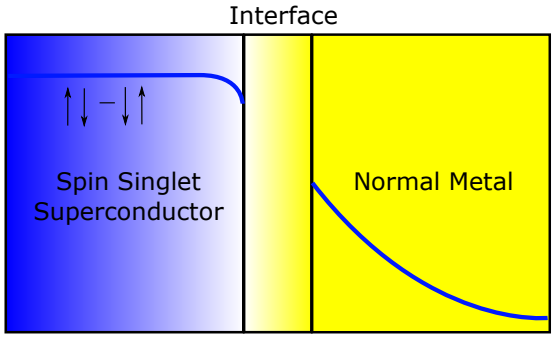

Figure 2.1: Leakage of Cooper pairs at the superconductor/normal metal interface. Cooper pairs are able to penetrate the normal metal, which causes the Cooper pair density inside the superconductor to decrease.

for a thin film, proximity effects suppress the superconductivity, and with it a lowering of the superconducting transition temperature occurs. Proximity at the S/N interface is shown schematically in Figure 2.1.

Through the formalism of de Gennes, it is possible to describe the spatial extent of this normal proximity effect through an effective coherence length inside the normal metal ξ_n [44]. Inside the normal metal it is thermal fluctuations which destroy the coherence of the Cooper pair. ξ_n is therefore given by the thermal diffusion length (L_T), and [41]

$$\xi_n = \sqrt{\frac{\hbar D}{2\pi k_B T}}, \tag{2.18}$$

where D is the material dependent diffusion constant and T is the temperature. This length scale is typically 100's of nm into the normal metal [45].

An important characteristic of the superconducting proximity effect is the Andreev reflection at the microscopic scale [46]. Andreev demonstrated how single-electron states of the normal metal are converted into Cooper pairs, and also explained the transformation of a normal state current into the dissipationless supercurrent at the interface. An electron with an energy below the superconducting gap is reflected at the interface as a hole. The corresponding charge of $2e$ is transferred to the Cooper pair which appears on the superconducting side of the interface. The process can be detected as a doubling of the normal metal's conductance. The retro-reflected hole carries with it phase information of the superconducting state [25, 47].

2.4.2 S/F - Fulde-Ferrell-Larkin-Ovchinnikov State

When a ferromagnet is placed in proximity to a superconductor, it is no longer thermal fluctuations which destroy the Cooper pairs. The exchange field present inside the ferromagnet creates a re-entrant property which is caused by a shift in the momentum of the Cooper pairs [41].

Cooper pairs which enter the ferromagnet will be aligned either parallel or antiparallel to the direction of the exchange field. Parallel orientations will experience a decrease in potential energy relative to spins aligned antiparallel. The kinetic energy for parallel (antiparallel) spins will be increased (decreased) by Δk^2. The pairs inside the ferromagnet no longer have zero total momentum. Now Cooper pairs exist with values of momentum $\pm\Delta k$ altering the distribution of pairing density. This state was proposed by Fulde and Ferrell in 1964 [48] and independently by Larkin and Ovchinnikov in 1965 [49] for superconductors in the presence of a magnetic field and is referred to as the FFLO (or LOFF) state. This non-zero momentum component will correspond to a generation of a new m = 0 triplet state at the interface and an oscillation in the order parameter with respect to distance inside the ferromagnet.

These oscillations are shown schematically in Figure 2.2 for three possible ferromagnetic cases. Firstly in the case of a weak ferromagnet (for example low Curie temperature CuNi) the oscillations can extend a relatively long distance into the ferromagnet (typically 10's nm) and the inverse proximity effect is small. Proximity effects with the strong ferromagnet (for example high Curie temperature Co) are of much shorter length scale (1-2 nm). In this system the inverse proximity effect is larger, with a considerable m = 0 triplet component detectable on the superconductors side of the interface. For the case of a half metal, where all transport is 100% spin polarised, there is no leakage of either singlet or m = 0 triplets into the ferromagnet. In this system there is a considerably larger inverse proximity effect.

The characteristic length scale for the decay of the singlet wavefunction inside the ferromagnet is defined as an effective coherence length (ξ_f) inside the F layer. ξ_f depends upon the type of electron transport within the system (ballistic or diffusive). A ballistic (or 'clean' in some literature) case is defined where $\xi_f >> l$, where l is the electron mean free path (mfp). The alternative diffusive (or 'dirty') case is defined where $\xi_f << l$. The coherence lengths in these two limiting cases are defined respectively as [41];

$$\xi_f = \frac{\hbar v_F}{2\pi T} \tag{2.19}$$

and

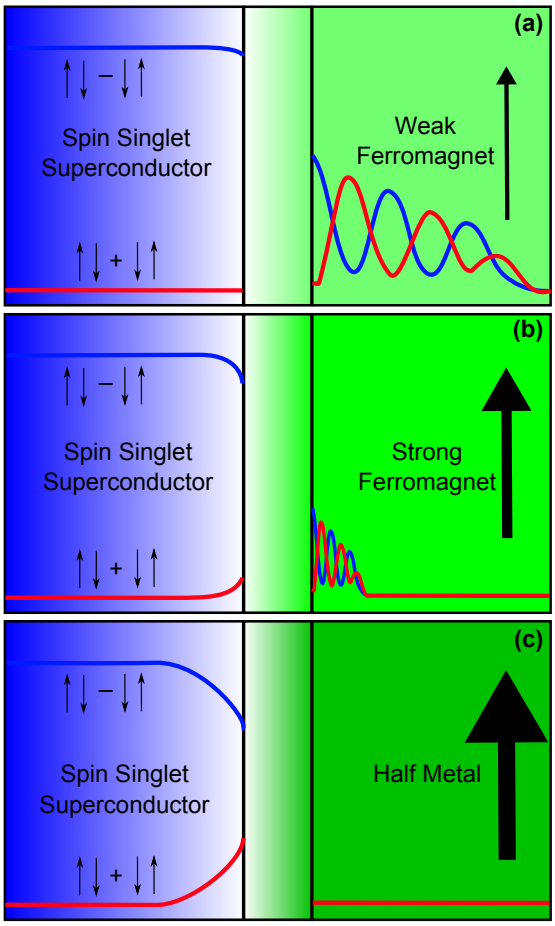

Figure 2.2: Leakage of Cooper pairs at the superconductor/ferromagnet interface. At the interface a new S=1, m=0 ($|1,0\rangle$) short ranged triplet component is generated. Inside the weak and strong ferromagnet, the singlet and triplet components oscillate out of phase with each other (the FFLO state). In the case of a half metal, neither superconducting component can enter.

$$\xi_f = \sqrt{\frac{\hbar D_F}{E_{ex}}}, \tag{2.20}$$

where v_F is the Fermi velocity, D_f the diffusion coefficient and E_{ex} the exchange energy of the ferromagnet which is approximately given by $k_B T_{\text{curie}}$ [41]. For the sputtered thin films in this work it is the diffusive limit which is appropriate.

In the formalism of the BCS theory (using the conventions of Eschrig [6]) it is possible to write the evolution of the wavefunction at the S/F interface in the following way. Starting deep inside the superconductor, only singlet Cooper pairs exist;

$$|\Psi\rangle = |0,0\rangle = \tfrac{1}{\sqrt{2}}\big(|\uparrow\downarrow\rangle - |\downarrow\uparrow\rangle\big).$$

At the S/F interface the exchange energy adds a shifted momentum term Q,

$$|\Psi\rangle = \tfrac{1}{\sqrt{2}}\big(|\uparrow\downarrow\rangle\, e^{iQx} - |\downarrow\uparrow\rangle\, e^{-iQx}\big),$$
$$|\Psi\rangle = \tfrac{1}{\sqrt{2}}\Big[\big(|\uparrow\downarrow\rangle - |\downarrow\uparrow\rangle\big)\cos Qx + i\big(|\uparrow\downarrow\rangle + |\downarrow\uparrow\rangle\big)\sin Qx\Big],$$

which is simplified to,

$$|\Psi\rangle = |0,0\rangle\cos Qx + i\,|1,0\rangle\sin Qx. \tag{2.21}$$

where the $|1,0\rangle$ state is the short ranged, m = 0, triplet component (SRTC). The spatial dependence on the singlet of cosine and the triplet of sine is the origin of the oscillation in the FFLO state. This is referred to in some literature as the singlet/triplet mixed state.

2.4.3 S/F - Long Ranged Triplet Component

Continuing from the FFLO state, in the presence of an inhomogeneous magnetic field at the interface, the $|1,0\rangle$ component can be converted into the possible states [6]:

$$|1,0\rangle \rightarrow \begin{cases} |1,1\rangle = |\uparrow\uparrow\rangle \\ |1,0\rangle = \tfrac{1}{\sqrt{2}}\big(|\uparrow\downarrow\rangle + |\downarrow\uparrow\rangle\big) \\ |1,-1\rangle = |\downarrow\downarrow\rangle \end{cases} \tag{2.22}$$

where the symmetric spin-triplet states, $|\uparrow\uparrow\rangle$ and $|\downarrow\downarrow\rangle$ are known as the long ranged triplet

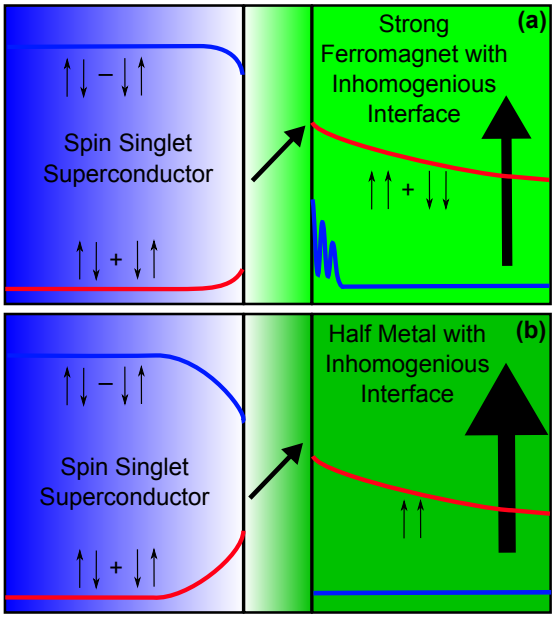

Figure 2.3: Leakage of Cooper pairs at the superconductor/ferromagnet interface, where the interface is inhomogeneous. Inside the inhomogeneity new S=1, m=±1 ($|1,1\rangle, |1,-1\rangle$) triplet components are generated, which can penetrate both strong ferromagnets and half metals.

components (LRTC)[1]. Being aligned to the exchange field, ferromagnetic pair breaking no longer takes place. The length scale for the LRTC to exist inside the ferromagnet is related to thermal fluctuations with a similar mechanism to that of proximity to a normal metal [50]. The length scale for the LRTC proximity is therefore given by equation 2.18. A schematic of this conversion is given in Figure 2.3. For the case of the strong ferromagnet the $|\uparrow\uparrow\rangle$ state is preferentially transmitted into the ferromagnet, although a smaller $|\downarrow\downarrow\rangle$ component also exists in the minority band [6]. The typical length scale of this proximity effect is now 10's nm [51]. In the case of a half metal, the minority band is insulating, and so only the $|\uparrow\uparrow\rangle$ component is transmitted, with the $|\downarrow\downarrow\rangle$ component reflected back into the superconductor. For the case of a half metal the proximity effect can have ξ_f =100's nm [52].

The exact nature of the magnetic inhomogeneity required is somewhat ambiguous. Theoretical literature has previously focused on LRTC generation by magnetic domain walls [53–55], where the presence of a domain at the S/F interface was able to convert the short range triplet into the LRTC. Other theoretical proposals have shown LRTC generation is possible using (but not limited to); conical ferromagnetic structure [56–61], multilayer structures [62–65], canted moments at the S/F interface [50], magnetic vortices [66, 67], spin-orbit coupling [68, 69] and magnetic skyrmions [70, 71]. From the large body of theoretical work, this thesis makes the reasonable assumption that any magnetic inhomogeneity will generate a LRTC. The exception to this is the case for ideal antiferromagnetism, where the repeat distance is much smaller than ξ, and so what may be perceived as magnetic inhomogeneity is not actually sampled by the Cooper pair. Due to the short mfp inside an antiferromagnet any proximity effect will be short lived (but with no FFLO or LRTC generation) [72, 73].

2.5 Induced moment at the S/F interface

A key experimental aim of this thesis is the direct observation of the induced moment expected from triplet Cooper pairs in the S/F system. Three theoretical descriptions of the expected induced moment are presented.

[1] In this case 'long' is in comparison to the FFLO state, where the m=0 triplet may be referred to as the 'short' ranged triplet component (SRTC). The penetration of the 'long' ranged triplet is not long compared to the singlet penetration in S/N proximity.

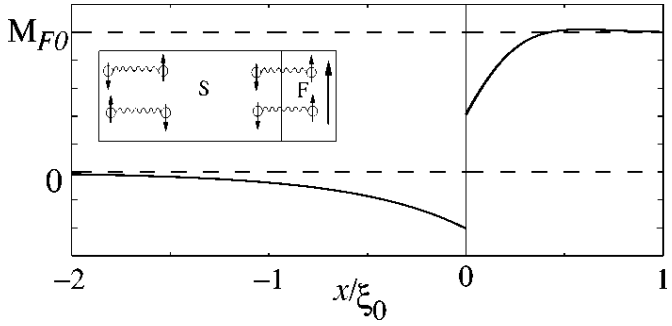

Figure 2.4: Spatial dependence of the induced magnetisation (M_{F0}) at the S/F interface ($x/\xi_0 = 0$) where ξ_0 is the zero temperature coherence length. Inset: Schematic view of the inverse proximity effect. Reproduced from Bergeret *et al.* [74].

2.5.1 Bergeret Inverse Proximity Induced Ferromagnetism

So far in this section, all that has been considered is the penetration of the superconducting order into the adjacent metal. In the case of the adjacent metal being a ferromagnet Bergeret *et al.* considered the question "can the ferromagnetic order penetrate the normal metal or superconductor over long distances?" [74]. In the case of a N/F interface it is not uncommon for the normal metal's spins to become aligned at the interface, for example when vanadium (in the normal state) is in proximity to iron [75, 76]. In this work, care was taken to choose materials with no known N/F magnetic proximity. Any induced moment in these systems is as a consequence of the onset of superconductivity.

Starting from the assumption that the F layer is thin and all Cooper pairs are antiparallel so the total magnetic moment of the pair is equal to zero, it is clear that the Cooper pairs existing only in the superconductor cannot contribute to the magnetic moment of the superconductor. The moment is simply zero. It is possible, nevertheless, to imagine some pairs which are located in space in a more complex manner: one of the electrons of the pair is in the superconductor, while the other moves in the ferromagnet. These pairs create the magnetic moment in the superconductor. The direction along the ferromagnets moment is preferable for the electron located in the ferromagnet. This makes the spin of the other electron in the pair antiparallel to the ferromagnet. All such pairs equally contribute to the magnetic moment in the bulk of the superconductor.

As a result, a ferromagnetic ordering is created in the superconductor with opposite direction to the ferromagnet over the length scale of the size of the Cooper pair, ξ. A second

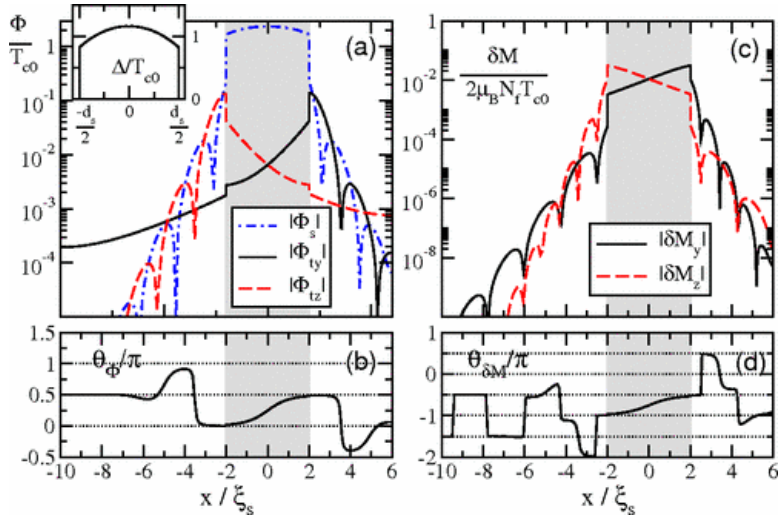

Figure 2.5: **(a)** The spatial variation of the singlet and short and long ranged triplet components in a F/S/F trilayer. **(c)** The induced magnetisation from the triplet components. Reproduced from Löfwander *et al.* [63].

consequence is the lowering of magnetic moment in the ferromagnet as the proximity effect reduces the density of states in the F layer. This result is reproduced from Ref [74] and shown in Figure 2.4.

A small number of reports attribute observations to this effect, however in almost all cases the technique employed did not have adequate statistics or the required spatial sensitivity to characterise the effect in detail [77–80]. A further report utilising the LEμSR technique (see section 3.8), which possesses the required spatial resolution, found the expected induced moment in the S layer, but with a length scale of only $1-2$ nm. This is far shorter than the coherence length inside the Nb S layer of 10 nm [33]. This report either suggests that the key length scale of induced moment is more similar to the effective coherence length inside the ferromagnet, or that a rather different interfacial mechanism is present in that work, and possibly others.

2.5.2 Löfwander Triplet Induced Spin Magnetisation

In the work of Bergeret *et al.* [74]; only homogeneous magnetisations and singlet Cooper pairs were considered. Löfwander *et al.* extend this work to include triplet Cooper pairs [63]. This work considers a F/S/F trilayer with arbitrary angle between the moments of the

F layers. When the moments are aligned parallel or antiparallel, singlet and short ranged (m=0) triplet Cooper pairs exist inside the superconductor and very short distances inside the ferromagnet. Inside the ferromagnet these two components oscillate and decay rapidly. For other orientations the m= 1 LRTC is also induced, which penetrates deep inside the ferromagnet and does not oscillate. Figure 2.5 (a) shows the spatial profile of the three components. Note that the LRTC is only generated nonlocally in one ferromagnet by diffusion of the SRTC from the other through the superconductor. The consequence of this is the LRTC at the interface is already quite small and hard to detect.

The most surprising finding of this work is that triplet pairs in isolation do not contribute to induced moment, rather it is the product of the singlet and triplet components which is proportional to the induced magnetisation. Both short and long ranged triplets contribute to induced magnetisation. The consequence of this can be seen in Figure 2.5 **(c)** which shows the spatial profile of the induced magnetisation (δM). Inside the superconductor δM is spread out over the longer length scale ξ_s. But δM decays rapidly in the ferromagnet on the scale ξ_f, because of the dependence on the fast decaying singlet component.

A further consequence of the dependency on the presence of the singlet component is that the oscillation periods of δM are different for the short and long ranged triplet components. The oscillation period for δM induced by the LRTC is twice that for the SRTC. This is caused by the product of an oscillating singlet with a monotonic LRTC and oscillating SRTC. Inside the superconductor the induced moment is consistent with the description from Bergeret *et al.*, it should be antiparallel to the direction of the ferromagnetic moment and decaying away from the interface over the length scale of a Cooper pair.

2.5.3 Inverse Meissner Screening

Several reports have studied theoretically the magnetic susceptibility of singlet and triplet Cooper pairs inside proximity structures [81–85]. It is well known that superconductors set up Meissner screening currents in response to an externally applied field. The LRTC, however, contributes a positive component to susceptibility when it is present. When a sample is designed so that one can isolate the LRTC inside a normal metal (for example in an S/F_1/F_2/N spin valve) the response from the normal metal (from only the LRTC) will be paramagnetic.

The 'smoking gun' experimental observation of this inverse Meissner screening is not necessarily the observation of paramagnetic response, but the ability to reverse the suscept-

ibility of the normal metal by either tuning the production of the LRTC [84] or observing an expected oscillation between positive and negative susceptibility with temperature [82].

It should be noted that this induced moment from the creation of paramagnetic screening currents is different in origin to the induced ferromagnetism of Bergeret *et al.* and Löfwander *et al.*. In order to observe this effect one needs to design a structure where the thicknesses of the layers in which these effects are observed are larger than the penetration depth. Therefore it would be very difficult to deconvolute any response from the traditional Meissner effect (which would be much larger in magnitude).

A very recent report claims the observation of an inverse Meissner screening effect created by the LRTC [34] measured using the LEμSR technique outlined in Section 3.8. This observed effect, however, is very small, with poor statistical fidelity and incomplete data sets making it impossible to attribute the observed effect to the onset of superconductivity, as opposed to changes in the ferromagnet's magnetisation or a rearrangement of stray fields due to screening by superconductivity (for example).

2.6 Experimental Observation of the FFLO state

The signature of the FFLO state is an oscillating superconducting wavefunction inside an exchange field. The two main methods of detecting this oscillatory behaviour are in T_c measurements of S/F bilayers and critical current measurements across S/F/S Josephson junctions.

2.6.1 Measurements of T_c

The damped oscillatory behaviour of the superconducting order parameter inside an adjacent F layer results in a nonmonotonic superconducting T_c dependence on the F layer thickness. The predicted oscillatory-type dependence of the critical temperature [86, 87] was subsequently observed experimentally in Nb/Gd [88], Nb/CuMn [89], and Nb/Co and V/Co [90] multilayers, as well as in bilayers Nb/Ni [91], trilayers Fe/V/Fe [92], Fe/Nb/Fe [93], Nb/[Fe/Cu] layers [94], and Fe/Pb/Fe [95].

2.6.2 Josephson Junctions

Oscillation of the order parameter inside the F layer in an S/F/S Josephson junction is responsible for a thickness dependent switching of the phase across the junction. At ferro-

magnet thickness $< \xi_F$, the singlet pair wave function inside the ferromagnet changes little and so the order parameter will be identical in both S layers. On the other hand, if the F layer thickness is $\approx \xi_F$ then the singlet pair wave function may reach zero value at the centre of the F layer, with an opposite sign or π shift of the phase of the order parameter in the adjacent S layer [41]. This is the so-called $0-\pi$ transition. Now a highly reproduced result, the first observation of reenterent $0-\pi-0$ critical current with F thickness was observed in 2006 by Oboznov *et al.* for a weak ferromagnet [96] and by Robinson *et al.* for a strong ferromagnet [97].

2.7 Experimental Observation of the LRTC

The first initial hints for the presence of the LRTC in S/F proximity structures came in 1998 with a report of Co wires with Al contacts showing a large decrease in resistance when the Al was in the superconducting state. To explain this result it was concluded the proximity effect in the Co wires had to be much longer than expected, however the authors did not offer any insight into the origin of the effect [98]. A similar report the following year stated "we observe a spectacular drop in the resistance of the F/S junction at the onset of superconductivity with slow changes persisting down to the lowest temperatures." Additionally it was commented that the sample-to-sample interface transparency had an important role [99]. A similar observation in a wire made of Ho was reported in 2006 [56]. Ho has spiral magnetisation, and so is capable of generating the LRTC. In 2010, a report from Wang *et al.* demonstrated zero resistivity in a 600 nm long Co wire with superconducting electrodes attributed to LRTC generation and propagation [100]. The extremely long length scale of the effect compared to other works using Co was attributed to the wire being a single crystal, although it was unclear where the necessary source of inhomogeneity to generate the LRTC arose in this work.

2.7.1 Josephson Junctions

The first definitive observation of the LRTC came in 2006 from Keizer *et al.* in passing a supercurrent through half metallic CrO_2 [101]. In this work the only allowed proximity into the half metal is the LRTC. The triplet supercurrent was propagated about a micron between superconducting electrodes placed laterally on the surface of the CrO_2. It was noted a large sample to sample variation was observed, with only a minority of devices working (about 1

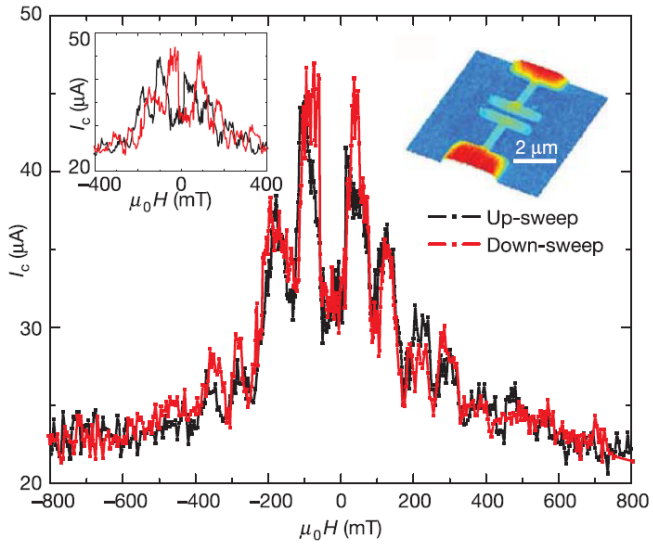

Figure 2.6: Critical current as a function of external magnetic field, applied in the plane of the film, for a lateral NbTiN Josephson junction device across half-metallic CrO_2. The raw data (showing hysteresis with magnetic switching) and SEM of fabricated devices are shown as insets. From Kiezer *et al.* [101].

in 50) with a large range in $\mathbf{J}_c$ values. The LRTC generation was explained by the surface state of the CrO_2 providing the necessary inhomogeneity. If the local area of the contacts were in a position of inhomogeneity, the LRTC was generated, otherwise no proximity effects were observed.

Continuing this work, Anwar *et al.* showed that by optimising the treatment of the CrO_2 surface by pre-deposition cleaning, triplet supercurrents could be passed through the CrO_2 up to 700 nm [52]. This acted as confirmation of the results from 2006. These works on half-metallic materials show the longest propagation through a ferromagnet and are the only observations in the lateral junction geometry. This report was the first of 3 in 2010 which outline the now standard methods of injecting a controlled triplet supercurrent into a ferromagnet.

The second report from Khaire *et al.* involved controlling the inhomogeneity by employing a multilayer approach [102]. Large area Josephson junctions were fabricated using sputter deposition through masks in a S/F'/F/F"/S design. In this scheme the magnetisation of the F' and F" layers are perpendicularly aligned to the F layer. This is achieved by making the F' and F" layers thin and with low anisotropy, so they are aligned to a small ex-

ternal field. The central F layer is a Co/Ru/Co synthetic antiferromagnet (SAF). This layer serves two purposes, upon the application of a saturating field and subsequent relaxation of the field, the SAF aligns perpendicular to the applied field. Secondly the domains in the two Co layers cancel, which significantly reduces the stray field effects from the layer. This in turn minimises the magnetic flux in the junction. It is the misalignment of the SAF from the other ferromagnets which generates the LRTC. Triplet currents were propagated up to 28 nm through the Co.

The third report from Robinson *et al.* added thin layers of the magnetic spiral material Ho at both sides of Co in nano-pillar Josephson junction [51]. It was shown that tuning the thickness of the Ho could control the LRTC generation, which was maximised when the thickness of the Ho was enough for it to develop spiral magnetisation.

Following from these three initial break throughs, research into the Josephson junction devices has continued in great depth. Several experiments have independently found evidence for LRTC penetration across junctions of different materials, for example Sprungmann *et al.* showed critical current characteristics consistent with LRTC generation in junctions containing the Heusler alloy Cu_2MnAl [103]. In this alloy intrinsic inhomogeneity is generated at interfaces, where a spin glass low moment phase exists. This interface magnetism transitions to a ferromagnetic type ordering at the core of the film.

The group working on CrO_2 has shown that adding additional 'spin mixer' layers of Ni between the superconductor and CrO_2 greatly improves the reliability of LRTC generation. Additionally the surface state of the CrO_2 can be controlled with substrate choice [104].

The second group employing the multilayer approach have reported optimisation of the devices, with a confirmation of the domain structure of the SAF by PNR [105]. Additionally they substituted the F' and F" layers for ferromagnetic multilayers with perpendicular anisotropy and report that this too generates LRTC [106].Most recently efforts have focused on the fabrication of switchable Josephson junctions for cryogenic memory elements [17]. By utilising a combination of hard and soft magnetic layers for the F' and F" spin mixer layers, it is possible to independently switch F' and F" and control LRTC generation [107]. This group has also been the first to fabricate SQUID devices which employ two magnetic Josephson junctions [18], although they are yet to incorporate the LRTC into the SQUID geometry.

The low temperature spiral properties of epitaxial Ho were studied with neutron diffraction, confirming its helical properties in the thin film [108]. Additionally, Josephson junctions with Ho as the sole F layer were fabricated, in which no observation of the 0-π trans-

ition was observed. This was due to the magnetic coherence length through the Ho being very short, consistent with only a singlet component present inside the Ho. Gd was used in an S/F/S junction where Bloch domain walls can be controllably generated at the interfaces. When the domain walls were at the interface, evidence for the LRTC was observed [109]. In a similar experiment, the interface in Cr/Fe can generate an antiferromagnet type ordering. This inhomogeneous ordering was used to generate a triplet supercurrent [110]. Finally using a stack of ferromagnets with different anisotropies, triplet pairing was observed in a junction with multilayered F structure [111].

There has been experimental and theoretical work to realise long ranged triplet type proximity in Josephson type devices where the superconductor is a thin film high T_c, such as YBCO [112–116]. Additionally the first step has been made in coupling a ferromagnet to $SrRuO_3$, which has an intrinsic triplet ordering [117].

2.7.2 Superconducting Spin Valves

Initial interest in the superconducting spin valve centred around the concept of achieving an infinite magnetoresistance [118]. By measuring around the T_c of the superconductor, it was theoretically possible to tune superconductivity by the mutual orientation (parallel or antiparallel) of two F layers in an $S/F_1/F_2$ or F/S/F type multilayer. The initial physical picture presented in early work in this field was that shifts in T_c were due to pair breaking spin polarisations, extending into the S layer from the F layers. When the F layers were antiparallel these polarisations effectively cancel out, however when parallel they enhance each other and suppress superconductivity [14, 118–121].

The experimental results attempting to observe this infinite MR showed that while there was a shift in T_c, it was a much smaller effect compared to predictions from theory. The largest observed ΔT_c was ≈ 40 mK. This shift is much smaller than the typical transition width of a thin film proximity coupled superconductor, and so the predicted complete switching was not observed [122–126]. Additionally it was observed that the higher T_c state was not always observed in the parallel case [127–129]. Interestingly the MR measured in the transition was larger than expected for the same magnetic structure without a superconductor. This may be due to the ability of a superconductor to carry information about the alignment of the ferromagnets as quasiparticles [130]. This will be discussed in detail later. In 2010 the complete switching effect was achieved in a system with a very narrow transition width [131, 132]. This observation was followed up in 2013 in a system where the F layers

were ferromagnetic insulators [133] and in 2015 where the F layers were the RE Ho (which has already been shown to have a proximity effect with Nb) or Dy [134].

Together these observations fuelled a development of the theoretical framework to include the triplet superconducting components. The groundwork for the generation and observation of the LRTC in a $S/F_1/F_2$ spin valve structure was developed by Fominov *et al.* [65] and was later extended for an F/S/F type spin valve [135]. The now accepted interpretation of shifts in T_c between the parallel and antiparallel magnetisation alignments is via the same mechanism as oscillations due to the FFLO state, singlet/triplet mixing. In these magnetic orientations only short ranged triplets and singlets are present. Switching between the two magnetic alignments changes the effective thickness of the exchange field observable to the superconductor. The sign of the shift (increase or decrease in T_c) is now an oscillatory function of ferromagnet thickness which is consistent with the previous observations [132].

Changing the separation angle to create misalignment creates the required non-collinearity for LRTC generation. The LRTC effectively increases the range of coupling between the S/F layers, creating additional channels for supercurrent leakage into the F layers. The consequence of this is a reduction of pairs inside the superconductor and a suppression of T_c. Maximum generation occurs at maximum non-collinearity (perpendicular or 90 degrees) which is where the largest suppression in T_c should be observed. The triplet spin valve effect. This is now a widely accepted and reproduced result. Presented here are the current experimental results showing angular dependence of superconducting spin valves consistent with that of the triplet spin valve.

Leksin *et al.* first observed the signature triplet spin valve effect in an $S/F_1/F_2$ exchange biased Pb/Fe spin valve [19] as reproduced in Figure 2.7. They continued to study the dependency of thicknesses of each layer [136] and found that there was intermixing between the Pb and Fe, which occurred after the deposition process and caused the degradation of samples over the time scale of a week [137]. Adding Cu spacer layers significantly improved the sample quality, and the size of the observed spin valve effect was found to be dependent on the interfacial roughness; with smoother interfaces giving a larger effect. Rougher or grainy films showed less angular dependence. This observation is consistent with other reports [21, 138]. Most recently this group has worked on the 'isolation' of the triplet spin valve effect. In the theoretical framework of Fominov there exists a narrow range of F thicknesses for which there is no change in T_c between parallel and antiparallel, but for which the triplet effect is still present. Samples were recently fabricated which demonstrate this

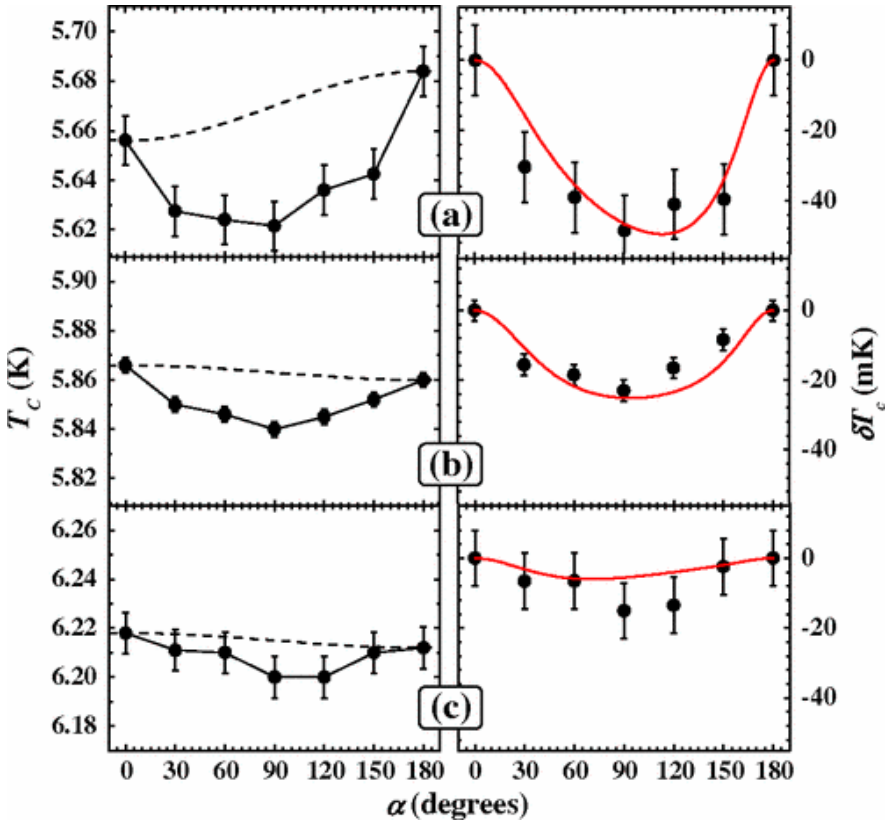

Figure 2.7: Angular dependence of the superconducting transition temperature of the $S/F_1/F_2$ superconducting spin valve, showing minima at 90° as expected for triplet generation behaviour. The thicknesses of the F_1 layer are 0.6 (a), 1.0 (b) and 1.5 nm (c). Left: The dashed lines are the expected behaviour of the spin valve when no LRTC formation is present. Right: The deviations from T_c 0° and theoretical result (solid red line) when the LRTC is present. From Leksin *et al.* [19].

[139].

In addition to the Pb/Fe system, the S/F_1/F_2 triplet spin valve effect has been shown in Nb/Py/Co pseudo spin valves [21], Nb/Co exchange biased spin valves [20, 22], and in the F/S/F spin valve structure in Co/Nb/Co [22] and CuNi/Nb/CuNi [140]. The size of the spin valve effect can be greatly enhanced by replacing the lower 'drainage' layer with a material of very high spin polarisation such as CrO_2 [141]. This is consistent with the large proximity effects observed in Josephson junctions containing CrO_2 and highlights the importance of high spin polarisation in the transport of the LRTC.

The T_c shifts observed in these works have a periodicity of 180 degrees, which is then related back to the orientation of the ferromagnetic layers and hence is attributed solely to the triplet generation. None of these works factor in that the periodicity and magnitude of the observed effect is the same as a number of other potential measurement artefacts. Upon attempting this measurement the author became aware of the following things to look out for.

Firstly the complex multilayer approach taken by all groups (and the sensitivity to very thin layers) means that samples grown in different vacuum cycles can give very different behaviour. In some works (for example [137]) interdiffusion between layers occurs on the time scale of days after the structures are grown. Without clean interfaces it is impossible to know the true thickness of layers (especially magnetic layers, in which the magnetisation may weaken or dead layers appear).

The reported triplet spin effect is typically only 10-20 mK in size. It is therefore important to have temperature stability in the measurement system which allows such small changes in T_c to be reliably measured. This stability can either be the ability to measure at a constant temperature and rotate the sample, or alternatively to have a well controlled cooling at a constant rate, and record many cooling curves at fixed angles.

Next the issue of sample rotation needs to be addressed. In literature there does not appear to be a consensus as to what is the best methodology for undertaking the sample rotation. Two options were explored in this work. The first, application of a field by split pair magnets or Helmholtz coils across the sample space. The sample and measurement stick is subsequently rotated by hand or stepper motor in the field. The second methodology is to place the entire cryostat between Helmholtz coils and rotate the cryostat. If rotation occurs too quickly it is possible that the act of rotating the sample creates local heating. In both measurements it is difficult to be able to align the sample so that it is exactly known

what direction the field is pointing with respect to the pinning or current direction. It may therefore be necessary to centre the sample before beginning measurements.

Non-uniformity of temperature, field and angle are all issues under rotation. Any change to temperature or field uniformity during rotation may appear identical to the spin valve effect. It is also impossible to mount a sample in such a way that the applied field will be completely in-plane. Any misalignment will create an out-of-plane field component, which will not be completely uniform under rotation. If the sample 'wobbles' under rotation then this will change the out-of-plane field component, which will also change the T_c.

Finally, possibilities of vortex flow and induced voltage from this phenomena need to be addressed. Even when a film is too thin to form in-plane vortices, the out-of-plane field component will create vortices on the films surface. During rotation the angle between applied current and field will continually change, modifying the Lorentz force acting on the vortices. As a function of angle, therefore, the induced voltage from the motion of the vortices will oscillate with the same periodicity as the triplet spin valve effect.

There are also angular dependent studies which do not show evidence for triplet effects, and instead show monotonic changes from parallel to antiparallel alignments [142] or completely anomalous T_c changes [143].

Samples grown by the author and measured by Dr. M. G. Flokstra have addressed all of the above issues (in both sample preparation and how the measurement was performed. See [22] for details on the experiment and section 2.10 plus Chapter 6 for characterisation of the spin valves.) By rotating the sample at a constant temperature, T_c shifts consistent with LRTC generation were observed, with the result plotted in Figure 2.8.

2.7.3 Density of States

The superconducting density of states (DoS) can be determined by tunnelling spectroscopy and the measured conductance (dI/dV) with bias voltage. The presence of a LRTC gives rise to a conductance peak at zero bias, where in a purely BCS gapped state a minimum should exist [144–146]. Most work to observe this peak at zero bias has been conducted on high T_c superconductors which, despite having a different pairing mechanism, have similar proximity effects with ferromagnets and can generate the LRTC when there is inhomogeneity [112, 114]. Several reports have shown conductance behaviour consistent with the presence of a LRTC on the ferromagnetic side of S/F bilayers in high T_c systems [113, 115, 147, 148].

While searching for signatures of Majorana fermions in proximity-induced topological

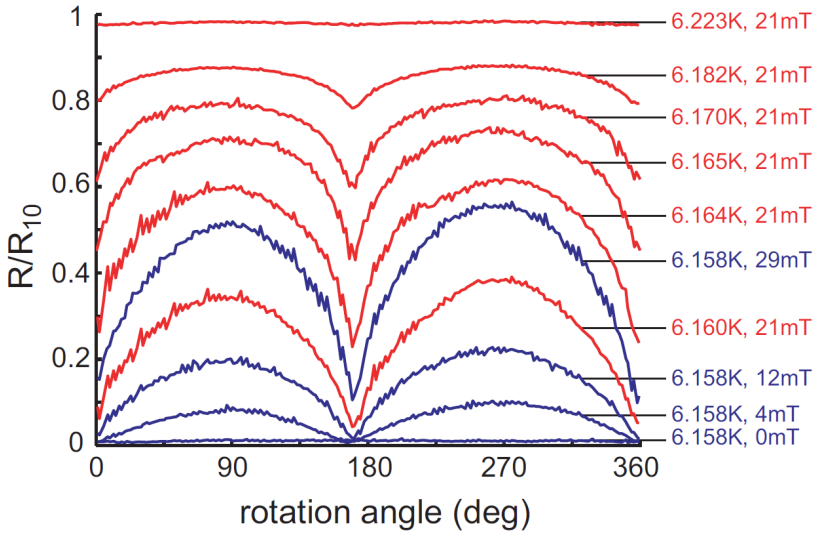

Figure 2.8: (Red) Angular dependence of resistivity at various temperatures in the superconducting transition for the $S/F_1/F_2$ superconducting spin valve grown by the author. Maxima in resistance is at 90° and 270°, corresponding to the minima in T_c, as expected for triplet generation. Additionally shown in blue is the field dependance of the effect, demonstrating that applied field is a possible control parameter for the spin valve effect. From Flokstra *et al.* [22].

superconducting juctions, Koren *et al.* found conductance spectra with a prominent zero bias peak, suggesting the induced superconductivity in the topological insulator (Bi_2Se_3) was triplet in nature [149, 150].

A recent report by Di Bernardo *et al.* has shown a number of sub-gap features in the DoS in a hybrid Au/Nb/Ho multilayer, where the conductance was measured in the proximity gapped Au layer [151]. A spatial mapping of sub gap features, reproduced in Figure 2.9, showed most commonly a split double peak was observed, within which some zero bias peaks are also present. These peaks only appear at very low temperatures (< 300 mK). There were also normal areas and regions showing a purely BCS type gap. The application of an in-plane field modified the conductance and could destroy the peaks. This was related to the magnetic state of the Ho.

What should be noted, however, is that the LRTC is not the only source for sub-gap features such as a zero bias peak. Similar sub-gap features to that seen by Di Bernardo *et al.* exist as a result of Andreev processes in superconducting vortex cores and their surroundings [152–154]. At very low temperatures the core of a vortex gives a signature zero bias peak, which is surrounded radially by splitting into a double peak. Confirmation of the result of Di Bernardo *et al.* is needed to conclude if this is truly a triplet effect. The most important future experimental work would be the understanding of the temperature dependence of the sub gap features and an observation of the zero bias peak in a region where it is not surrounded by the split peak feature (which is not explicitly triplet in origin).

A recent observation in Bi/Ni bilayers showed that in thin film, when the two layers are grown in proximity to each other, superconductivity with a zero bias peak is observed. As neither layer superconducts on its own, it is suggested the system may have triplet pairing where the superconductivity is generated at the Bi/Ni interface [155]. If correct, this opens the exciting possibility of intrinsic triplet pairing in the thin film form, although possibilities of intermixing and alloying of the two layers needs addressing (as some BiNi alloys exhibit BCS superconductivity) [156–158].

2.7.4 Other Observations

Evidence for the LRTC can be deduced from T_c measurements of S/conical-F bilayers, where an observed oscillation of T_c with the pitch length of the cone can be related to LRTC generation [57, 58]. Such oscillations were observed for Nb/Ho bilayers [159, 160].

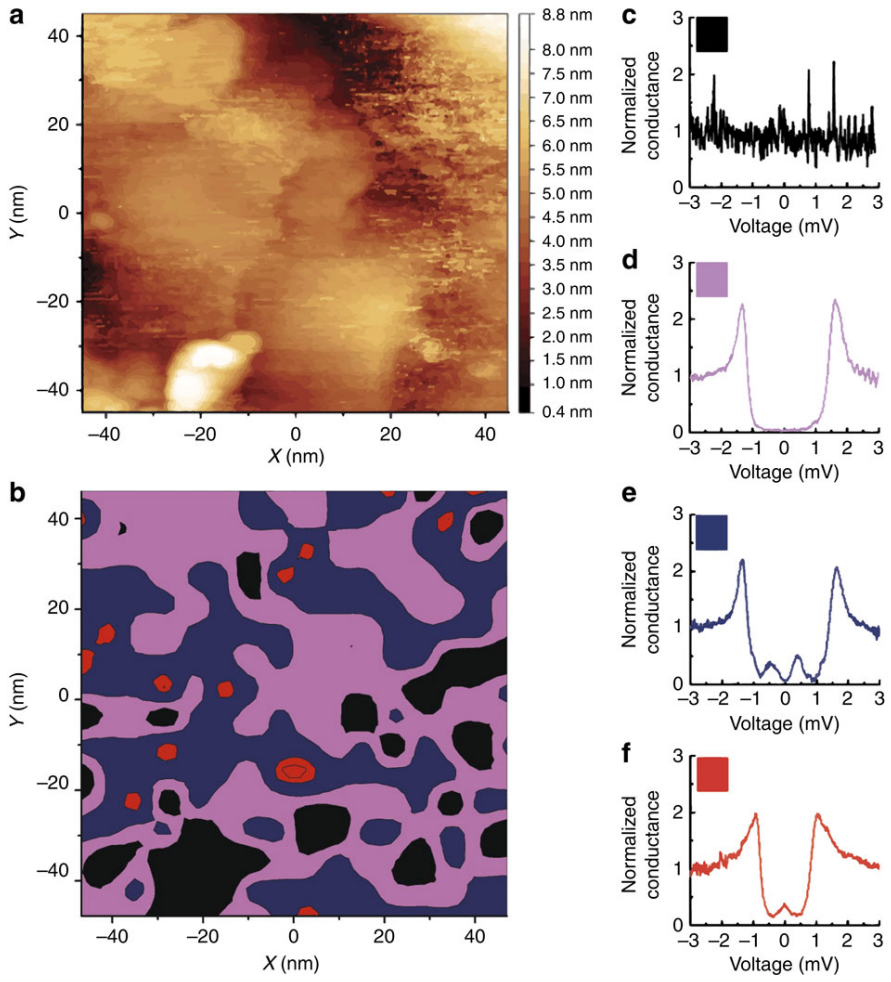

Figure 2.9: (a) Surface topography of the Au (3 nm)/Nb (20 nm)/Ho (9.5 nm)/Nb (6.5 nm)/sapphire samples (right key indicates sample height) and in **(b)** a spatial map of the corresponding spectra obtained at 290 mK; the different colours correspond to the different types of spectra observed and match the spectra shown in **(c)-(f)**. From Di Bernardo *et al.* [151].

2.8 Spin Transfer through a Superconductor

In addition to the type of proximity effects whereby purely Cooper pairs are considered, it is important to also consider the case where spin polarised quasiparticles can be injected into a superconductor.

A high priority for spintronics is to extend spin lifetime so it is long enough to perform a logic operation, or can be manipulated and read. In diffusive material spin lifetimes are typically fairly short, due to spin-orbit and spin-flip scattering processes. In a superconductor, it is possible to create spin 1/2 quasiparticles which carry a net spin component. In the superconducting state it takes longer for such quasiparticles to scatter through processes involving spin-orbit impurities relative to the scattering rates in the normal state. The consequence is that spin lifetimes in superconductors can be increased by many orders of magnitude relative to ferromagnetic metals [130, 161–166]. There have been several experimental reports of increased spin lifetimes of up to a million times in superconducting Al [10, 167, 168].

This is still a controversial result, with some experimental observations reporting a decrease in spin lifetimes (or relaxation length) when entering the superconducting state [169]. This is attributed to an increase in magnetic impurity scattering in the superconducting state, which *may* be improved by using purer superconductor.

In recent experiments by Wakamura *et al.* it has been demonstrated that a superconductor with strong spin-orbit coupling can preferentially absorb a pure spin current [170]. In this experiment a pure spin current is generated in a Cu wire, which is then preferentially absorbed into Nb both above and below T_c. It was possible to determine that the differences between preferential absorption above and below T_c were caused by an increase of 4x in the intrinsic spin relaxation time below T_c. This is consistent with other reports of an increase in spin accumulation in the superconducting state [169].

2.9 Domain Enhanced Superconductivity

An additional mechanism by which to influence superconductivity in an S/F hybrid system is presented here. It has been shown that altering the domain configuration in a F layer can influence T_c in an S/F bilayer [54, 171, 172] or F/S/F trilayer [173]. What is of particular interest in these works is that they have almost the opposite behaviour of the triplet spin valve, where the tuning of inhomogeneity lowers T_c. The result of Zhu *et al.* is reproduced in

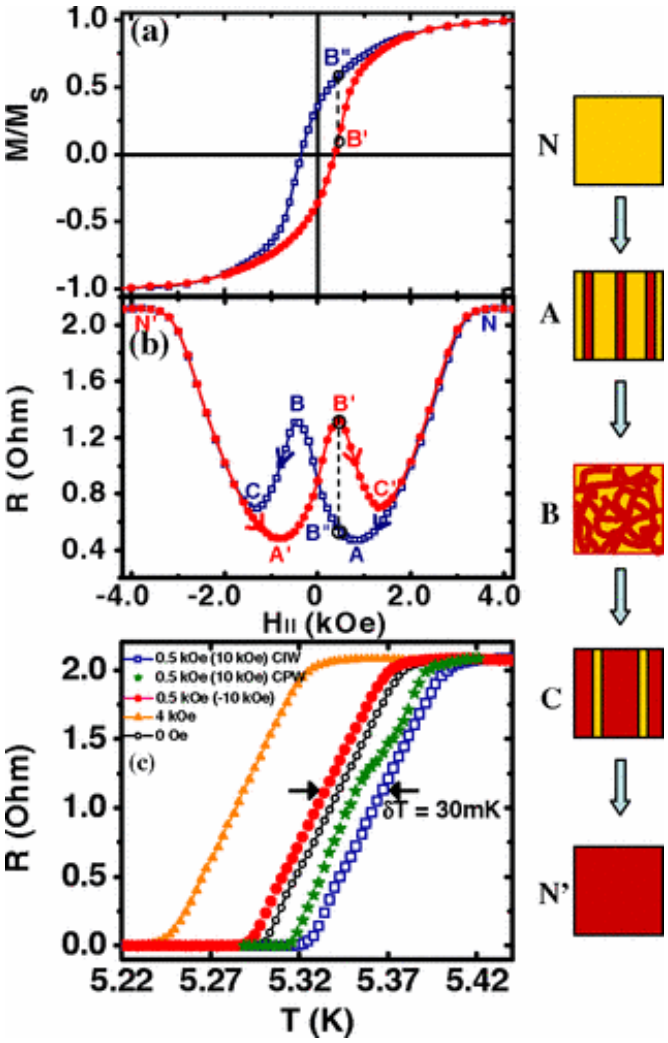

Figure 2.10: Domain enhanced superconductivity in a $[\mathrm{Co/Pt}]_n/\mathrm{Nb}/[\mathrm{Co/Pt}]_n$ multilayer, **(a)** normalized magnetization at 10 K and **(b)** resistance R at 5.350 K versus magnetic field. **(c)** Resistance (R) versus temperature (T) of the same sample at 4 KOe (in-plane saturation field, solid triangles), 0 KOe (remnant state, open circles), 0.5 KOe with measuring current parallel (CIW, open squares) and perpendicular (CPW, solid stars) to stripe domains (both reduced from +10 KOe), and 0.5 KOe (increased from −10 KOe, solid circles). The domain structure evolution is schematically shown on the right. Reproduced from Zhu *et al.* [171].

Figure 2.10. In this work a superconductor is sandwiched between Co/Pt multilayers. A field history can break the ferromagnetic layers into multiple domains, this causes an increase in T_c of 30 mK. Unlike the superconducting spin valve, here the low T_c state is when the ferromagnetic layer is single domain and homogeneous.

2.10 The Influence of Superconductivity on Magnetism

Until now the focus of this literature review has been on the magnetic ordering altering the pairing properties of the adjacent superconductor, or the mutual leakage of superconductivity into a ferromagnet. In this section the inverse case is considered, how does superconductivity affect the adjacent ferromagnet? The following contains mostly work performed by P. J. Curran on samples fabricated by the author and J. Kim. While the results are of importance to the interpretation of this thesis, they are presented independently in this section.

The observed phenomena can loosely be classified into two groups: Abrikosov vortex mediated pinning of ferromagnetic domains [174], and the restructuring of ferromagnetic domains due to changes in magnetostatic energy arising from Meissner screening currents inside the superconductor [175–177]. It was shown that both of these phenomena were present inside the superconducting spin valve [178].

In the spin valve the free magnetic layer switches and rotates at very small applied field values (≈ 2.5 mT). Within the ferromagnetic layer are 360° domain walls. These are observed using the scanning Hall probe microscopy technique (SHPM), and are shown in figure 2.11. The stray fields from these domain walls create superconducting vortices which become pinned at defects in the polycrystalline Nb. This is because, although the superconductor is too thin to create screening currents in-plane, it is possible to set up surface screening currents to screen out-of-plane field components (emerging as stray fields from the domain structures). When the superconducting vortices become pinned, the magnetic domains are also locked in position and orientation. In the normal state, these domain walls switch or rotate with the bulk of the F layer. At $T<T_c$ the domain structures remain unchanged when an applied field of 10 mT is rotated through 180°.

The presence of stray fields from the ferromagnetic layers, the modification of the stray fields and the screening by the superconductor will become important in the discussion of the induced magnetisation effect in chapter 6.

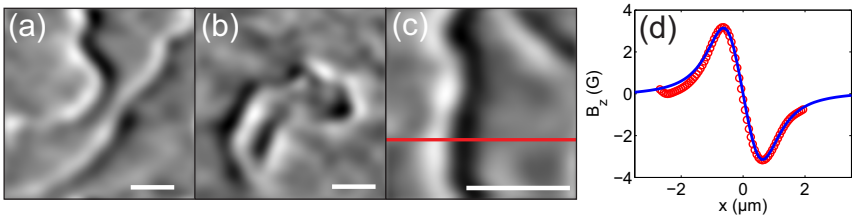

Figure 2.11: Typical SHPM images of 360° DWs in the 2.4nm free Co layer of our sample at remanence after saturation in positive fields at 77K, (a) and (b), and at 10K (c) (scale bars 5 μm). (d) Shows a fit to the line scan indicated in (c), using a 360° DW model. Reproduced from [178].

2.11 Conclusions

The phenomena of superconductivity and ferromagnetism were traditionally considered so highly competing that the fourth stated rule, of B. T. Matthias, for discovering superconductors (who himself discovered more than any other scientist) was simply "stay away from magnetism" [179]. As it turns out, there is a wealth of physics present at the superconductor/ferromagnet interface. While much of this physics originates from the competition, it has also been shown that complete synergy, via triplet proximity effects, is possible.

CHAPTER 3

Experimental Methods

3.1 Introduction

To access new physics at material interfaces, one must first force materials (which have no business existing naturally) together. To achieve this, metals in the thin film form are grown. In this thin regime, interfacial (as opposed to bulk) properties and their effects dominate the system. Metal deposition by the sputtering technique is outlined. Lab based characterisation of the thin films structural, electrical and magnetic properties are then discussed.

To study the nature of interactions at these interfaces, and ultimately to determine what proximity effects exist, it is necessary to make use of neutron and muon techniques at large scale facilities. This is due to the small measurement signals and length scales involved in the proximity effect. The PNR and LEμSR techniques are outlined. Two strategies are outlined to combine complimentary lab based and facilities techniques into a complete model of the S/F interfaces studied in this work.

3.2 Sputtering

Thin film deposition in this thesis is performed by DC magnetron sputtering over two systems. Once the samples are loaded, the system is roughed using a rotary pump and then evacuated to high vacuum overnight by a cryogenic pump. Liquid N_2 is pumped around the Meissner trap at least 90 minutes prior to growth. This is essentially a coil to which unwanted impurities (mostly water vapour) condense onto. A typical base pressure achieved after 90 minutes of N_2 cooling is 10^{-8} mbar for the first system and 10^{-7} mbar for the second (which has a much larger volume to pump).

Sputter deposition is the process where positive ions of an excited plasma are accelerated in an electric field towards a target. The target is composed of the material to be deposited, and the impact of the positive ions on the target is sufficient to cause the ejection of (neutral) atoms of the target material as well as free electrons. This ejection will take place at a random (but net uniform) direction. However enough are ejected towards the substrate to be incorporated in the new thin film. Behind the targets are high-flux permanent magnets which prevent the escape of the ejected electrons. The electrons are confined, increasing the plasma density and in turn creating a higher sputter rate.

By holding the substrate in a permanent magnetic field; magnetic layers can be grown with a preferential orientation (easy axis). This is defined as the anisotropy field (H_k). The atomic mass and pressure of the Ar will affect the sputter rate and the mean free path of an

ejected atom, respectively. They will both have an impact on the growth of the thin film, with a combination of these and the substrate temperature determining the surface mobility of the atoms as they arrive at the growing film. It is important therefore to aim for consistency between depositions. The specific case for deposition onto heated substrates (epitaxial sputtering) will be discussed in chapter 4.

The following preparation previsions are additionally undertaken in an attempt to produce sample to sample consistency; substrates are cleaned in an ultrasonic bath using acetone then IPA. Remaining moisture on the substrate is removed using compressed air. Any substrate with visible particles after cleaning is discarded. Target and substrate holders are cleaned prior to loading. Immediately prior to growth 'pre-sputtering' is performed. Non reactive targets are pre-sputtered for a minimum of 5 minutes to remove any impurities present at the surface, or any gas that has become trapped. Targets sensitive to oxidation are pre-sputtered for 15 minutes to ensure the removal of any oxide layers formed. Targets which are particular reactive or sensitive to contamination (Nb, Er, etc) are pre-sputtered for longer (typically 30 minutes). In addition to cleaning the target these reactive materials are getters to clean the local vacuum of water and oxygen in the region of the target, lowering potential contaminates and improving film quality.

Growth rates for each material are calibrated using fits to the Kiessig fringes in XRR measurements outlined in Section 3.5.2. Due to variations in the magnetrons and targets, each material must be re-calibrated for different targets and sources. Once this is done growth rates are consistent sample to sample in the same vacuum cycle, but may vary by small amounts between consecutive growths due to breaking vacuum and potentially having to remove the target from the magnetron.

This technique produces very high quality uniform films, with sharp interfaces. It is, however, very difficult to control the exact vacuum quality. Factors such as how long the system has pumped down, the efficiency of the Meissner trap, how warm the system was when opened previously (if it was too cold, condensation can get trapped inside), and the temperature of the cryogenic pump all have influence over the vacuum quality. For this reason when growing elements that are highly sensitive to vacuum quality, such as Nb and Er, it is not possible to directly compare samples deposited in different vacuum cycles. It is also difficult (but possible) to make direct comparisons between samples grown in the same vacuum cycle. Just as a pre-deposition getter improves local vacuum conditions, the process of sputtering will cause an improvement throughout a deposition. It is therefore

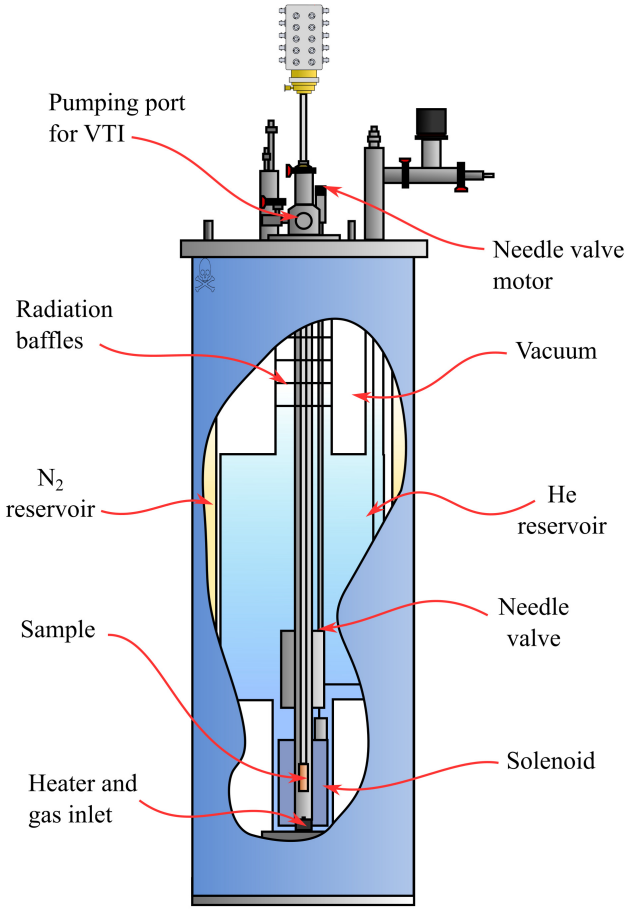

Figure 3.1: Schematic of a He flow cryostat used for magnetotransport measurements. Reproduced from [180].

quite common to observe an increase in film quality sample-to-sample in a deposition run. In this work several precautions are made to negate this, which are described in the relevant chapter.

3.3 Electrical Transport

All electrical transport measurements were performed in an Oxford Instruments ^{4}He flow cryostat, shown schematically in Figure 3.1. The system has outer vacuum and liquid nitrogen jackets to thermally isolate an inner ^{4}He reservoir. A Variable Temperature Insert (VTI) is placed into this reservoir and controls the sample environment. Additionally inside the

reservoir surrounding the VTI is a superconducting solenoid capable of producing fields up to 8 T.

The sample sits inside a sample head, which is interchangeable and application dependent, which is then mounted to a measurement stick containing the electrical lines. The sample stick and sample head are lowered from the top of the cryostat such that the sample sits in the centre of the coil. The VTI is evacuated with a roughing pump, which then pulls ^{4}He gas through the needle valve. The temperature can be controlled between 300 and 1.4 K using a combination of gas flow, pressure and applying a heater mounted at the base of the VTI.

Typically in this work the sample is first mounted inside a ceramic chip carrier package with electrical contact made by wire bonding from the chip package to the sample. The chip carrier is mounted in one of two sample heads, where in one the sample is aligned perpendicular to the applied field and the other parallel. Sample temperature is recorded from a Lakeshore 340 using a Cernox temperature sensor which is in thermal contact to the chip carrier and is mounted within the sample head.

Electrical transport measurements are performed via four terminals with a Keithley 6221 current source and a 2182 nano-voltmeter. These, along with the temperature and magnetic fields, are all controlled using custom software written in LabVIEW by Dr. G Burnell. The communication between the equipment and PC is through a GPIB to USB adapter.

3.4 Magnetometry

Lab based magnetometry measurements are performed in an Oxford Instruments vibrating sample magnetometer (VSM). The system's cryostat is very similar to that used for transport measurements. The VTI can be set between 2 and 300 K by controlling the flow of ^{4}He vapour and a heater.

The magnetic sample is placed between two pick-up coils and vibrated at a frequency of 55 Hz. It is first aligned to the coils by applying a constant field and moving the sample vertically through the coils. Due to magnetic induction, an EMF will be induced in the coils, the magnitude of which will be proportional to the magnetisation of the sample. The sample is aligned vertically at maximum induced EMF. A lock-in amplifier, with a 55 Hz reference signal from the vibrators driver, is used to pick up the signal at specified frequency. The system has a 6 T superconducting magnet. By sweeping an applied field and continuously measuring the EMF a full hysteresis loop of the magnetisation can be measured [182]. Background

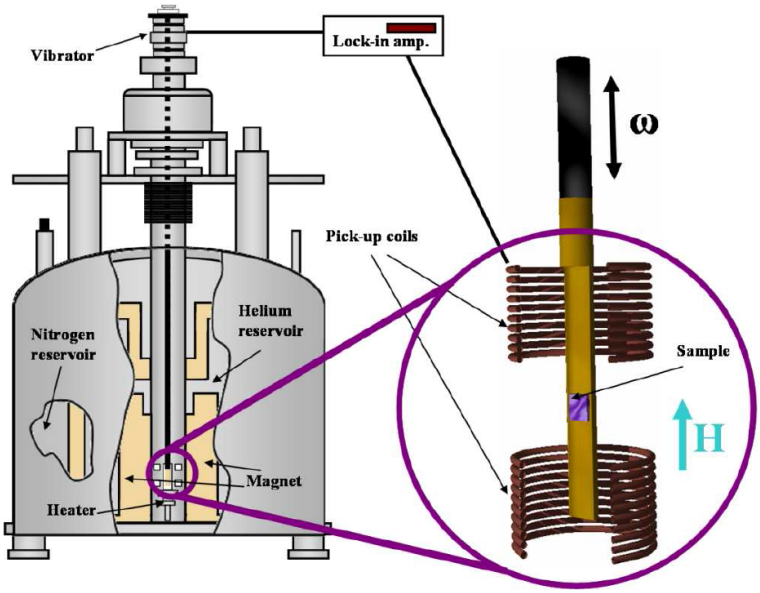

Figure 3.2: Schematic of the VSM in Leeds. Reproduced from [181].

signals from the substrate and probe must be subtracted from the loop. In addition, care is taken preparing samples to avoid surface contamination by magnetic impurities [183].

3.5 X-Ray Diffraction and Reflectometry

The characteristics of the scattered particle (X-ray or neutron) are determined by the mechanism responsible for the scattering. For an X-ray this is the electromagnetic interaction with electrons in the atoms shells. For each material the relative scattering is quantified by a *scattering length density* (SLD) function, with SI units m^{-2} (or in this thesis in units of classical electron radius (r_e) per $Å^3$), of the appropriate scattering material; nuclear, electromagnetic or dipole-dipole (magnetic). For the X-ray scattering in this section, magnetic scattering is negligible.

The geometrical set up for specular reflectivity is shown in Figure 3.3. This is the general case for a beam of incoming X-rays or neutrons, of wavelength λ impinges at a grazing angle θ on a planar sample, and the fraction which bounce back with the same attributes is ascertained. The specular scan consists of the coupled motion of the sample and detector arms such that the detector arm moves at twice the rate of the sample arm. This yields the

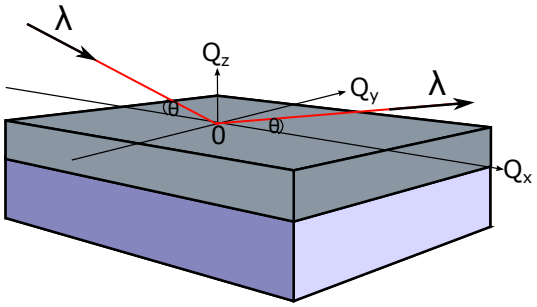

Figure 3.3: Schematic illustration of an X-ray or neutron, of wavelength λ, being reflected specularly, at an angle θ, from the surface of a layered sample.

reflectivity curve $R(Q)$, where [184]

$$Q_z = \frac{4\pi}{\lambda} \sin\theta. \tag{3.1}$$

3.5.1 Diffraction

In this work, X-ray diffraction (XRD) was used for structural phase identification and also to assess the quality of the crystallinity of the epitaxially grown films. It is the similarity of the X-ray wavelength and the characteristic separation of atomic planes in the solid state which enables X-rays as a means to probe the structure of matter. The basic principle of XRD is explained by Bragg's diffraction law [184]

$$n\lambda = 2d \sin\theta, \tag{3.2}$$

where by sweeping in 2θ and identifying points of constructive interference in the specular reflectivity (Figure 3.3), information about the lattice spacing, d, is obtained. This information is not limited to material identification, but also the determination of preferred crystallographic phases and alignments as well as the presence of strain and other deformities in the lattice.

An estimation for the crystallite size can be extracted from X-ray diffraction data using the Scherrer equation [185]:

$$\tau = \frac{K\lambda}{\beta \cos\theta}, \tag{3.3}$$

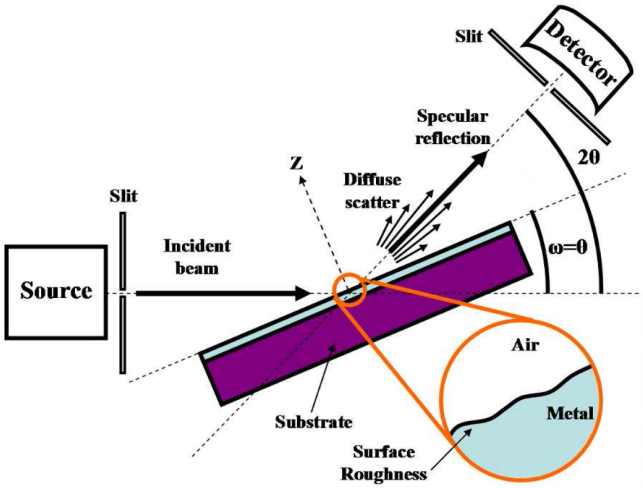

Figure 3.4: Schematic illustration of an X-ray diffractometer. Conventional $\theta - 2\theta$ geometry for low angle reflections from the surface of a thin film on a substrate. In the specular condition the detector angle, 2θ, is positioned at twice the sample angle, ω. Reproduced from [181].

where τ is the mean size of the ordered (crystalline) domains, K is a dimensionless shape factor (typically 0.9[1]), λ is the X-ray wavelength, β is the FWHM of the $\omega/2\theta$ peak (in radians) and θ is the Bragg angle. In the case of highly crystalline thin films, this gives an indication of the structural coherence length normal to the sample surface. In a thick enough thin film, with very high epitaxy, one can approach the true crystallite grain size giving an indication of the in-plane structural coherence.

3.5.2 Reflectometry

When performing a 2θ X-ray scan from 0°; below some critical angle total external reflection is observed. As the angle of incidence is increased above this critical angle a large reflectivity signal may be observed. Reducing the angle of incidence to these low angles creates a

[1]The Scherrer constant (K) depends on how the FWHM is determined, the shape of the crystal and the size distribution. Typically in thin films, values between 0.89 and 0.94 are used as this approximates a sphere with cubic crystal structure. K can actually vary from 0.62 to 2.08. If the in-plane crystallite size is known (eg. from SEM or AFM), the shape factor can be improved towards that of a cylinder (which more closely resembles the true shape of crystallite growth in a thin film). In this work, where the in-plane grain size is unknown and Gaussian modelling is used, $K = 0.9$ is used throughout for consistency. For a full description of K see reference [186]

special case where the angles of the scattering vector are approximately the same size as the layer thickness. This low angle reflectivity regime for X-rays generated by Cu K_α exists in the approximate region 1-10°. Above this, measured signals begin to return to the diffraction type. Away from the critical edge, reflected intensity falls off approximately as θ^{-4} or faster in the presence of roughness [184]. It is the rate of this fall off which allows the determination of a layer roughness.

For the simplest case of a single layer deposited on a substrate, Kiessig interference fringes are observed in $R(Q)$ [187]. They originate from the interference of the x-rays reflected from the surface and from the interface between the material and the substrate. The periodicity is used to determine the thickness t_{film} of the layer on the substrate, according to the Kiessig equation:

$$n\lambda = 2t_{\text{film}}\left(\sin^2\theta_n - \sin^2\theta_c\right)^{1/2}, \tag{3.4}$$

where θ_n is the angle of the n^{th} interference fringe and θ_c is the critical angle for total reflection. For a multilayer sample, many interference fringes sum to the total $R(Q)$.

3.6 Polarised Neutron Reflectometry

The basic principles of PNR are outlined in Blundell & Bland [188], the review articles by Majkrzak and Fitzsimmons [189, 190] and the book of Sivia [184]. For an overview of science conducted using neutron reflectometry on magnetic thin films and nano-structures the following review articles are recommended [191, 192].

3.6.1 Neutrons - Properties and Production

Neutrons are spin 1/2 neutral particles and as such are unaffected by the charge of orbital electrons. The de Broglie wavelength of thermal neutrons is comparable to the interatomic length scale. They interact with the nucleus of the atom via the strong nuclear force which, although powerful, acts only over very short distances. This gives the neutron the ability to deeply penetrate a sample and is the reason neutrons can be used to learn about the structural properties of a sample.

If some of the atoms in the material under investigation are magnetic the incident neutrons can be scattered by them through a spin-based dipole-dipole interaction. This type

of interaction is negligible in X-ray based scattering techniques, however with the neutron, nuclear and magnetic scattering occurs at a similar rate.

There are two sources of neutrons for science. The first is from a nuclear reactor, where (for example) 2 neutrons are emitted as the decay product of ^{236}U. The second is from a process called spallation. As results in this thesis were obtained at the ISIS spallation neutron and muon facility, it is this second source of neutrons which will be outlined.

In essence, a stream of high energy protons strikes a tungsten target, which results in neutrons, protons and other subatomic by-products being knocked out of the nuclei. Although this debris of ejected particles is too hot for application, less energetic secondary neutron emissions can be used. Unlike the continuous emissions from a nuclear reactor, at a spallation source neutrons are produced in short bursts. This enables the use of the time-of-flight technique. At ISIS a single pulse of neutrons in produced at a rate of 50 Hz at target station 1 and 10 Hz at target station 2.

3.6.2 Time-of-Flight Technique Outline

Scattering measurements in the time-of-flight set up are performed by considering the pulse of incoming neutrons as containing neutrons of many wavelengths. As opposed to considering a monochromatic source where $R(Q)$ scans are acquired by physically rotating the sample and detector, at a spallation source it is adequate to take a measurement of the time taken for a neutron to arrive at the detector, and then work out its corresponding wavelength, given by [184]

$$\lambda = \frac{h(t+t_0)}{m_n(L+L_0)}, \tag{3.5}$$

where t is the time, measured from target impact, at which the scattered neutron (of mass m_n) is detected after a flight distance L from the moderator; t_0 and L_0 are small offsets to be calibrated and h the Planck constant.

3.6.3 Experimental Set-Up on PolRef Beamline

The PolRef beamline has three modes of operation, neutron reflectivity, polarised neutron reflectivity and polarisation analysis.

Neutron reflectivity allows the SLD to be obtained. This is highly complimentary to XRR, but with the added advantage that neutrons are excellent for studying light elements which may not scatter x-rays.

The addition of a polarising mirror to the beamline separates the u and d neutrons, allowing only one spin state to reflect towards the sample. When scattering from a magnetic sample, the total scattering is proportional to the sum/subtraction of nuclear and magnetic scattering lengths (b)

$$b_{\text{total}} = b_{\text{nuclear}} \pm b_{\text{mag}}. \tag{3.6}$$

If an incident neutron enters a material it experiences a potential V_0, and if the material is magnetic then there is an extra potential V_{mag}

$$V_{\text{mag}} = \mu \cdot \mathbf{B}. \tag{3.7}$$

where μ is the magnetic moment of the neutron and $\mathbf{B}$ is given by,

$$\mathbf{B} = \mathbf{B_0} + \mu_0 \mathbf{M}, \tag{3.8}$$

where μ_0 is the permittivity of free space and $\mathbf{M}$ is the magnetisation vector. $\mathbf{B}_0$ is the applied field which does not contribute to the scattering, but does define the magnetisation direction. The polarised neutrons are sensitive to magnetism and the magnetic potential changes sign depending on if the polarisation is up or down with respect to the magnetisation. The consequence of this is that each spin state has a different scattering length in the magnetic medium. This is the basis for PNR and can be expressed as [193]

$$V_{\pm} = V_{\text{nuclear}} \pm V_{\text{mag}} = \frac{2\pi\hbar^2}{m} N(b_{\text{nuclear}} \pm b_{\text{mag}}), \tag{3.9}$$

where N is the density and m the mass of the neutron. The total scattering length now has a neutron polarisation dependence. The polarisation of the neutron beam is defined so that the plus sign (spin up neutron state) corresponds to a beam of neutrons polarised by a polariser with its magnetisation in the same direction as the sample magnetisation. When the beamline is polarised, half the flux is lost. Practically this means count times increase by a factor of 4.

When employing polarisation analysis four states are measured, uu and dd (the PNR non-spin flip channels) plus du and ud (the spin flip channels). While the uu and dd channels hold the same information as u and d before, the spin flip channels can be used to determine the magnitude and direction of the in-plane magnetic moments which may be

canted from the applied field. To perform this measurement very large area samples are required and count times increase by a factor 16. Polarisation analysis was not performed in this work.

3.6.4 Neutron Diffraction at Low Angle by Repeating Magnetic Structure

Although primarily designed for the purpose of low angle neutron reflectometry, the PolRef beamline can be used for neutron diffraction as long as the (magnetic) Bragg peaks are at low enough angles. For this the polariser is removed, and both spin states are simultaneously passed through the sample to increase flux.

Neutron diffraction essentially operates on the same principle as that of XRD described previously, but with two main differences. While XRD makes use of the monochromatic source, neutron diffraction takes advantage of the time-of-flight technique. Secondly as the neutron carries a spin it is able to interact with the repetitiveness of a magnetic lattice in an analogous way to structural diffraction. This magnetic diffraction produces interference effects which are superimposed onto the structural interference pattern. In materials with more unusual magnetic orderings, where the magnetic repeat distance is larger than the structural one, the magnetic diffraction produces a tighter diffraction pattern with each of the main structural Bragg peaks having multiple satellite peaks. It is the relation between structural and magnetic peaks which hold information about the relation between their lattices [159].

3.7 Combined XRR and PNR Fitting Technique (GenX)

In order to interpret results from XRR and PNR techniques a physical model of the sample needs to be built. Where possible in this work, the physical model of a samples structure satisfies data from a combination of XRR and PNR. All fitting is performed using the GenX software written by M. Björck, which is described in references [194, 195].

Within the fitting parameters are first the instrument properties. These are fixed by the technique or particular instrument employed and include; wavelength of particle, instrument resolution, incident intensity of the source and background signal.

With these fixed, a model for the sample can be built. GenX uses a layer model to build its SLD profile. Starting from the substrate (which is assumed to be infinitely thick) each layer is defined by scattering length density (SLD) (specific to each element with both real

and imaginary components), thickness and roughness parameters. For PNR there is an additional magnetisation parameter. These combine to provide a total depth dependent SLD for the sample.

While very attractive looking fits to experimental data can be achieved by allowing GenX free reign over the parameter space, such a fit is probably not a physical representation of the samples real parameters. It is therefore of importance to simplify the modelling of data to as few parameters as possible. Outlined below are each fitting parameter and steps taken to produce a physically meaningful final fit to experimental data. The first important tool in performing this are the maximum/minimum boundary conditions which are set on every free parameter during the fitting algorithm. Discussed below is the methodology as to how these boundary conditions can be set for each parameter.

GenX provides a scattering lengths library of all elements, for both X-rays and neutrons. Combining multiple elements in the scattering length can be used for alloys or other elemental mixtures. As the scattering length has both a real and imaginary component, it has to become two fitting parameters. In this work all elements and alloys employed have known scattering lengths and so these are not included as fitting parameters, rather are fixed to the nominal values [196, 197].

In GenX, the density is defined by atoms per $Å^3$. The actual calculations use the scattering length density, the scattering length multiplied with the density. Thus, how the scattering length is defined must be taken into account when defining the density. As the scattering length library is scaled by units of electrons (Thompson scattering lengths), this density value is used for convenience. This density can be calculated easily knowing the density in g/cm^3 and the molecular weight.

The density is a fitting parameter in a model, however for a continuous, uncontaminated layer the density is not expected to deviate significantly from the bulk value. Where a structure contains multiple layers of the same material a single density value is returned. For a reactive un-capped metal it is often found an interface region of reduced density is needed to be added to the model as the metal has become oxidised or abraded. The density of this layer is treated separately as it is not an isotropic layer.

Thickness is defined in Å. For most fitting, this is the most important parameter in the model. In thin film growth the sputter rates is one of the most controllable parameters during deposition of the films. It therefore expected there will be no large deviations from the nominal 'as grown' structure. Additionally limits can be set from calibration samples grown

in the same vacuum cycle or physical limitations such as thickness not being negative.

In specular scattering there are two main contributions to roughness. For a single interface these are surface roughness at a distinct structural boundary and inter-diffusion of two atomic species at a gradual graded boundary [198]. From purely reflectometry data it is not possible to distinguish between the two types of roughness. Rather a total RMS roughness is extracted from relectivity data as per Névot and Croce [199]. This can be thought of as an interface width. In this work, no inter-diffusion between layers is expected. A single roughness per layer is returned from the fits, this value corresponds to the top interface of the layer and is assumed to be roughness from distinct structural boundaries.

For PNR the additional magnetisation parameter is used. This is magnetic moment per formula unit of the density. A positive returned moment corresponds to the magnetisation of the layer being aligned in the same direction as the applied field. It is quite difficult to place lower limits on this value as the magnetisation of a layer is often suppressed in very thin films compared to the bulk, or a layer may contain magnetically dead interfacial regions. For most thin films it is reasonable to assume the magnetisation of the layer will not exceed the bulk value.

A good test for the physicality of a model is to directly transfer a structural model between XRR and PNR techniques with the ability to fit different magnetic configurations of the same sample by changing only the magnetisation in the magnetic layers. In practice the two techniques have slightly different sensitivities to roughness and so this parameter may need to be modified.

In summary a physical model should reproduce the experimental data set, with no large deviations from the 'as grown' structure or 'known' material parameters such as density and scattering length.

3.8 Low Energy Muon Spin Rotation (LEμSR)

Unlike X-ray and neutron based scattering, LEμSR is an implantation technique, where the probe (muon) comes to rest inside the sample. It is the decay of the at rest muon which gives information about the local implantation site. Bulk μSR has provided a wealth of information about superconducting properties, such as flux lattices in high T_c and exotic superconductors. Bulk μSR can also be used as a probe of magnetisation for magnetic samples. For a review of the applications of muons to condensed matter physics see Blundell [200]. The implantation energies involved in bulk μSR would cause the muon to simply pass through a

thin film. For this application a unique low energy μSR beamline was developed at the Paul Scherrer Institut (PSI) in Switzerland. For a review of this beamline see Bakule & Morenzoni [201].

3.8.1 Muons - Properties and Production

The muon is a second generation lepton with the same charge as an electron, but is 207 times more massive. For experimental condensed matter physics, the positive muon is used. This is because the negative muon tends to implant at the site of the nucleus, where as the positive muon will implant into the electron cloud (where the interesting physics takes place).

To produce muons, first high energy proton beams (provided at PSI by a cyclotron accelerator) are fired into a graphite target to produce pions via

$$p + p \rightarrow \pi^+ + p + n, \tag{3.10}$$

and the pions decay into muons

$$\pi^+ \rightarrow \mu^+ + \nu_\mu, \tag{3.11}$$

where ν_μ is a muon-neutrino. Using a particle physics trick, it is possible to produce 100% spin polarised muons in this decay. The pions are stopped in a target material. As their decay is two bodied, each decay product must have equal and opposite momentum. The pion has zero spin so the muon spin must be opposite to the neutrino spin. Due to the neutrino possessing a property called negative helicity, its spin is aligned antiparallel to its momentum, this implies the muon spin is similarly aligned. It is also possible to create a near monochromatic beam by selecting so-called surface muons. These muons are produced by positive pions that lost all their energy during the proton bombardment process and decayed at rest near the target surface. The reason these muons form a near monochromatic beam is that they all have a unique energy of 4.1 MeV and a momentum of 29.79 MeV/c. Negative pions cannot come to rest in a similar way (they are captured far deeper inside the target material), and thus all the produced muons are positive, monochromatic and 100% spin polarised. This 4.1 MeV beam is appropriate for bulk μSR, but far too high in energy for a thin film, as the muons stopping profile is about 0.1 – 1 mm. For a thin film the energy needs to be lowered to the keV range.

Once at rest inside a sample the muon decays with a lifetime of $\tau_\mu = 2.2$ μs as per

$$\mu^+ \rightarrow e^+ + \nu_e + \overline{\nu}_\mu. \tag{3.12}$$

The positron emission occurs preferentially along the muon spin direction. Unlike the two body decay before, there is not a single direction of emission, rather this preferential direction is characterised by a probability distribution

$$W(\theta) = 1 + (1/3)\cos(\theta), \tag{3.13}$$

which is an energy averaged value of the positron spectrum.

3.8.2 LEμSR Technique Outline

When a particle with magnetic moment is placed in a magnetic field **B** (where $\mathbf{B} = \mu_0\mathbf{H}$), the field will exert a torque upon the moment. This causes the process of Lamor precession around field **H** with frequency ω. For the muon this is given by

$$\omega_\mu = \gamma_\mu \mathbf{B}, \tag{3.14}$$

where $\gamma_\mu = 851$ MHz T^{-1} is the gyromagnetic ratio for a muon. When the sample is placed between two positron detectors, the value of **B** can be recovered by making a large number of single muon measurements of the decay product (positron) direction and time after implantation. The ability to follow the time evolution of the Lamor precession, of a muon experiencing **B**, makes the muon a local magnetic field probe.

A schematic illustration of the muon and positron detectors is shown in Figure 3.5. Practically in order to perform a measurement the muon must be detected prior to implantation (start signal at $t = t_0$). At this point the muons direction is pointing opposite to its direction of travel, and it arrives and is implanted in the sample pointing towards the left detector, with angle ϕ_0. Now at rest at the implantation site, the muon precesses clockwise with frequency ω_μ. After time t, the muon has rotated over an angle $\omega_\mu t$ and is now pointing in the direction $\phi(t) = \omega_\mu t + \phi_0$. The probability of muon decay at t is given by $(1/\tau_\mu)e^{-t/\tau_\mu}$.

If the muon decays a positron can be detected (stop signal) in one of two detectors. This detection must take place before the next muon enters the sample (to be sure the time after the start signal is valid). This is the first limitation on sample rate in the technique. The other consideration is that the detectors do not cover all possible angles, leaving a range of

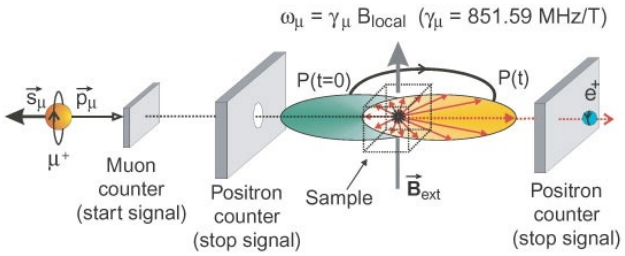

Figure 3.5: Schematic illustration of the muon beam end and sample space. The incoming muon polarisation, start counter and left & right positron detectors are shown. Reproduced from [201].

angles for which the emitted positron will not be detected, known as the 'dark-angle' which is parametrised by β.

To calculate the probability $P(t)$ that at t a positron is detected on the left (right) detector, the positron emission angle probability function ($W(\theta)$) is integrated over all values of theta that cause the positron to arrive at the left (right) detector, and multiply this by the probability that the muon actually decayed at that time. For simplicity in this work, the background corrected time spectra of positrons detected at the left (right) detector is given by the parameter $N_L(t)$ ($N_R(t)$). The time evolution of the muon spin polarisation along the axis of each detector is given by

$$N_L(t) = N_0 \exp\left\{-\frac{t}{\tau_\mu}\right\}\left[1 + A_0 P(t)\right], \tag{3.15}$$

$$N_R(t) = N_0 \exp\left\{-\frac{t}{\tau_\mu}\right\}\left[1 - A_0 P(t)\right]. \tag{3.16}$$

In Figure 3.6 the sum of the histograms show an exponential decay corresponding to the nuclear decay of the muon. Within this decay is a periodic oscillation as the spins are aligned preferentially towards one of the detectors.

The time evolution of this oscillation is the so-called asymmetry function, $A(t)$, determined as the normalised difference in signals observed by the two detectors:

$$A(t) = A_0 P(t) = -\frac{N_L(t) - \alpha N_R(t)}{N_L(t) + \alpha N_R(t)}, \tag{3.17}$$

where A_0 is the experimentally observed maximum asymmetry and α is a scaling factor if the two detectors have different efficiencies or the sample is not placed symmetrically. This value is typically slightly lower than the intrinsic asymmetry of the muon decay, which is the

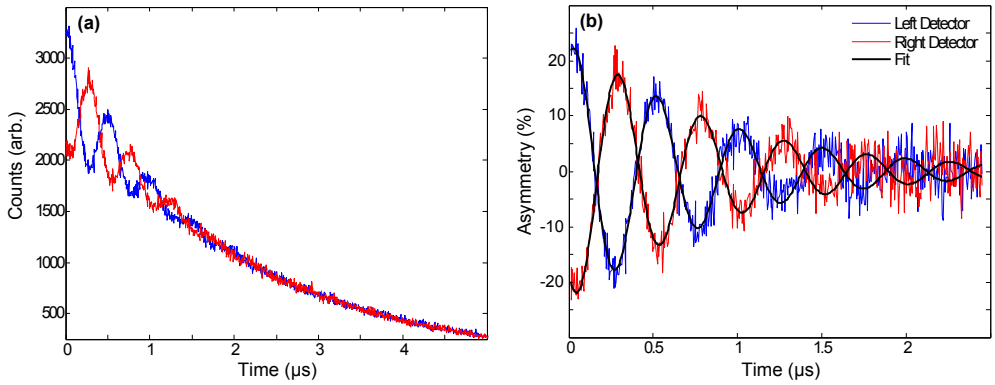

Figure 3.6: Data for a typical spin valve structure used in Chapter 6. Showing **(a)** detector histograms from the left and right detectors and **(b)** the extracted asymmetry of the histograms in **(a)**. The best fit results obtained to both signals are given by the black curves.

factor 1/3 in equation 3.13. It is $A(t)$ (or $P(t)$) which contains all the physical information about the muon precession, and thus the magnetic structure.

3.8.3 Experimental Set-Up on LEμSR Beamline

At PSI, high energy surface muons are generated and transported to individual beamlines. A schematic of the experimental set up on the LEμSR beamline is shown in Figure 3.7. This shows the beam energy point, moderation chamber, focusing and trigger chamber and the sample chamber. It is possible to isolate each chamber, which is important for the sample change process. All chambers are pumped down to UHV pressures ($< 10^{-8}$ mbar) as the high accelerating voltages involved can cause sparking at higher pressures.

Before becoming useful for thin film studies, the incoming surface muons of energy 4.1 MeV must first be moderated. The interactions of particles implanted in some well-selected materials (moderators) lead to a preferential emission at energies up to a few eV. This is achieved by injecting the surface muons into aluminium foil (of thickness 100 μm) which is covered in a 400Å argon cryosolid, which is in turn capped with nitrogen. What is essentially a thin film of solid argon is maintained at a temperature of 10 K. The energy lowering mainly occurs in the aluminium foil, while the argon film creates a minimum threshold value for the energy of the outgoing muons. This process does not alter the polarisation of the film, and so the outgoing beam of polarised muons can now be focused (by an electrostatic Einzel lens) and re-accelerated to appropriate energies for LEμSR. The final stage in the moderation

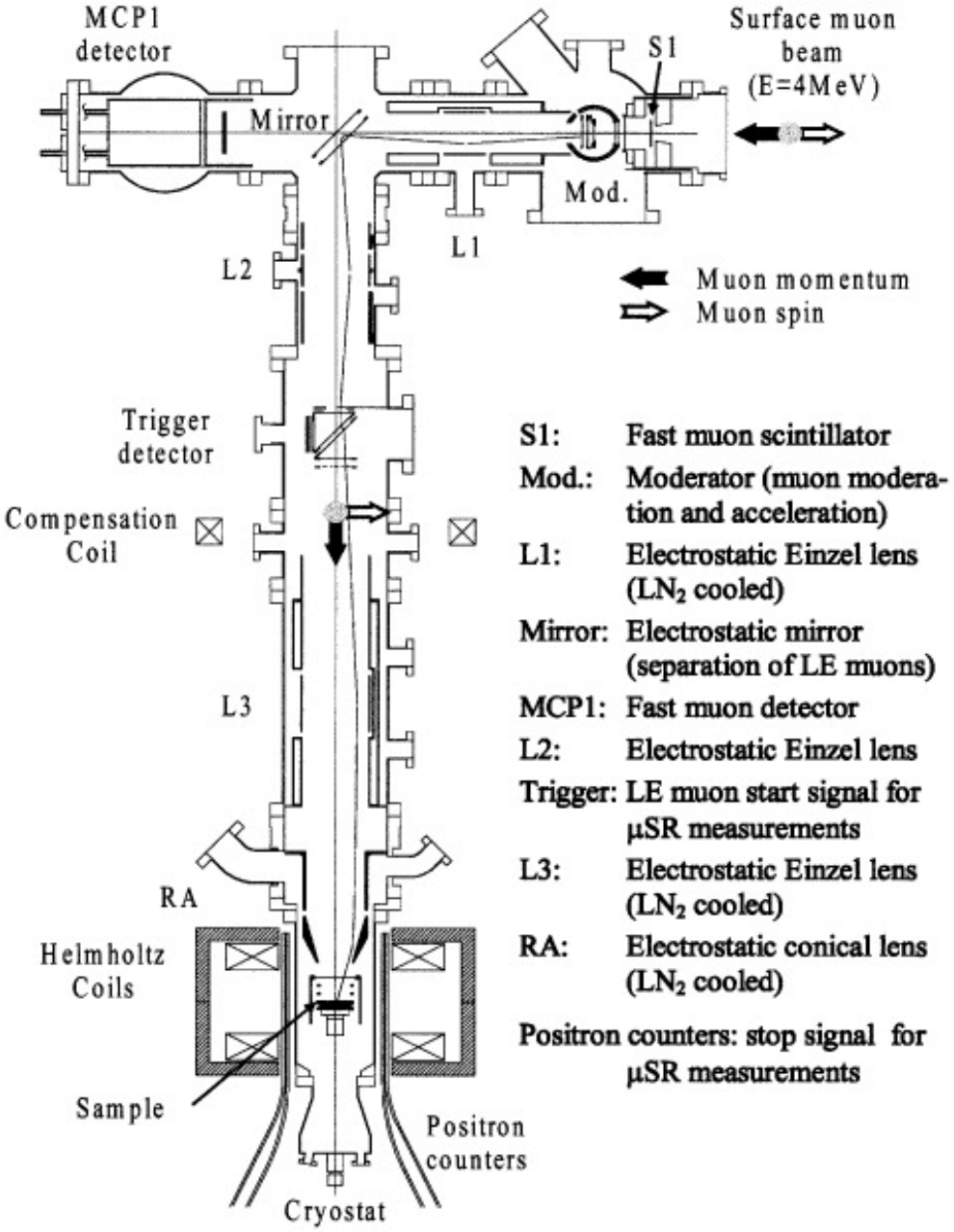

Figure 3.7: Schematic illustration of the muon beam line. Reproduced from [201].

process is to separate the low energy muons from the background surface muons. This is achieved with an electrostatic mirror which only reflects muons with energies of 10 or so eV. Muons of higher energies pass straight through to the MCP1 fast muon detector.

The low energy muon beam is focussed by a second electrostatic Einzel lens onto the trigger detector. Whenever a muon passes this detector the timer is started for a new (single) measurement. This measurement time is completed when the emitted positron is detected. Approximately 4500 muons per second are registered at the trigger detector, which means the time between muons is larger than the average lifetime. This helps ensure the requirement that a single measurement has been completed before the next incoming muon. The measurement event is aborted if the trigger detector is activated before the positron is detected or (as the positron detectors do not cover the entire area of possible emissions) 12.5 μs has passed.

A final Einzel lens is used to focus muons onto the sample. The sample is mounted onto a nickel plate, which is in turn mounted to a sapphire block. The nickel plate is chosen so non-implanted muons are de-phased and do not contribute to the measurement count. The sapphire block has the dual purpose of being a good thermal contact to the cold finger of the cryostat and it electrically isolates the sample and nickel plate. This allows the sample and nickel plate to be charged to high voltage ($\pm$12 KeV) which re-accelerates the incoming muons and determines their energy upon implantation, allowing the chosen stopping profile to be probed.

3.8.4 Fitting of the data

There are two general methodologies for the fitting of acquired data. The first is maximum entropy analysis, where a Fourier transform is applied to the asymmetry data to obtain a probability distribution of the local fields. The second involves performing a fit to the measured detector signals (the real-time raw data). It is this second approach which is employed in this work. Fitting is performed using a custom MatLab script written by Dr. M. G. Flokstra. The strategy of the program makes a best fit to the raw detector data using the Levenberg-Marquardt algorithm [202].

For a specified stopping profile, it is not possible to reconstruct the field distribution. When considering each implantation energy separately, a single average field value (<B>) per energy is obtained. This can be considered the field value at the mean stopping distance (<x>) for the profile. For low energies, where the stopping profiles are fairly concise,

this average field value is a good approximation of the local field profile. For higher energies, where the stopping profile can be spread across most of the sample, ignoring the spatial dependence of the field is clearly incorrect. The data is therefore modelled by taking all the collected histograms at different energies (at a single temperature) and fit all data simultaneously, imposing a single model for B and using the muon stopping profiles to correctly weight each 'slice of the sample. More details of the fitting script can be found in [203].

3.9 PNR and LEμSR

PNR and LEμSR are complementary techniques for the investigation of magnetic thin films. Together with XRR, PNR can help build a structural profile (density, thickness, magnetisation and roughness) of each layer in a multilayer sample. This is useful information for performing the necessary Monte Carlo simulations for determining stopping profiles of muons in the multilayer.

The two techniques probe magnetism is very different ways. LEμSR can only probe very weak ferromagnetism, as the muons are easily de-phased inside a ferromagnet, but has sensitivity of about 0.001 μ_B/atom as a local probe. PNR on the other hand is an excellent probe of large moment ferromagnetism and determining the samples total magnetic moment. Its sensitivity to magnetism within a layer is lower, however, limited to about 0.05 μ_B/atom before counting times become unreasonable.

PNR has the distinct advantage of being able to probe buried interfaces and gain magnetic information across the thickness of a sample. Additionally PNR has a very high spatial sensitivity ($\approx$ 10Å). PNR measures the magnetisation of each layer, although it is also possible to use it to measure flux vortices in superconductors [204]. The large moments associated with the ferromagnetic layers in this work make it difficult to see any small induced moments which may also be present in the system. LEμSR is an implantation technique and instead of measuring the layers magnetisation, has a particularly high sensitivity at implantation sites to small, local changes in magnetic field. Due to the spread of implantation sites at any given energy, LEμSR has a lower spatial sensitivity ($\approx$ 100Å), however with careful sample design the muons can be implanted in only the region of interest.

In this work a combination of PNR and LEμSR is employed on the sample structure. LEμSR is used to measure local changes in the external applied field in the superconducting state, the profile of which is then applied to data from PNR as a confirmation of similar changes observed in that technique. PNR can be used to look for changes in the total mag-

netisation of the sample, or additional moments at buried interfaces, inaccessible to LEμSR.

Thus the combinations of PNR and LEμSR is highly useful to find out the microscopic magnetic information for thin films which can provide both the spatial and magnetic resolution required to fully characterise the film.

CHAPTER 4

The Growth and Characterisation of Epitaxial Thin Film Erbium

4.1 Introduction

Magnetic inhomogeneity is the key component in generating the LRTC. To understand the role of intrinsic (as opposed to engineered) inhomogeneity, the rare earth (RE) metal erbium is studied. The RE metals possess complex magnetic properties, which have potential application to a range of emergent scientific areas, from enhanced spin-torque effects within microwave-frequency spin filters [205] to the generation of the LRTC for injection into Josephson devices [51].

Er is an example of a RE metal with a rich magnetic phase diagram. The realisation of application for Er depends upon having a fine control over its physical and magnetic properties. With the aim to incorporate thin film Er into S/F proximity structures, work was undertaken for this chapter on the growth and characterisation of sputter deposited epitaxial Er.

In this chapter, the work attributed solely to the author was all sample depositions, sample optimisation, X-ray characterisation, fitting to neutron measurements. Initial growth parameters were optimised by M. Batley. Neutron measurements were performed at the ISIS neutron and muon source, with the assistance of P. J. Curran, G. Burnell and local contacts C. J. Kinane and J. F. K Cooper. Magnetometry was carried out by the author and J. D. S. Witt. Temperature dependent XRD was carried out by the author and C. J. Kinane.

4.2 Magnetism in the Rare Earth Elements

Chapter 2 outlined the mechanism for exchange in the room temperature Stoner ferromagnets. This is often referred to as *direct* exchange because it arises from the direct Coulomb interaction among electrons from the two ions. This chapter introduces the RE ferromagnet Er. Magnetic interactions in the RE metals do not occur due to the direct exchange and do not satisfy the Stoner criterion. The origin of magnetic interactions comes between electrons in the partially filled $4f$-shells. The $4f$ electrons are very strongly bound, and their orbitals are highly compact. The spatial extent of the band is much smaller than the interatomic distance (so the overlap is very small), making the direct exchange almost non-existent.

The $4f$-electrons in the RE ferromagnets are coupled through their interaction with the conduction electrons. This mechanism is known as *indirect* exchange and can be stronger than direct exchange coupling. An explanation of indirect exchange was developed in 1954

by Ruderman and Kittel [206], which was later refined and expanded by Kasuya [207] and Yosida [208] to what is now referred to as the RKKY coupling interaction. In the formalism of exchange presented in Chapter 2, the RE ion at site i creates a local field, $\mathbf{h}_i = J\mathbf{S}_i / g\mu_B\mu_0$. When a conduction electron is in the vicinity of the RE ion, it interacts locally with the $4f$ electrons. This interaction spin-polarises the conduction electron, which propagates the polarisation through the lattice to any point j. This magnetisation of the conduction electrons at site j, associated with the initial field $\mathbf{h}_i$ at another site, is described by a susceptibility χ_{ij}. The induced magnetisation can be written $\mathbf{m}_j = \chi_{ij}\mathbf{h}_i$ and is the indirect interaction between spins on the two sites. Considering this now as an exchange interaction:

$$E_{Ex} = -J^2\chi_{ij}\mathbf{S}_i \cdot \mathbf{S}_j / \mu_0 (g\mu_B)^2. \tag{4.1}$$

The sign of the magnetic interaction depends upon the susceptibility χ_{ij} which is distance (r) dependent and gives [24]

$$E_{Ex} \propto \frac{\cos 2k_F r}{r^3}, \tag{4.2}$$

where k_F is the radius of the Fermi surface. For free electrons this interaction acts at long distance and for RE metals χ_{ij} oscillates spatially between being positive and negative. Therefore depending on r the interaction can be ferromagnetic or antiferromagnetic. This long range oscillation in Er and other RE elements leads to long period magnetic structures, which can be incommensurate with the lattice spacing.

4.3 Erbium

Er is a trivalent RE metal (Z=68), with highly localised 4-f electrons and hexagonal close packing (HCP) crystal structure. Similar to its neighbour holmium, it has a very large magnetic moment ($\approx 9\ \mu_B$/atom). Competing interactions within the material creates an exotic magnetic phase diagram, the subject of which will be studied in the thin film form in this chapter.

The most important magnetic interaction in Er (like other heavy RE metals), is the isotropic RKKY exchange interaction. This results in a minimised free energy when the ferromagnetism consists of sheets perpendicular to the c-axis, with the moments rotating through a certain angle from one sheet to the next. Competing with this is the crystalline anisotropy in the HCP structure, which favours magnetic alignment either along or perpendicular to

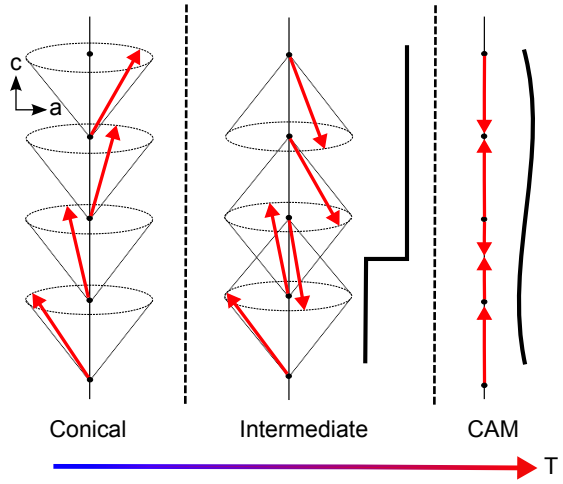

Figure 4.1: Schematic showing the magnetic structure as a function of temperature for bulk Er.

the c-axis. In the latter case, for example in holmium, this results in an in-plane helix magnetic structure. In the former case, the strength of this anisotropy becomes more important. If strong enough, alignment perpendicular to the c-axis becomes completely suppressed, for example in thulium. In Er, this crystalline anisotropy is weaker than for thulium, resulting in an initial ordering of moments parallel to the c-axis, followed at lower temperatures by a canting out of the c-plane driven by crystalline anisotropy [209]. To recover the bulk magnetic phases of Er in thin film, the crystallographic quality of the film is very important.

Bulk Er has three distinct magnetic transitions. Within the three magnetic phases there are many other reproducible (but metastable) commensurate states. Below the high temperature paramagnetic phase ($\approx$ 85 K) Er first gains a sinusoidal, c-axis modulated (CAM) antiferromagnetic phase with a wavelength of about 7 atomic layers (which is traditionally labelled by the magnetic wave vector $\tau_c = 2/7$, in units of reciprocal lattice parameter, c^*). As the temperature is lowered the magnetic wave vector of the CAM peaks at $\approx$ 52 K. Below this temperature Er enters an 'intermediate' phase where the in-plane moments begin to order creating what has been referred to by Cowley *et al.* as an antiferromagnetic "wobbling cycloid" [209]. The magnetic repeat distance increases with decreasing temperature, through a number of stable commensurate phases, to 8 atomic layers ($\tau_c = 1/4$). These states exhibit a ferrimagnetic moment. Finally, below 18 K a conical c-axis ferromagnetic phase is formed with a wavevector ($\tau_c = 5/21$), as summarised in Figure 4.1. The formation of this lowest temperature phase is accompanied by a small expansion in the c-axis lattice parameter.

The three main magnetic transitions were identified in bulk samples using neutron diffraction in the 1960's by the group of Cable *et al.* [210], however the exact ordering of the intermediate phase remained an open problem. Neutron and x-ray scattering techniques in the 80's and 90's finally revealed the multitude of commensurate and incommensurate spin structures within the intermediate phase [209, 211–214]. These phases were additionally confirmed by the group of N. Ali *et al.* using magnetometry and transport techniques [215–217].

Previous work on thin film Er has failed to show the recovery of the low temperature bulk-like conical phase, even in films as thick as 1 μm[218–221]. It was clear from these works that the magnetic structure was extremely sensitive to in-plane strain. To date all previous work has used molecular beam epitaxy (MBE) to deposit films. While this technique produces high-quality films, it is not ideal for incorporation into heterostructures or nanodevices due to the low sample throughput and requirements of ultra high vacuum. In this work for the first time DC magnetron sputtering onto heated substrates has been employed for thin film growth of Er with the aim to exploit the varied magnetic properties in hybrid S/F heterostructures.

4.4 Epitaxial Growth

Up until now, this work has only considered sputter deposition at ambient temperature. While this method still produces high quality samples (from the point of view of having sharp interfaces) the low surface mobility of deposited atoms means that crystal ordering is unfavourable. Depending on the element in question, this leads to either amorphous films with no crystal ordering, or polycrystalline films with possibilities of mixed growth phases and small grain sizes.

By performing deposition at high temperature (typically 1/3 the melting point of the material) it is possible to increase the surface mobility of the deposited atoms enough to promote the nucleation of single crystal phase. This is described as the epitaxial growth condition. A homoepitaxial grown film maintains the crystallographic alignment of the substrate upon which it is grown. Where the texture of a film takes crystal ordering from the previous layer (in a multilayer) it is of the heteroepitaxial growth type.

Using previous work [220–222] as a guide, *c*-plane Al_2O_3 substrates are used, and the growth of a thin Nb seed/buffer layer on the substrate precedes Er growth. Nb is chosen for three reasons; firstly, it is known to grow with good epitaxy in the (110) phase on sapphire.

Growth Temperature (°C)	Er (002) FWHM (°)	Structural coherence
700	0.71	39%
600	0.35	79%
550	0.31	90%
500	0.30	93%
450	0.34	81%

Table 4.1: The FWHM for the 2θ scans and the calculated structural coherence (see text) for a 30 nm Er film varying deposition temperature.

Secondly, it has very little reaction with RE metals and acts as a buffer to stop Er from reacting with oxygen from the substrate to form Er_2O_3. Finally it is a superconductor, which is advantageous in the context of this thesis. A Lu capping layer to prevent oxidation of the Er is chosen for good lattice matching between materials.

The Er grows epitaxially on the most densely packed Nb (110) plane, in the Nishiyama-Wasserman orientation. The in-plane axis of hcp Er [$10\bar{1}0$] is aligned with bcc Nb [$\bar{1}10$] with 3:4 supercell commensuration in their nearest-neighbour distances along these axes [222].

4.4.1 Optimal Growth Parameters

All films were deposited using DC sputtering as described in Chapter 3 with the addition of substrate heaters on the sample wheel. At the highest temperature of 700°C the base pressure of the system was 10^{-7} mbar, however this pressure improved towards lower temperatures. Samples in this chapter were grown onto 0.65 mm thick c-plane Al_2O_3 single-side-polished substrates which were annealed overnight at the maximum temperature for the system. Growth was performed at a typical Ar flow of 55 sccm and partial pressure of 2-3 μbar, a substrate-sample distance of 70 mm and at a typical growth rate of 0.1 nm s^{-1}.

Initial investigation focussed on optimising the growth temperature for the Nb buffer and Er layers. The Nb film quality improved in crystallinity, morphology and superconducting T_c as the growth temperature was increased. The highest heater temperature of 700°C was lower than the ideal Nb deposition temperature of 900-950°C [222], but was used for the rest of this work.

Next the growth temperature of the Er layers was considered. Table 4.1 shows the temperature dependence of the structural coherence (determined using the Scherrer equation

3.3) of the (002) peak for 30 nm Er films, deposited on 10 nm Nb buffer. The highest epitaxy was achieved for films grown at 500 and 550°C. Although both temperatures appear to give an almost identical structural coherence, careful examination of the XRD data (not shown) revealed that the growth texture entered a mixed phase at 550°C, and began to favour Er (100). In addition, all films grown above 500°C showed a significant increase in Er_2O_3 contamination. 500°C was chosen as the optimal deposition temperature for this study. Growth of a Lu capping layer at this temperature, immediately following Er deposition, provided good protection from oxide contamination. It was also unlikely to cause any strain to the film as it has good lattice matching and has previously been used as a seed layer [221]. Thin Nb or Ta caps were found to be ineffective at protecting the reactive Er from oxidation, possibly due to a tendency to grow as islands and not continuous layers. Alternatively, a thick Nb (10 nm plus) layer can be used to ensure coverage.

For the rest of this chapter, the properties of a set of 5 samples are considered. They were grown in the same vacuum cycle, under the previously determined optimised growth condition. They all have 10 nm Nb buffer and 5 nm Lu capping layers. They are identified by the thickness of the Er layer (5, 10, 20, 50, 200 nm).

4.5 Structural Properties

Structural characterisation was performed using XRD, as shown in Figure 4.2. All samples show strong structural Bragg peaks, identified in the figure, and somewhat reassuringly there is no evidence for Er_2O_3 in any film. The 50 nm film appears to be somewhat of an anomaly and has grown more polycrystalline. This can be explained if the heater bulb above this particular substrate was faulty during growth, reducing the substrate temperature.

The full-widths at half-maxima (FWHM) for the principle peaks of Nb (110) and Er (002) are shown in Table 4.2. Using the Scherrer equation 3.3 structural coherence perpendicular to the plane is estimated. Strain analysis may be carried out by considering the position of the Bragg peaks compared to the ideal case (from powder diffraction). For the Er films in heteroepitaxial growth, lattice mismatching between Nb and Er will translate a Bragg peak from the ideal angle (to smaller angles if the lattice is being stretched and to higher angles if compressed). Non-uniform strain can cause the peak to broaden and may be mistaken for a reduction in grain size. In this work the Er is between two layers (Nb and Lu) with similar lattice constants. It is therefore assumed any strain is uniform.

Figure 4.3 shows the thickness dependence of the *c*-axis lattice spacing at 300 K. All films

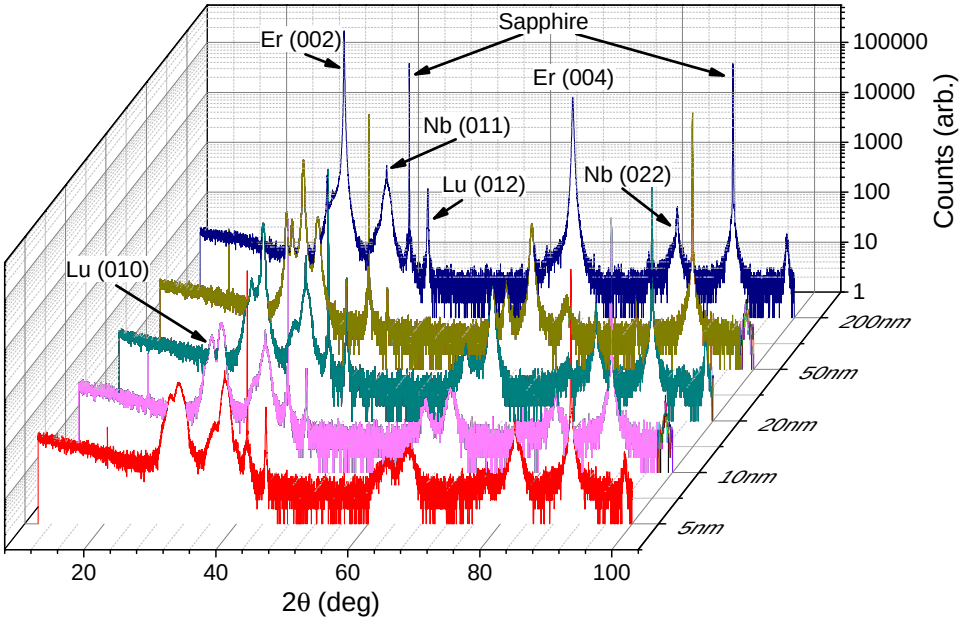

Figure 4.2: XRD of all films studied in this chapter with main structural peaks identified. The instrument was aligned to the samples surface.

Er thickness	FWHM (°)		Structural
(nm)	Nb(011)	Er(002)	coherence (nm)
200	1.15	0.09	98.1
50	*	0.28	32.7
20	1.15	0.44	20.8
10	1.26	0.95	9.7
5	1.16	1.52	6.0

Table 4.2: The FWHM for the 2θ scans and the calculated structural coherence. (*see text.)

show signs of strain, increasing the lattice spacing from the bulk value. As to be expected, the thinnest samples show the largest strain, which changes with thickness and has settled by 50 nm.

The FWHM for the main peaks in Figure 4.2 are shown in Table 4.2. Nb grain sizes range from 7.3-8.1 nm, indicating very high structural coherence and consistency between samples. For the thinnest Er films, the structural coherence is very close to the layer thickness, indicating strong epitaxy. Considering next the 50 nm film, the Nb structural phase was clearly different in this sample than the others. Figure 4.2 shows almost no detectable peak where the Nb(001) phase is expected. This is possibly due to a reduced heater temperature during growth. This caused the Er film to have a reduced structural coherence and a mixed growth phase. A strong secondary peak of Er(011) is observed, with a comparable structural coherence of 29.5 nm. Finally the structural coherence of the 200 nm sample is 98.1 nm. This is probably approaching the true crystallite grain size.

4.5.1 Temperature Dependent XRD

Temperature dependent XRD is possible using the Rigaku SmartLab with an Oxford Phenix cold stage. The temperature dependence of the Er(002) peak position for the 200 nm thick sample in the temperature range 12 - 300 K is shown in Figure 4.3. Firstly, the lattice parameter at all temperatures is higher than bulk (solid line). Taking this offset into account, the temperature dependence is qualitatively similar to that of bulk Er. In both the thin film and and bulk samples there is a structural transition at $20-22$ K, where the lattice parameter abruptly changes. This is related to the first order transition into the low temperature ferromagnetic phase.

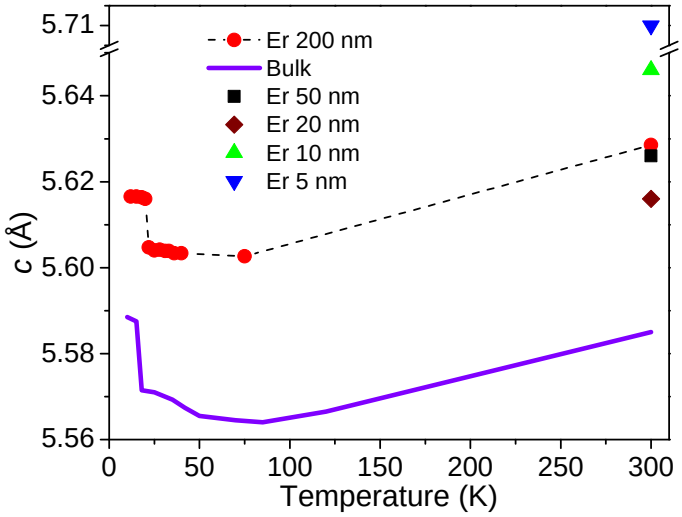

Figure 4.3: The *c*-axis lattice spacing for the 200 nm thick Er film with the bulk behaviour shown. The thickness dependence at 300 K is also shown. Dashed line is a guide for the eye

It has been shown previously [159] that Nb grown on *c*-plane sapphire contracts smoothly and isotropically with decreasing temperature. Over this temperature range, the contraction is in good agreement with Nb (and the sapphire) thermal expansion coefficient. No structural transitions of the type observed in the Er are expected for the Nb, Lu or sapphire.

4.6 Magnetic Characterisation

Figure 4.4 shows OOP magnetometry for the 200 nm thick sample acquired at an applied field of 200 mT, from 120 to 5 K obtained with the Oxford VSM apparatus. It is possible in the data to see the transition from paramagnetic, through antiferromagnetic, to a ferromagnetic state.

The first transition is characterised by the 'bump' in the magnetisation near 80 K, corresponding to the paramagnetic to CAM antiferromagnetic phase. The next feature occurs at around 20 K, where the magnetisation of the film sharply increases. From what is expected for bulk crystals, this is most likely due to the formation of the conical ferromagnetic phase. The phase transitions visible in the magnetometry data occur at temperatures very close the bulk transitions at 85 and 18 K respectively.

There is a noticeable temperature hysteresis between the cooling and warming data, as

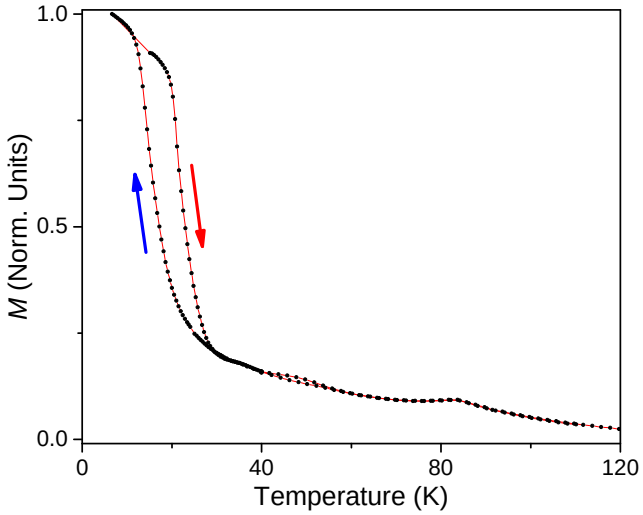

Figure 4.4: Normalised Moment with temperature for the the 200 nm thick Er film measured at a field of 200 mT and a cooling rate of 5 K/minute.

indicated by the blue (cooling) and red (warming) arrows. This was reproducible even with very slow temperature ramping (1 K/minute), and is therefore a property of the film rather than artefact of the measurement. In Er, this temperature hysteresis is to be expected and is a common feature of both bulk [213] and MBE grown films [221].

Hysteresis loops for the films are shown in Figure 4.5 for both OOP and IP orientations at 2 K. The most notable observation is the presence of Meissner screening at low fields, particularly for the 20 nm sample. This confirmation of superconductivity in the 10 nm thick Nb layer confirms the high quality of the buffer layer. As these samples were not designed to be superconducting (10 nm is typically too thin for Nb to become superconducting when adjacent to a ferromagnet), it is quite surprising that the Meissner state was observed in any sample. This is encouraging for the prospect of producing hybrid S/F devices.

With the exception of the OOP measurement of the 200 nm thick sample, the maximum applied field of 6 T did not fully close the loops. In all films the loops are not square-like and the Er shows very small remanent magnetisation. This is due to the Er re-forming the conical or helical magnetic state upon relaxation of the field, instead of retaining ferromagnetic behaviour. This behaviour is quite different to holmium, which in thin films saturates IP at fields of typically only 300 mT, after which the squareness of its hysteresis loop suggest

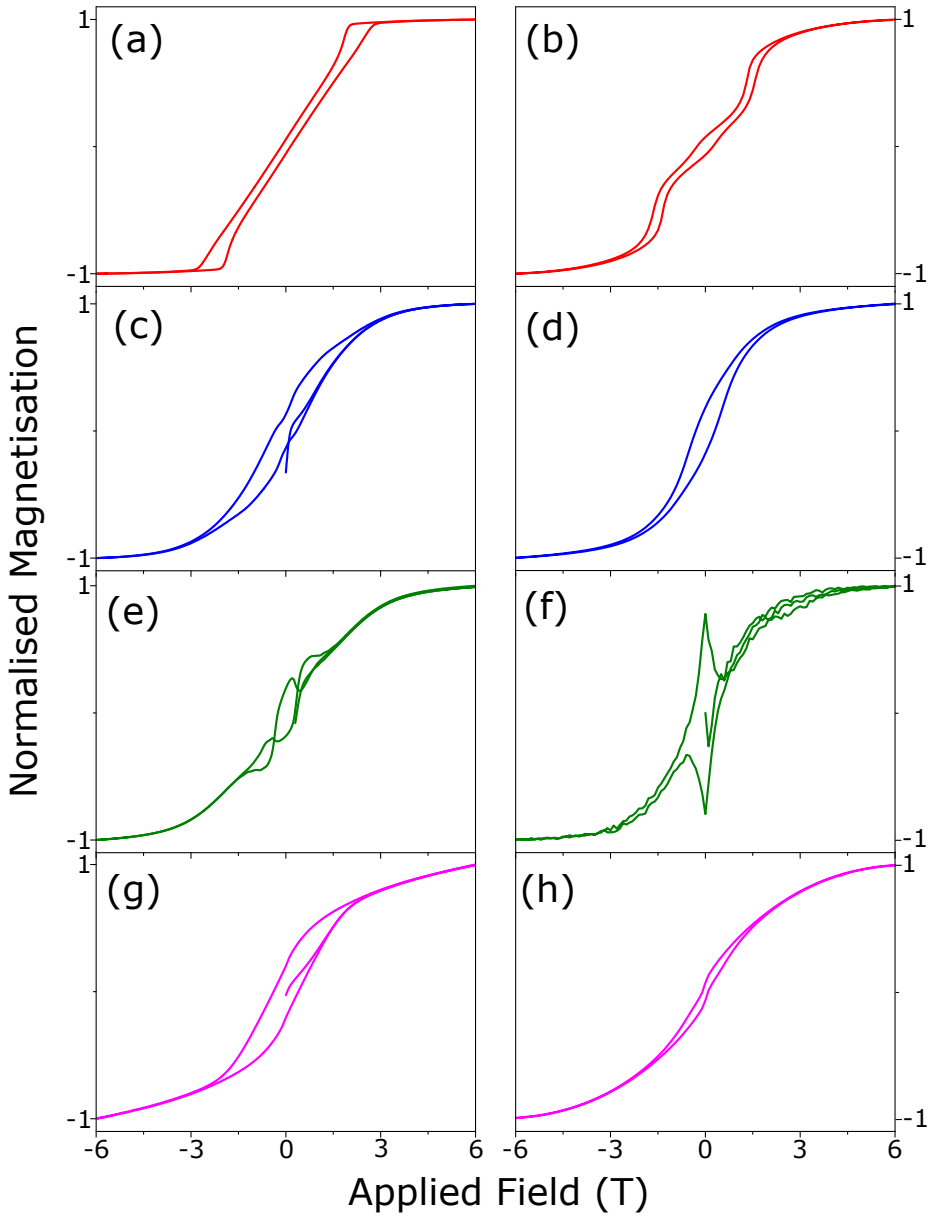

Figure 4.5: Normalised magnetic hysteresis loops for the **(a)**-**(b)** 200, **(c)**-**(d)** 50, **(e)**-**(f)** 20 and **(g)**-**(h)** 5 nm films in out-of-plane (left hand column) and in-plane (right hand column) sample alignment, measured at 2 K. In the 20 nm sample the Nb buffer layer has become superconducting with the Meissner response dominating the signal at low fields.

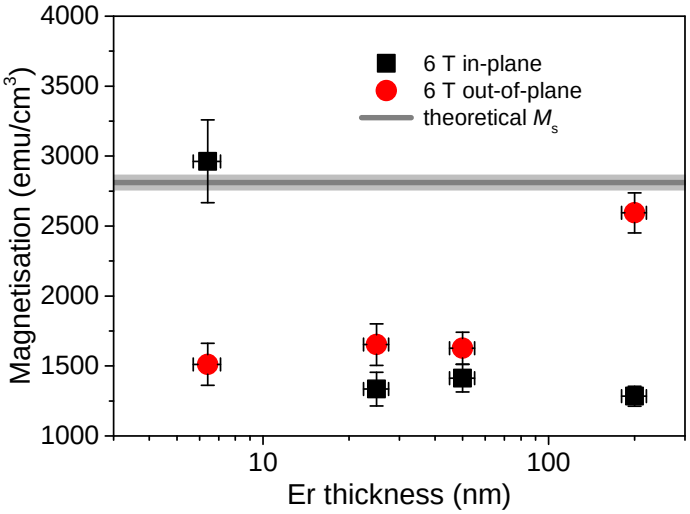

Figure 4.6: Magnetisation at "saturation" in an applied field of 6 T at 2 K for in-plane and out-of-plane field orientations as a function of Er thickness. The theoretical maximum is also shown.

a ferromagnetic ordering takes over and the spiral magnetism does not reform [151]. This difference is most likely due to the *c*-axis crystalline anisotropy in the HCP structure being more important, or certainly being retained to a greater extent, in thin film Er.

From these data, the OOP and IP magnetisation at 6 T and 2 K for all Er thicknesses are extracted and plotted in Figure 4.6. The 200 nm thick sample exhibits bulk-like behaviour, with the OOP magnetisation approaching the theoretical maximum, ≈ 2700 emu cm^{-3} (grey line). The IP magnetisation reaches only approximately half this value. As with bulk, the IP components will not reach more than $\approx 3/5$ saturation until an applied field above 10 T. This IP magnetisation remains constant for the 50 and 25 nm thick samples, however the OOP magnetisation becomes suppressed. This is probably due to the suppression of the conical ferromagnetic phase, consistent with other reports of thin films in literature.

The 5 nm sample has a markedly different behaviour. In this thickness range there is a switching of the magnitude of the two components, with the IP magnetisation now much larger than the OOP magnetisation. While the OOP magnetisation is similar to that of the 25 and 50 nm thick films, the IP magnetisation is close to the theoretical maximum. This is a strong indication that, for this thickness range, the RKKY interaction at the interface is weakened, making the film more susceptible to IP fields, and saturating completely along this direction. The reason why this occurs only in the thinnest sample, is the dominance

of surfaces disrupting the long ranged RKKY interaction. The weakening of RKKY interaction at the surface makes these moments easier to rotate. This in turn causes the nearest neighbours to align with the field, until the spiral has completely unwound and the sample is saturated. For the samples which are not dominated by the surface, the RKKY interaction is simply too strong in the available field range.

From these measurements, it was not possible to extract the exact magnetic phase of the Er. For this, neutron diffraction was performed.

4.7 Neutron Diffraction

As outlined in section 3.6.4 it is possible to use the PolRef beamline at ISIS to observe low angle magnetic Bragg peaks. In the case of Er this will be the observation of the spiral $(000\tau_c)$ peak. The value of τ_c can be related to the magnetic repeat distance in the c-axis direction. When expressed in units of the reciprocal lattice parameter, $\tau_c = l/n$, where n is the number of c-axis lattice parameters within which l full magnetic repeats are contained. Neutron diffraction was performed on the 200 and 50 nm thick samples. In addition neutron diffraction was attempted on the 5 nm thick sample, however the $(000\tau_c)$ peak was too weak. This was not too surprising since its thickness would not allow many repeats of the magnetic structure for neutrons to scatter off. Due to constraints of allotted beamtime, the other samples were not measured.

Figure 4.7 shows the variation in the $(000\tau_c)$ peak as a function of temperature for the 200 nm thick Er sample. The data at each temperature are well described by the Gaussian distribution function, which is used to determine peak positions (Bragg angle) in addition to giving an integrated intensity of the peak, plotted in Figure 4.8.

Figure 4.8 shows the magnetic wavelength (in units of the reciprocal lattice vector) as a function of temperature for the 200 nm and 50 nm Er samples. Also plotted is the bulk behaviour and expected commensurate states. For the 200 nm sample it is clear that τ_c increases for increasing temperatures, in a way that is qualitatively similar to bulk. The slight increase in transition temperatures at which the main magnetic transitions occur can be explained by the temperature hysteresis observed in Figure 4.4.

In previous reports on MBE grown thin films it was not uncommon for the conical ferromagnetic state to be completely suppressed [221]. This appears to be the case for the 50 nm film, which reaches at the lowest temperatures the commensurate $\tau_c = 1/4$ state. At higher temperatures the signal from this sample became too weak to detect.

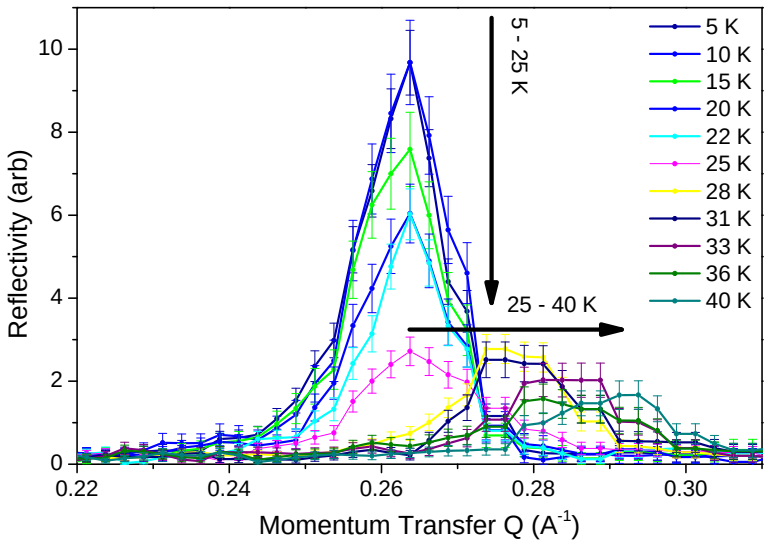

Figure 4.7: The momentum transfer versus the intensity of the magnetic diffraction peak for the 200 nm thick Er sample as a function of temperature. Lines through the data are as a guide for the eye.

It is also not uncommon for thin films to have commensurate states inconsistent with bulk behaviour. The most interesting part of the data in figure 4.8 is the attainment of a hitherto unseen magnetic state. At temperatures below 25 K the 200 nm sample has 'locked in' to a $\tau_c = 4/17$ commensurate state. This corresponds to a magnetic repeat distance of 8.5 atomic layers in the c-axis. This is the first report of the recovery of the conical ferromagnetic state in thin film Er of any thickness or growth method.

The integrated intensity of the magnetic Bragg peaks is directly related to the magnetisation, $I \propto M^2$, which is in turn related to the degree of order within, and the temperature of the sample. For the 200 nm thick sample a clear variation in the $(000\tau_c)$ peak with temperature is visible. From both the peak height in Figure 4.7 and the integrated intensity in the top part of Figure 4.8, the $(000\tau_c)$ peak is approximately constant between 5 and 10 K, before becoming weaker with increasing temperature. This has strong implications for the design of Er based devices. In the temperature regime that one would be interested in for superconductor applications, this result shows that there is no change in the magnetic properties of the Er.

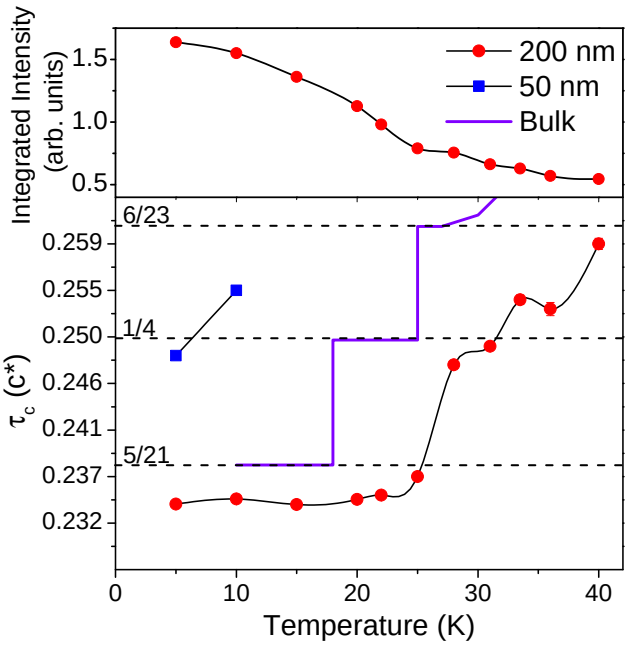

Figure 4.8: Top: The integrated intensity of Gaussian fits to the data in Figure 4.7 for the 200 nm sample. Bottom: the magnetic wavelength (in units of the reciprocal lattice vector) as a function of temperature for the 200 nm and 50 nm Er samples. Also shown are the values for bulk single-crystal (solid purple) and the commensurate bulk phases (dashed horizontal lines). Lines through the data are as a guide for the eye.

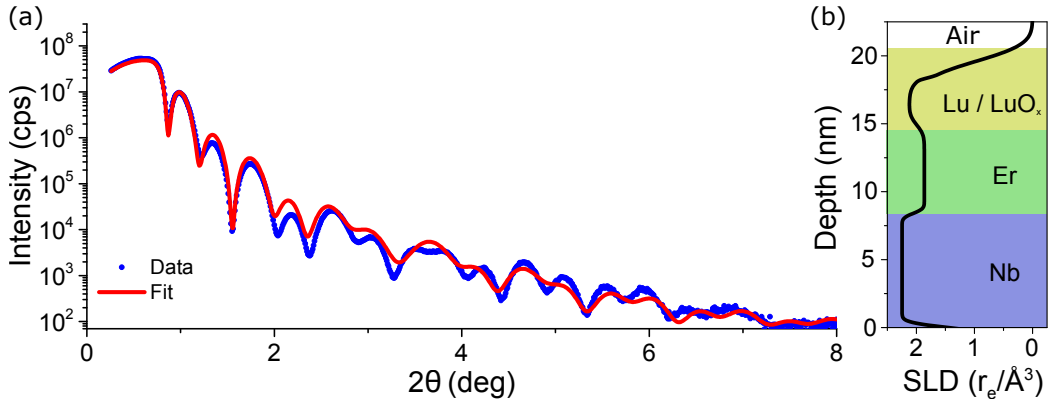

Figure 4.9: (a) Low-angle X-ray reflectometry and corresponding fit. **(b)** The SLD (in units of classical electron radius (r_e) per Å^3) with depth from the fit in (a). The returned fit parameters are given in Table 6.1.

4.8 PNR of 5 nm Thick Sample

The magnetic $(000\tau_c)$ Bragg peak in the 5 nm thick sample was too stretched and so did not give a detectable signal. For this sample the PolRef beamline was returned to its polarised state, and PNR was performed on the sample to extract detail about the magnetism. Measurement was performed at 5 K where any signal would be largest.

4.8.1 X-ray Reflectometry

The nominal *as-grown* structure was Al_2O_3 (substrate) / Nb (10 nm) / Er (5 nm) / Lu (5 nm). The XRR data and model fit from this representative sample can be seen in fig. 4.9. The extracted parameters are shown in Table 6.1. There is good agreement between the modelled values and the nominal structure, however the Er layer is slightly thicker than expected. The interfacial roughness is small for all layers. Of particular note for this work is the low interfacial roughness (σ) between the Nb layer and the adjacent Er layer, indicating a lack of intermixing.

4.8.2 Polarised Neutron Reflectometry

Fitting the PNR allows the scattering length density (SLD) to be obtained. This technique is highly complementary to XRR. The addition of a polarising mirror to the beamline separates the up (u) and down (d) neutrons, allowing only one spin state to reflect towards the sample.

Table 4.3: Material parameters extracted from the fit in fig. 4.9. The error in the extracted values is approximately 10%.

Layer	Density (f.u./Å^3)	Thickness (Å)	σ (Å)
LuO	0.030	12	6
Lu	0.033	35	2
Er	0.032	62	5
Nb	0.055	84	3
Al_2O_3	0.065	∞	3

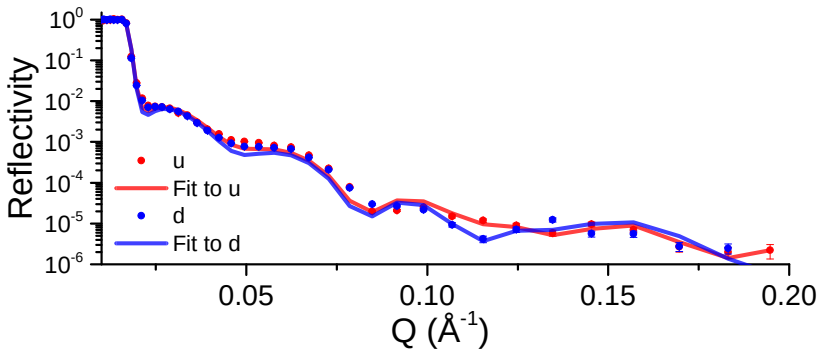

Figure 4.10: Polarised neutron reflectometry curves from the 6nm Er film. The two neutron spin states are shown (u,d) along with the corresponding fit described in the text.

When scattering from a magnetic sample, the total scattering is proportional to the sum of nuclear and magnetic scattering length. Careful fitting to the two obtained reflectivity curves allows the extraction of depth dependent magnetisation.

Figure 4.10 shows the obtained PNR curves for the sample with a corresponding fits to each spin state. The structural properties are imported from the XRR fit and the magnetisation of each layer is a fitting parameter. Despite the in-plane saturation moment of the sample being high (consistent with bulk), there appears to be very little splitting between the two spin states in the PNR data. This is also seen in the spin asymmetry (Figure 4.11 **(a)**), which is the difference between the two spin states normalised to their sum.

To guide the neutrons only a small applied measurement field (10 mT) is needed. Cooling in this small field is not expected to have any impact on the magnetic state of the Er. At this field and temperature value (5 K), Er is expected to be in a highly non-collinear or spiral magnetic phase. Atomic scale antiferromagnetism is too short a lengthscale for neutron reflectivity to probe, and as such is seen as net zero moment. In Er, however, the spiral repeat distance (equivalent to the antiferromagnetic lengthscale) is several atomic layers long; this is still too short for full depth dependence, but allows some insight.

Two fitting techniques are employed on the data. The first technique treats the magnetic moment inside the Er layer as being constant with depth, and will return the average moment inside the Er (model 1). The second technique allows the moment to be a depth dependent free parameter (model 2). In both cases, positive magnetisation corresponds to moments pointing in the direction of applied field. For a saturated, ordered, ferromagnet both fitting techniques would return that the magnetisation of the entire layer is positive.

The spin asymmetry and results of the two fitting techniques are presented in Figure 4.11. The differences between the two models are too subtle to observe in the reflectivity data, and even in the spin asymmetry there are only very small differences at low Q. Notably at higher Q ($> 0.08 Å^{-1}$) the models begin to separate, with model 2 providing a closer fit in this region.

Model 1 (shown in Figure 4.11 **(b)**) returns a constant magnetic moment inside the sample of -0.3 μ_B/atom. This is far lower than the moment possessed by the individual Er atoms (over 9 μ_B/atom). The returned moment is also negative. This solution is therefore most likely a returned 'average' magnetisation due to an inhomogeneous magnetic state within the Er layer.

Model 2 (shown in Figure 4.11 **(c)**) returns a small total moment, but a large, oscillating,

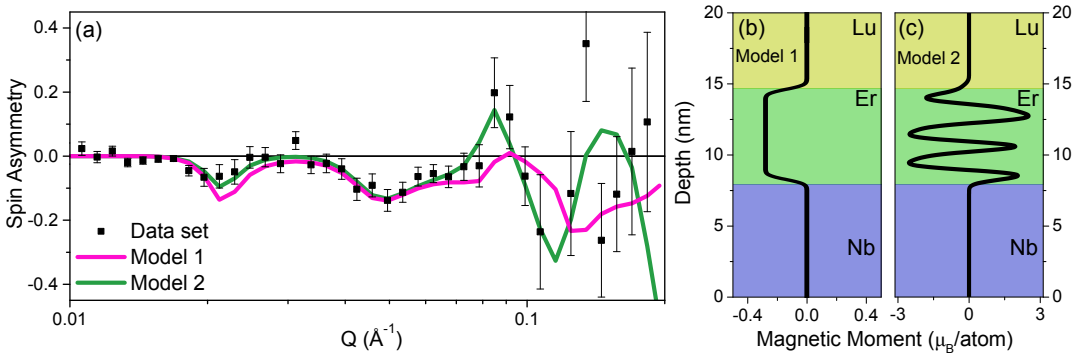

Figure 4.11: (a) Spin asymmetry for the PNR data in Figure 4.10 with two models (see text) for the magnetism in the Er layer shown in **(b)** and **(c)**.

depth dependent internal moment. The oscillation between positive and negative magnetisation values returned from this fitting technique is a good approximation for spiral magnetisation inside the Er layer. The average moment of this model (returned by integration) is -0.26 $\pm$ 0.05 μ_B/atom, consistent with the returned moment for model 1.

This model appears to have given some additional insight into the local magnetic state. It returns a magnetic spiral with repeat distance of $\approx$ 2.5 nm. This corresponds to a magnetic repeat distance of 4.3 atomic layers. Examining the expected bulk phases of Er, this is not consistent with any known commensurate state.

In order to interpret which of the two models provides the most insight into the actual magnetic state of the sample, one needs to consider the magnetometry. This showed the Er layer retained a high moment per atom but with a low net average remanent moment. Both models predict the latter, but only the spiral model predicts the former and is hence a candidate for the non-collinear state of the system. Even if the returned model does not match the exact magnetic state of the sample, the PNR shows evidence that the magnetisation of this sample is highly disordered.

4.9 Conclusions

The primary purpose of this chapter was to demonstrate that sputter deposited thin films of Er exhibit the intrinsic inhomogeneous magnetic properties of the bulk. It has been shown that indeed many of the features of bulk Er are attainable in thin film form, however in decreasing Er thickness the low temperature magnetic phases become suppressed. In par-

ticular the ferromagnetic OOP conical magnetic phase was only observed for the thickest sample which was found to be sufficiently bulk-like that all three magnetic phases were retained. In this film a new magnetic commensurate state, with longer magnetic repeat distance than bulk, was reported for the first time. Due to the excellent epitaxy of the sample, the magnetic properties were highly c-axis influenced.

A significant strain on the thin films was found, which placed the c-axis lattice constants at greater values than reported elsewhere. Taking into account this offset, the temperature dependence of the Er lattice parameters for the 200 nm thick sample qualitatively matched that of previous experiments on bulk and MBE grown thin films including a low temperature structural transition.

By reducing the film thickness to 50 nm, the neutron diffraction showed the suppression of the conical phase as at the lowest temperatures the film only reached the 1/4 state. This suppression of an OOP component of magnetism most likely arised as the contribution of the thin films demagnetising energy began to outweigh that from the magnetocrystalline anisotropy, typical in films of decreasing thickness.

The thinnest, 5 nm thick sample showed both suppression of the conical phase and weakening of the intermediate phase. PNR data provided some evidence that this sample reaches a spiral phase, however this magnetic phase does not match any known commensurate state and must be metastable. The application of a 6 T field revealed the IP magnetisation reached the theoretical maximum, suggesting a complete unwinding of the spiral magnetisation. Upon relaxation of the field, the Er did not retain ferromagnetic remanence, rather re-forming the spiral state or another nearly compensated magnetic structure. In thicker films, the c-axis crystalline anisotropy became greater, resulting in the OOP magnetisation becoming the largest component.

CHAPTER 5

Control of Superconductivity in Nb/Er Bilayers

5.1 Introduction

For a homogeneous F layer, the damped oscillatory behaviour of the superconducting order parameter inside an adjacent F layer (Figure 2.2) results in a non-monotonic superconducting critical temperature (T_c) dependence on the F layer thickness, where an initial sharp drop in T_c is followed by a re-entrant increase and stabilisation of T_c. This predicted dependence of T_c [86, 87] was subsequently observed experimentally in a large number of systems. A review of these measurements is given in Chapter 2. For the case when the F layer is conical, the non-monotonic T_c becomes oscillatory, where the pitch of the oscillation is linked to the repeat length of the cone. This is in part due to preferential LRTC generation by the conical F layer [57, 58]. Such oscillations were observed in previous works for Nb/Ho bilayers [159, 160]. The first aim of this section is to explore if similar oscillations are observed in Nb/Er bilayers.

While an oscillatory T_c with Er thickness would contain a lot of physical information about the system, it would not be particularly useful from a device perspective. By making the Er layer thicker, the metastable magnetic states explored in Chapter 4 become available. The influence of these metastable states on the superconductivity of an adjacent Nb layer is studied in the second part of this chapter. It has been proposed that if switching between the superconducting and normal states can be achieved by an external magnetic field, it can used as a memory device which is analogous to those based on giant magnetoresistance [14].

In this chapter, the work attributed solely to the author was all sample depositions, optimisation and characterisation and electrical transport measurements. Magnetometry was carried out by the author and J. D. S. Witt who also contributed data analysis code.

5.2 Growth of Nb/Er Heterostructures

All samples in this chapter were prepared with DC magnetron sputter deposition in the system described in Chapter 4. To ensure consistency between samples, up to 24 complete samples were deposited in a single vacuum cycle with or without the use of the heater bulbs.

A series of Nb/Er bilayer films were sputter deposited at ambient temperature onto thermally oxidised Si substrates, 10×10 mm. The Nb thickness was fixed at 20 nm (which is just thick enough to be reliably superconducting), while the Er layer thickness was varied in the 0.8 - 12.8 nm range. All films were capped with 5 nm of Lu. In order to ensure sample-

to-sample consistency, and negate any artefact arising from growth order (as T_c generally increases with growth order), the Er thickness was randomised and the Nb was deposited 5 nm at a time on all samples. The Er and Lu were deposited immediately following the final 5 nm Nb layer. Every sixth sample was a Nb film with no Er to ensure any changes in Nb quality with growth order could be tracked.

For polycrystalline Nb the coherence length (ξ_{GL}) was determined using equation 2.14 to be 10.5 ± 0.5 nm. At 20 nm the Nb will be highly sensitive to the S/F interface as it is less than $2\xi_{GL}$ thick, but will still have a measurable T_c in the available ^{4}He cryostat.

5.3 T_c Oscillations with Er Thickness

The transition into the superconducting state was investigated by measuring the resistance of each bilayer as a function of temperature, R(T). The films were diced into approximately 3×3 mm cuttings, mounted into chip-carrier packages where electrical contact was made to the samples by wire bonding. The chip carrier was mounted in a sample holder, allowing application of the field parallel to the plane of the sample. The chip package was in good thermal contact to a cernox temperature sensor. The resistance as a function of temperature of the samples, from which T_c is obtained, was always measured at zero applied field at a constant cooling/warming rate of 0.2 K/minute. Temperature sweeps, both cooling and warming, were recorded to check for temperature hysteresis in the measurements (which was found to be of order 20 mK).

5.3.1 Stepped Transitions

The initial aim to compare the Nb T_c to the thickness (d) of the Er for a constant Nb thickness was complicated by the observation of step features appearing in some of the transitions. Some examples of such curves are shown in Figure 5.1. In most polycrystalline films there is a small feature present at around 5 K. This appears to be related to the T_c of the Nb films without any Er. As will be shown, this feature may still be sensitive to the adjacent Er. In every growth, 4 single layer Nb films were deposited in order to track systematic changes in T_c during the growth. None of these samples showed a stepped transition, whereas approximatively 70% of Nb/Er bilayers showed the step.

Some common explanations for step-like features in the transition curves can be ruled out for this system. The sputtering technique employed in this work is very unlikely to create

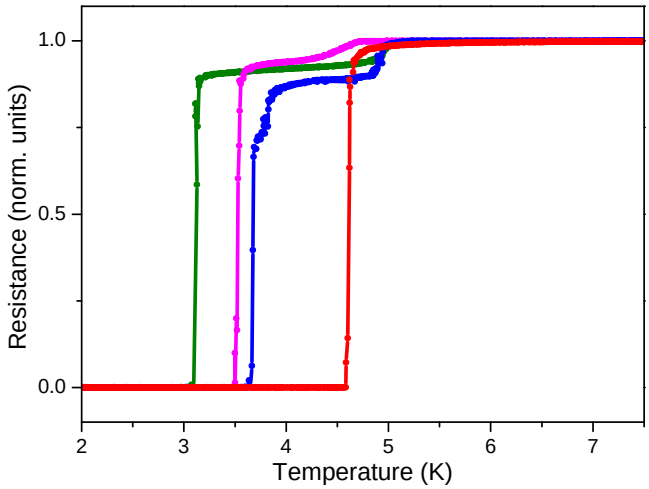

Figure 5.1: Normalised resistance as a function of temperature for four typical polycrystalline samples. The red curve shows behaviour for a single continuous transition of a single Nb layer sample, while the other curves show steps of varying height and width in the transition of Nb/Er bilayers . Interestingly two Nb/Er samples showed initial onset of T_c at higher temperature than the single Nb layer.

a significant thickness gradient. To check the uniformity of the films, a 20×20 mm film was diced into several pieces and XRR was performed. A 5% variation in thickness was observed, this variation is only slightly greater than the error in individually calculated thickness by fitting to Keissig fringes. By comparison, the sample size for transport measurements was only 3×3 mm, where uniformity in film thickness will be very high. Crystallographic inhomogeneity is a further possibility, but again very unlikely. Current induced local heating (or locally exceeding the critical current density) can be ruled out because the step-like features showed no dependency on applied current between 100 nA and 1 mA. For all measurements in this chapter a current of 10 μA was used. In a sheet film, the local current density will be very low. Poor interface transparency can cause anomalous features in resistivity around the superconducting transition, as current paths change to flow preferentially through the superconductor. The formation of an oxide barrier at the interface would cause such effects. Calculation of the oxidation time (as the monolayer formation time, τ_{ML}) is possible through [223]

$$\tau_{ML} = \frac{a}{Z_A}, \tag{5.1}$$

where a is the number of spaces, per unit of surface area, which can accept a specific gas and Z_A is the impingement ratio. The typical value of partial water pressure (the main source of oxygen) in the vacuum is 5×10^{-9} mbar giving $\tau_{ML} \approx 15$ minutes. This is much longer than the (at most) 20 seconds taken for the system to move a sample between sources. It should also be noted that a bad interface would destroy the proximity effects presented in this chapter. In addition, other S/F films (where the F layer was homogeneous) reported in this work, grown in the same vacuum system and measured with the same instrumentation, do not show stepped transitions. Step-like features have been observed previously in work containing helical F layers, for example Witt *et al.* in Nb/Ho bilayers [159, 160]. It is therefore believed that the origin of the step is the proximity effect of the Nb with spiral magnetisation.

Typically in this type of measurement, T_c is defined as the temperature at which the resistance has reached 50% of the normal state (R_N) value. Due to the step-like features this is not as appropriate in this case. To investigate the step-like features further, T_c is extracted at 5, 50 and 98% of R_N.

5.3.2 T_c vs. d

Figure 5.2 shows the variation in T_c as a function of Er layer thickness, d, for the three positions along the transition. In **(a)** and **(b)**, T_c is normalised against the critical temperature of the Nb on-its-own samples. At 5 and 50% of R_N there is an overall oscillatory trend with minima at 5.0 ± 0.8 and 12.0 ± 0.8 nm. On initial inspection this would appear comparable to the type of oscillation observed in conventional S/F bilayers. In these systems, the calculations of Buzdin *et al.* showed the thickness at which the initial minima occurs at is related to ξ_f and although the theoretical calculations show further minima are possible, in most instances they are not observed [41]. This is due to the now exponentially small component of superconductivity which remains at multiple values of ξ_f in the ferromagnetic layer.

When the data are plotted in growth order (not shown) there is no trend in T_c as a function of growth order for the samples with Er. For the single layer Nb films, a monotonic increase in T_c with growth order is observed. This is linked to the improving vacuum conditions as a function of time. The growth of reference Nb films allows for this small increase to be corrected, with the corrected data shown in Figure 5.2 **(a)** and **b**. The small spread in Nb T_c (≈ 0.3 K) is shown in **(c)** and is much smaller than the suppression measured at 5 and 50% of R_N attributed to the Er proximity effect (up to 2.5 K).

The 98% R_N behaviour is somewhat different. At this position in the stepped trans-

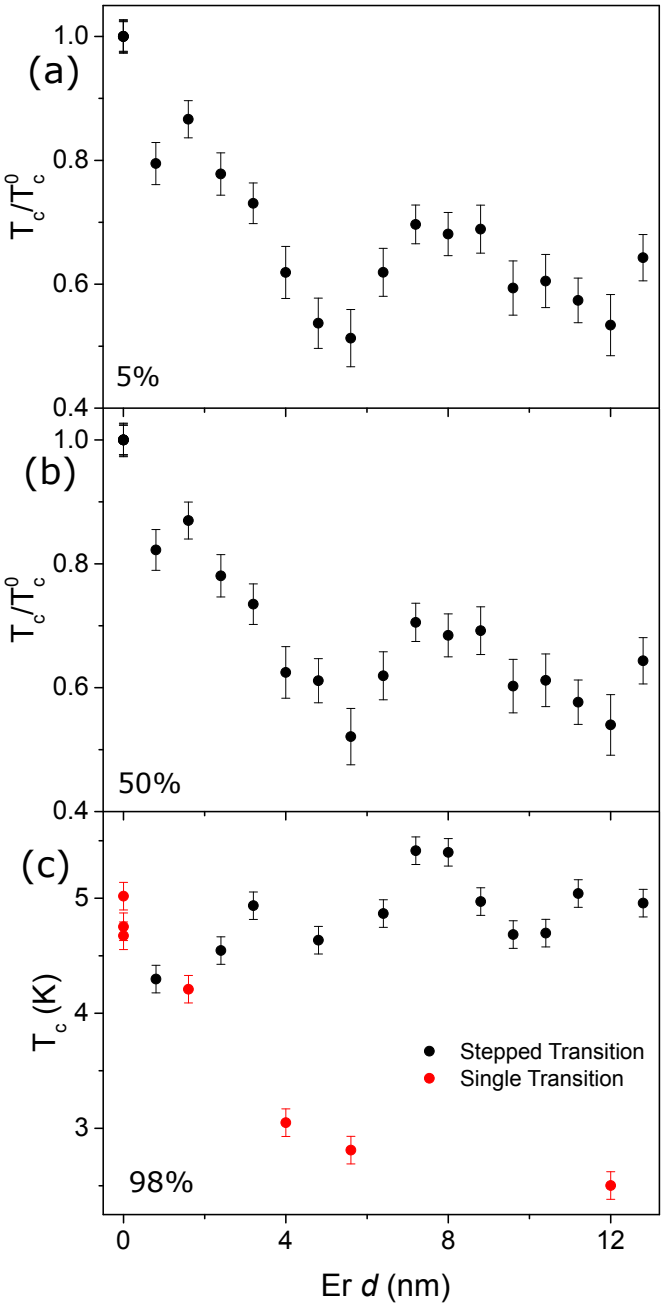

Figure 5.2: Oscillations of T_c of Nb/Er bilayers with the thickness, d, of Er at three positions along the transition curve. **(a)** At 5% R_N (the normal state resistance), **(b)** At 50% R_N and **(c)** At 98% R_N. In **(c)** the samples have been separated by colour to indicate if they showed a single or stepped transition (see text for details). Error bars are estimated from the spread in T_c of 4 single layer Nb films grown in the same vacuum cycle. The error in d is estimated to be 0.4 nm.

itions it is the initial onset of superconductivity at around 5 K which is probed. For clarity samples without a stepped transition are plotted in red. In samples which show no stepped transition, an approximately exponential decay with d is observed. Where there is a stepped transition, this 98% initial onset shows an oscillation which qualitatively similar minima and maxima positions as the 5 and 50% data. This is interesting, in that the two components (decay and oscillation) of the 5 and 50% data appear to have been separated out in this onset T_c. The spread of the oscillations ($\approx$ 1.3 K) is much larger than the spread in T_c of the single layer Nb films. Additionally it is noted with interest that for two consecutive Er thickness, the observed onset T_c is actually *higher* than that of any of the single layer Nb films. Due to the random growth order, these two samples were not grown one after another, rather they were the second (8 nm Er) and twentieth (7.2 nm Er) samples deposited.

5.3.3 Discussion

An attempt to fit the oscillations in T_c observed for the polycrystalline samples within the framework of the traditional S/F theory is now made. For the simplified case of a transparent interface, Buzdin showed [41] the critical temperature of an S/F bilayer can be described by

$$\frac{T_c - T_c^0}{T_c} = \frac{\pi}{4T_c\tau_0}\left(\frac{\sinh(2y)+\sin(2y)}{\cosh(2y)-\cos(2y)}\right), \tag{5.2}$$

where $\tau_0^{-1} = (D_s/2d_s\xi_f)\sigma_f/\sigma_s$ and $2y = 2d_f/\xi_f$ is the dimensionless F layer thickness. The respective conductivities of Nb, $\sigma_s = 7.66\times10^6$ S/m, and Er $\sigma_f = 1.16\times10^6$ S/m. The effective coherence length inside the F layer was calculated with

$$\xi_f = \sqrt{\frac{\hbar D_f}{E_{ex}}}, \tag{5.3}$$

where the exchange energy (E_{ex}) is given by $k_B T_{\text{Curie}}$. The T_{Curie} is assumed to be the low temperature transition to the conical ferromagnetic state and set to 20 K. This gives an effective $\xi_f \approx 12$ nm for Er. The fit to the data was made worse using the high temperature transition from the CAM antiferromagnetic to intermediate phase.

A further theory developed by Wu *et al.* considered the case where the F layer was a conical ferromagnet [57, 58]. For Er, this may be the more appropriate model to use. This model has not been explicitly solved for the case of Nb and Er. The model shows that T_c oscillations are linked to the repeat length of the spiral. This in turn plays a competing role with the FFLO state. For a ferromagnet such as Er with a small E_{ex} (due to the low

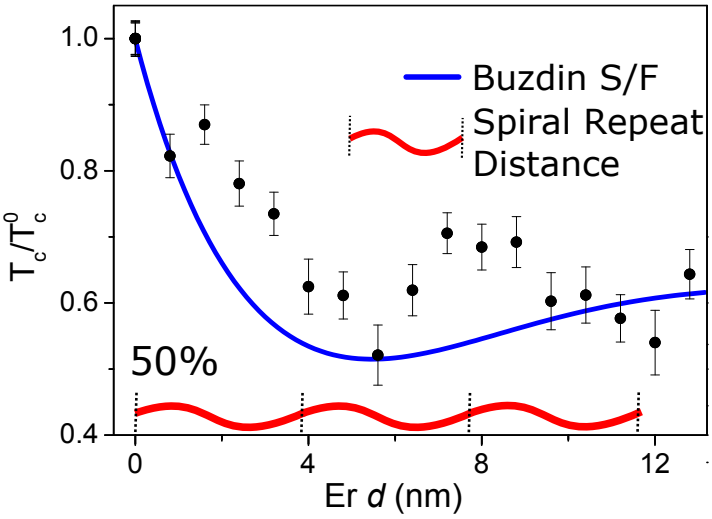

Figure 5.3: The T_c 50% dependence of the Nb/Er bilayers as a function of the Er layer thickness, d. Also plotted is the result of the simplified S/F model (equation 5.2) and the spiral repeat distance to indicate if the oscillation was due to the spiral magnetisation as predicted in reference [58].

Curie temperature) the maximum in the T_c oscillation is expected when the thickness d_f is a multiple of the spiral repeat distance (τ_c).

Figure 5.3 shows the result of the Buzdin S/F model and a schematic representation of the spiral repeat distance (for the 2/7 commensurate state) with the experimental data at 50% of the transition. The 2/7 commensurate state is chosen as it is the first commensurate state of the intermediate phase, however the repeat distance by PNR on the 5 nm Er film in Section 4.8 provides some evidence that the true repeat distance may be shorter.

Considering the data in comparison to the Buzdin S/F model, it is possible using the aforementioned physical parameters to place the minimum in T_c at the same point as the data. The model, however, does not reproduce the immediate increase to a peak in T_c or predict that there should be a second oscillation in the this range of Er thickness.

The maxima and minima in the data do not match the repeat distance of the spiral, with the first minimum at 5.0±0.8 nm and the second at 12.0±0.8 nm, the oscillations are approximately twice the spiral repeat length. This discrepancy could be explained in analogy to the "aliasing" effect in RKKY coupled magnetic multilayers, where the thickness increments do not allow the probing of the true magnetic spiral distance, causing the appearance of a longer ranged oscillation [224–228]. To test for this, the thickness increments would need to

be significantly reduced.

For a S/AF (antiferromagnet) proximity effect, no oscillations in T_c are expected at all [72]. Due to the extremely short repeat length of antiferromagnetism, the Cooper pair does not sample the magnetisation and so does not form the FFLO state. This case is more similar to the S/N proximity effect, where increase the thickness of the AF cause the critical temperature to decrease monotonically due to the proximity effect.

5.3.4 Epitaxial Samples

Using the previously determined best growth parameters, the Nb was deposited at a nominal temperature of 700°C, after which the system was cooled to 500°C, a final thin Nb interface layer was deposited at this temperature, followed directly by the Er and then a 5 nm-thick Lu capping layer.

An attempt to reproduce this data set was undertaken for epitaxial samples. Under these growth conditions, resulting single layer Nb films showed a large sample-to-sample variation. This was most likely due to a combination of changing vacuum conditions during the growth and inconsistent heating provided by individual bulbs. The heating bulbs for practical reasons are of varying age, which could impact the maximum temperature (and hence epitaxy of the films) achieved. Evidence of this sample-to-sample variation in epitaxial films was also observed in Chapter 4, for example in the films which showed unexpected superconductivity and the mixed phase growth of the 50 nm sample. In the current deposition chamber set-up it was not possible to overcome this.

Despite this limitation, Figure 5.4 shows that, within the obtained data, it is possible that oscillations may still exist, with minima at 4, 8 and 12 nm. In order to further investigate this a much higher density of points around the minima would be necessary. Some general conclusions, however, can still be drawn from the epitaxial sample set. If these oscillations are physical, then the theories discussed previously in an attempt to fit the polycrystalline data would also fail to reproduce the oscillation seen here. The apparent change in periodicity of the oscillations between polycrystalline and epitaxial data sets may be explained from the increased strain which will be present in the epitaxial films.

These films of much improved crystalline quality still showed step-like features in a number of samples, strengthening the argument that these features are as a result of the proximity of Nb to a spiral ferromagnet.

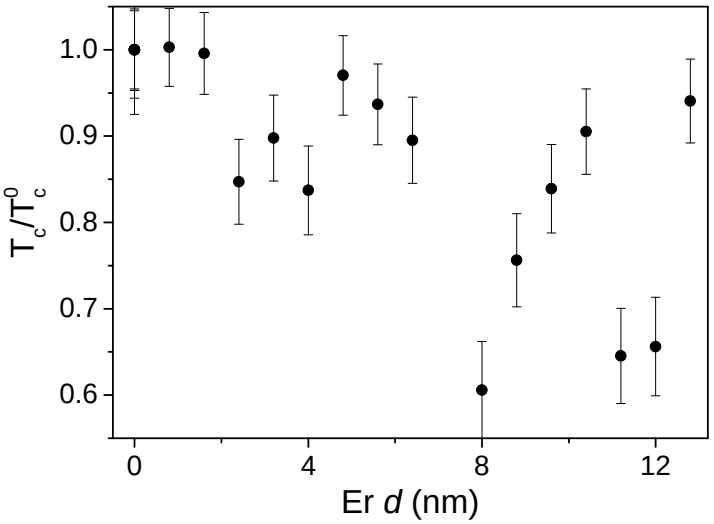

Figure 5.4: Oscillations in T_c for Nb/Er bilayers with the thickness, d, of Er at 50% of the normal state resistance. Error bars are estimated from the spread in T_c of 4 single layer Nb films grown in the same vacuum cycle. The error in d is estimated to be 0.4 nm.

5.4 Control of T_c in a Single Bilayer

Increasing Er thickness in turn increases the availability of the metastable magnetic states within the Er phase diagram. The aim of this investigation is to see if controlling these metastable states can influence the superconductivity of an adjacent Nb layer. The motivation for this is the recent results on the superconducting spin valve (SSV). In a SSV, control of the magnetic state of the two F-layers in an S/F/F or F/S/F heterostructure can tune the generation of the LRTC [19–22]. The generation of the LRTC (opening an additional "leakage" channel for Cooper pairs) is believed to result in the lowering of the T_c of the system. Typically, the suppression of T_c is of the order 10–20 mK, although by introducing a half-metal as the bottom F-layer, this effect can be significantly increased [141].

Such manipulation of the F-layers requires careful engineering of the heterostructure and the rotation of the sample in an applied magnetic field. The pitfalls of this measurement are discussed in detail in Section 2.7.2. The motivation for this work is therefore to create a simplified S/F hybrid system, where the superconductivity can be controlled by a single adjacent F-layer. A limitation was placed on the system to only require the ability to apply an external field in one direction (without the need for sample rotation).

The same cryostat employed previously is now used with the superconducting magnets

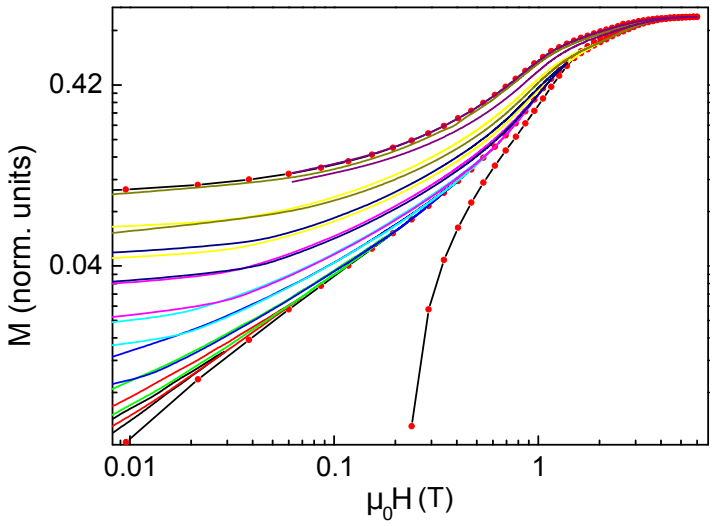

Figure 5.5: Positive quadrant of the magnetic hysteresis loop (circles) and minor loops (solid lines) of the bilayer at 10 K with field applied in-plane. The data are displayed on a log-log plot for increased clarity.

on. The resistance as a function of temperature of the samples, from which T_c is obtained, was always measured at zero applied field. The initial field, to set the remanent magnetic state, was applied in-plane, above the superconducting T_c, immediately prior to measurement.

5.4.1 Magnetic Characterisation

The magnetisation versus field data, along with minor loops, for the 25 nm-thick Er bilayer sample at 10 K are shown in fig. 5.5. The red circles show the initial magnetisation and full magnetic hysteresis behaviour for applied magnetic fields up to 6 T. The solid lines are a series of minor loops, from which information about the remanent magnetisation (M_r) of the sample can be obtained. The M_r as a function of initial field data are collated in the lower panel of Figure 5.6.

It is evident from Figures 5.5 and 5.6 that at low fields, there is little change to the remanent state of the Er. This indicates that, in this range, the stabilisation of the spiral magnetic structure in the Er is robust against perturbation by the externally applied magnetic fields. The large increase in M_r between 2–3 T is evidence that, for initial field values greater than this, the Er does not re-enter the same spiral phase upon relaxation of the field. This is con-

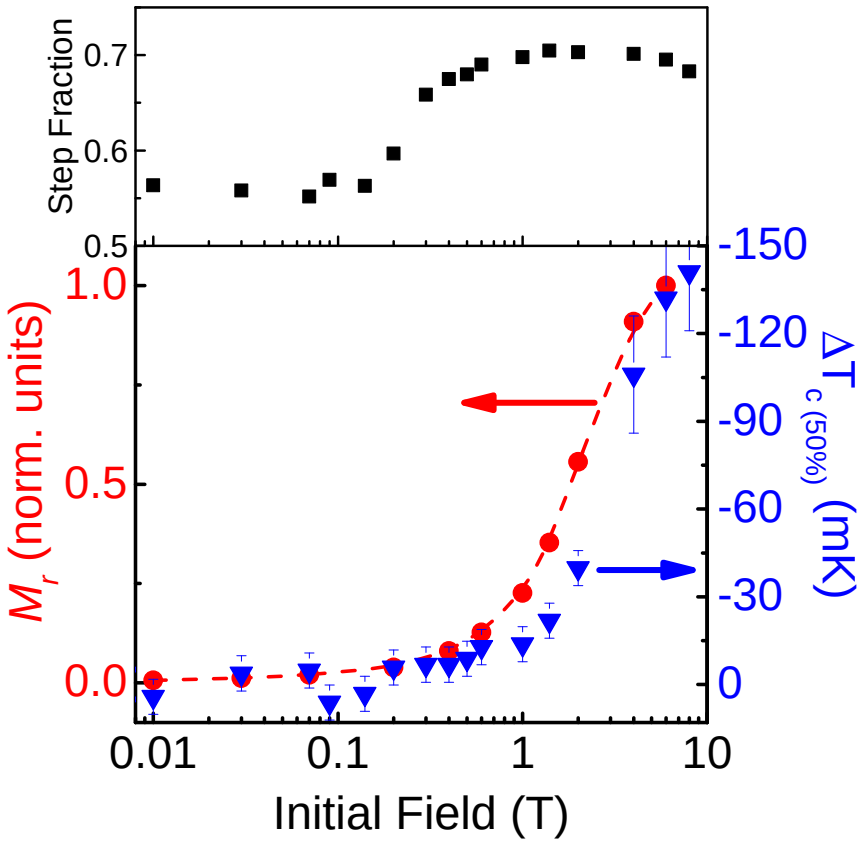

Figure 5.6: Top panel: The fractional step height change with initial field. Bottom panel: The normalised remanent magnetisation, M_r, (circles) and the shift in superconducting critical temperature from the as cooled state, ΔT_c, (triangles) as a function of initial applied magnetic field.

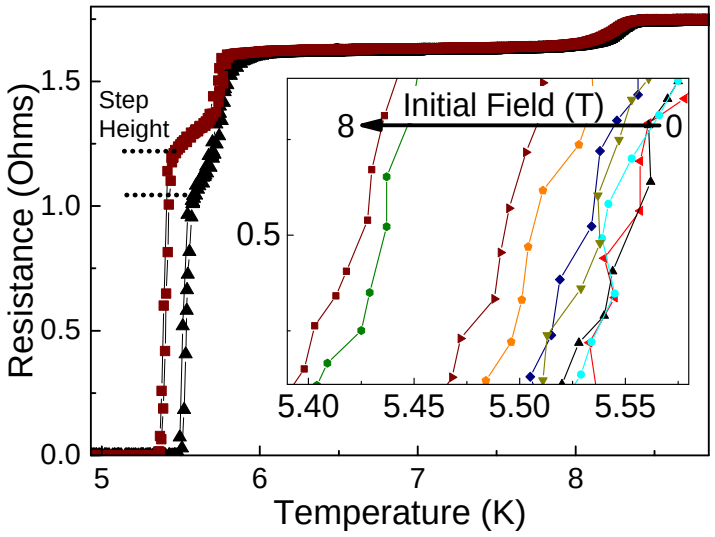

Figure 5.7: Resistance as a function of temperature for the as-cooled magnetic state (triangles) and post 8 T field saturation (squares). Both warming and cooling data are included and the changing step heights marked. Inset: The evolution of T_c as a function of initial field.

sistent with previous characterisation work which shows that at approximately 2.5 T there is a phase transition, for an in-plane applied field, into a distorted spiral phase, known as 'fan' or 'canted-fan' [217, 229].

5.4.2 Electrical Transport

In Figure 5.7 the resistance as a function of temperature for the 25 nm-thick Er bilayer sample can be seen. The data show the onset of superconductivity as the temperature is decreased for the as-grown case (triangles) and after the application of an 8 T applied magnetic field (squares). In the inset of Figure 5.7 the evolution of the T_c as a function of the initial applied magnetic field can be seen. Resistance as a function of temperature was always measured in zero applied magnetic field and T_c was defined as 50% of the normal state resistance. ΔT_c is calculated as the difference between T_c of the the as-grown state and T_c after the application and removal of a magnetic field. The ΔT_c data for all of the initial applied magnetic field values are collated in Figure 5.6.

It is immediately clear that there is a strong link between the M_r of the Er and the T_c of the superconductor. This correlation, between the properties of Er and Nb, show that both the T_c of the Nb and the magnetic state of the Er are strongly dependent upon the

field history of the sample. It also shows that there is a strong coupling between the S and F layers. The largest change to ΔT_c comes between 2–3 T, which, as mentioned previously, is also the field value where the Er state is expected to change magnetic phase. After the application of the largest field possible in our system, 8 T, the T_c of the Nb was suppressed by approximately 140 mK, which is the largest value reported for such a system. Once the metastable magnetic state is altered, the T_c of the Nb does not change further, until the sample is warmed through the curie temperature, which effectively 'resets' the system.

It was observed, in the upper panel of Figure 5.6, that the height of the step as a fraction of the transition is field history dependent. Interestingly, this step height change occurs at a different field than the largest changes in M_r and ΔT_c. The step height changes just as the gradient of M_r begins to increase, this will be just at the transition between metastable phases. While the change in step height does not appear to be intrinsically linked to the change in T_c, it is still clearly linked to the magnetic state of the Er layer through the proximity effect. This further supports that the stepped transitions in these samples do not have a trivial cause.

5.5 Discussion

As a conical ferromagnet, Er is an ideal system in which to generate the LRTC [59]. In this chapter, however, it is not possible to directly attribute LRTC generation to the observed lowering of T_c. In the superconducting spin valve, it is the rotation from an aligned homogeneous magnetic orientation to the misaligned inhomogeneous magnetic state which creates the LRTC proximity effect. The generation of the LRTC allows more effective leakage of supercurrent from the S layer, and results in a lowering of T_c. In this experiment the disordered, as cooled, conical magnetic state has the higher T_c. The application of a field is most likely to align the surface moments and create a 'fan' structure. This is also an inhomogeneous magnetic state, which *may* produce a larger triplet component (resulting in a observed lowering of T_c), although further theoretical modelling outside the scope of this work is needed to support this.

The size of this T_c effect is generally larger than that reported for spin-valves (and is not the only reported case of the disordered magnetic state resulting in a higher measured T_c [143, 171, 172, 230]). It is therefore necessary to use caution for the interpretation of T_c measurements alone as evidence for the presence of the LRTC in a S/F system.

In the transition curves, shown in fig. 5.7, three step-like features can be seen. The origin

of these steps is most likely similar to the previously discussed steps. For the epitaxial Nb, it is not unreasonable for the T_c of a bare film to be in the region of ≈ 8 K, where the first step occurs. This is evidence of local regions of the bilayer film where the Er has no direct influence on the Nb, that is, where the two materials are not coupled by the proximity effect. One possibility for this is at the Er grain boundaries or local regions around the wire-bond contacts, where the force of the contact may have disrupted the Nb/Er interface. This interpretation is supported by the observation that there is no field history dependence of this step. Again local current induced heating, crystallographic inhomogeneity and thickness gradients are ruled out for this sample.

5.6 Conclusions

The T_c oscillations as a function of Er thickness showed a highly complex oscillation for both polycrystalline and epitaxial data sets. It was not possible to reproduce this oscillation in the framework of the simplified S/F theory. Additionally the periodicity appeared to be longer ranged than the spiral repeat distance for any expected commensurate state for thin film Er. This ruled out attributing the oscillation solely to the spiral magnetisation.

The step like features present in many of the Nb/Er samples are of interest due to the origin of the step believed to be caused by the proximity effect with spiral magnetisation. Such steps are not observed in S/F samples where the F layer was homogeneous. They are possible evidence for a spatial variation in the influence of the proximity effect. It has been observed previously that by removing the spiral magnet, T_c recovers to that expected for a bare film and additionally step like features disappear [230].

It was observed that the ferromagnetic remanent state of Er, when proximity coupled to a superconductor, can have a strong influence on the T_c of the superconductor. The application of magnetic field is able to change the metastable magnetic state of the Er. This modification results in a fundamental change to the shape and temperature of the superconducting transition. The shift in T_c of 140 mK was much larger than previously observed in spin valves or for singlet domain wall effects. It is hoped that the observation of this unconventional effect proves fruitful for refinement of S/F theory, and offers a new route for device application for low temperature super-spintronics.

CHAPTER 6

Induced Moment in a Normal Metal Coupled to a Superconducting Spin Valve

6.1 Introduction

In lab based transport results, evidence for the presence of the LRTC in superconducting spin valves is extracted from the angular dependance of T_c with LRTC generation. This result was summarised in Section 2.7.2. While this behavour matches the theoretical expectation of LRTC generation in the spin valve, it gives little direct information about the nature or extent of the LRTC in the heterostructure. In an attempt to address these questions, the local magnetic state of the same heterostructures as those in reference [22] are studied in this chapter. Two large scale facility based magnetism probes (neutrons and muons) are used to search for an expected induced moment originating from the triplet Cooper pair.

In this chapter, the work attributed to the author were sample depositions (which were performed jointly with J. Kim), sample optimisation and development, magnetometry, X-ray characterisation and fitting, fitting to neutron measurements. Neutron measurements were performed at the ISIS neutron and muon source, with the assistance of G. Burnell and local contacts C. J. Kinane and J. F. K Cooper. Muon spin rotation measurements were performed at PSI, with the assistance of S. L. Lee and M. G. Flokstra (who also contributed the fitting code) and local contact T. Prokscha. Additionally S. L. Lee and M. G. Flokstra gave significant advice on the how to present LEμSR data and contributed graphs and graphics where acknowledged.

6.2 Sample Design

As established in Chapter 2, the key ingredient for the generation of the LRTC is magnetic inhomogeneity. This chapter considers the prototypical super-spintronic device, the superconducting spin valve. In this system, the degree of magnetic inhomogeneity can be tuned by controlling the angle of separation of the two ferromagnets. There are two possible geometries for this system, the 'superconductor on top' SFF and the 'superconductor in the middle' FSF [22], both of which show the expected modulation in T_c with LRTC generation. The former case is employed in this chapter.

In order to be able to control this angle, careful sample design is necessary. In general the SFF spin valve takes the form:

sub/Ta(buffer)/Co(seed)/IrMn(pinning)/Co(pinned)/Nb(spacer)/Co(free)/Nb(S)/Cap,

sub/Ta(75Å)/Co(30Å)/IrMn(50Å)/Co(12Å)/Nb(30Å)/Co(24Å)/Nb(500Å)/Au(700Å),

where the choice of substrate is experiment specific. For electrical transport, thermally oxidised SiO_x is used to prevent current paths inside the substrate. For facilities experiments, lightly doped Si is chosen so that any necessary accelerating voltages can be applied across the samples. The role of the Ta buffer is to grow in a bcc phase to improve growth quality, the adjacent Co seed layer sets the the direction of pinning and the antiferromagnetism in the IrMn, which in turn pins the next Co layer. The free Co layer is separated from the pinned Co layer by a thin Nb spacer layer, which is non-superconducting in this thickness range and acts to decouple the switching of the Co layers. The superconducting layer is deposited on top of the free Co layer. The structure has a capping layer (typically Au) which acts to both protect from oxidation and, when needed, as a moderating layer for muon implantation experiments.

Samples were prepared by DC magnetron sputtering as described in Chapter 3, in a system with base pressure 10^{-8} mbar, at ambient temperature with all layers deposited immediately proceeding each other in a single vacuum cycle.

When considering the aim of this chapter was to observe the small induced magnetism from the triplet components, it is necessary to be careful with the choice of superconductor. Nb is chosen due to its relative ease to sputter and favourable T_c, however it is highly sensitive to vacuum quality and thickness. As discussed previously for transport type experiments, the key consideration is trade off between thickness and coherence length, so that the superconductors properties are dominated by the interface. For the facilities work in this chapter the key trade off is between thickness (to provide a good T_c) and penetration depth. For thin film Nb $\lambda_{GL} \approx 90$ nm [34]. If the film thickness begins to approach λ_{GL} then any induced moment may be mistaken for a Meissner response from the superconductor. The typical base temperature of a ^{4}He cryostat employed by neutron and muon facilities is 3 K. To see any effects, it is favourable to be measuring at a least $T_c/2$. A thickness of 50 nm was chosen as films have a typical T_c of 7.5 K (vacuum condition dependant, but generally reproducible) but are still only half of λ_{GL}, removing the possibility of significant screening currents forming in the direction of sample thickness. Surface screening currents are observed where a technique has sensitivity to out-of-plane fields. On these heterostructes out-of-plane stray fields and surface screening were studied using the scanning Hall probe technique in reference [178], which is summarised in Chapter 2 and in the supplementary

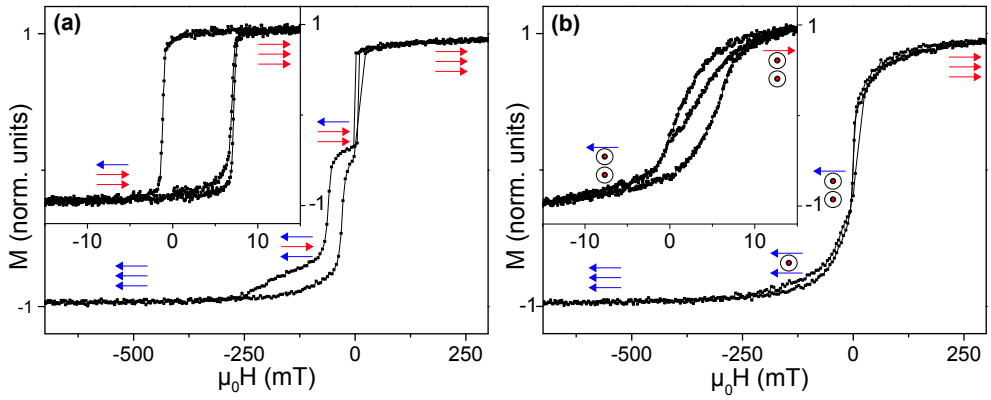

Figure 6.1: Magnetic switching of the three magnetic layers in the spin valve structure for **(a)** field parallel to the easy axis and **(b)** perpendicular. The insets show the minor loop switching of the top 'free' layer only. Blue and red arrows indicate the direction of each layer at the corresponding field.

information of references [22, 231].

6.2.1 Magnetic Characterisation

The chosen exchange biased spin valve structure produces highly reproducible magnetic configurations. The addition of the bottom Co seed layer underneath the IrMn creates room temperature exchange bias, and negates the necessity for complicated field cooling or post growth annealing. The former being impractical from an experimental perspective at the facilities used in this work and the latter unwanted due to possible intermixing which can occur during annealing. The direction of exchange bias is along the growth field.

Figure 6.1 shows magnetic hysteresis loops for the spin valve. In **(a)** the field direction is aligned parallel to the growth field. In this orientation it is easy to obtain magnetic configuration where the 'pinned' and 'free' layers are parallel or antiparallel. The inset shows the minor loop for the 'free' layer switching only. There is a small field offset from zero in all these measurements, due to trapped flux in the VSM magnet. The 'free' layer switches with a coercive field of about 5 mT. From an experimental perspective, it was discovered that not all facilities have magnets which are calibrated in these low field ranges. It is somewhat lucky, therefore, that a field of up to 45 mT can be applied before any of the other magnetic layers begin to switch. Once the free layer saturates, it is the Co seed layer which switches next, followed finally by the pinned layer. When saturating the layers antiparallel to the direction of exchange bias, a field of 300 mT is required, compared to only 5 mT in the direction of

exchange bias.

Figure 6.1 **(b)** shows the same spin valve, after an in-plane rotation of 90°, with the field applied perpendicular to the growth field. For the small applied fields shown in the inset, the pinned layer will only move by some very small angle, while the free layer will align with the field along its hard axis. It is interesting to note that the loop is less square, due to this being the layer's hard axis. The free layer will be aligned to the external field at about 10 mT. The spin valve is now set up in the perpendicular state where the separation between the F layers is 90°. Unlike for the parallel applied field, the exchange biasing in this direction makes the switching of subsequent layers harder, rather than offset. For subsequently higher applied fields, the remaining two layers will be rotated away from the growth direction into the applied field. For either positive or negative fields the two layers saturate at 300 mT. Upon removal of the field the ferromagnetic layers will relax back into the easy (growth) field direction.

6.3 PNR and XRR Fitting of Device Structure

In order to interpret results from muon and neutron facility techniques it is first important to build a physical model of the spin valve system. This is achieved by fitting the PNR and XRR curves. Allowing the GenX software free parameters of XRR scans of the complete spin valve structure leads to model with 23 free parameters (each material is fitted with a density and individual layers given a thickness and roughness, except the substrate which is assumed to be infinity thick). While very attractive looking fits can be achieved by allowing GenX free reign over the parameter space, such a fit is probably not a physical representation of the sample's real parameters. The problem gets worse with PNR where magnetism in each layer also becomes a fitting parameter as discussed in Section 3.7. In this section all PNR was performed at the CRISP beamline at ISIS.

The limitations of the model come from the specifics of the PNR and XRR techniques. With this in mind small changes are made to the model between the two data sets. The XRR technique is more sensitive to interfacial roughness (due to the much higher Q range), while in PNR the structure is simplified to having sharp interfaces and only surface roughness. With the PNR technique it is difficult to extract information about the IrMn layer as the SLD for Mn in neutrons in negative, cancelling out with the positive SLD of Ir, making the net SLD for the alloy close to zero. This can be seen in the returned density value in Table 6.1. While this would have been a real problem if the alloy was placed next to air, the surrounding

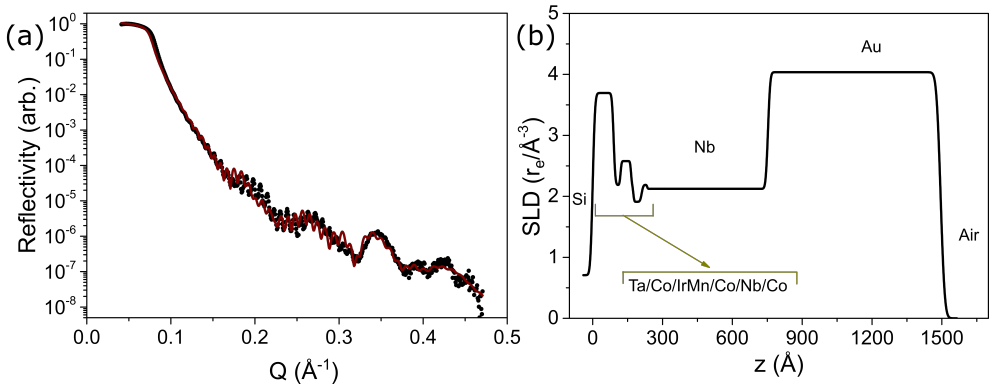

Figure 6.2: (a) Low angle X-ray reflectometry and corresponding fit. The returned fit parameters are given in Table 6.1. **(b)** The returned scattering length density (SLD) with depth through the heterostructure. For clarity each layer is identified.

Co layers provide enough difference in contrast for the layers parameters to be extracted. It should also be noted that, as an atomic antiferromagnet, IrMn has close to no net moment and does not contribute to the total magnetisation of the sample as observed in PNR.

Figures 6.2 and 6.3 show the fitted reflectivity curves for the typical spin valve used in this chapter. The model itself, while physical, does not perfectly reproduce all features of the reflectivity curves. The largest deviation from the data is at high Q values in the perpendicular magnetic state (Figure 6.3 **(e) (f)**, although from studying the spin asymmetry the model clearly reproduces the general trend in the data, even if the magnitude is slightly different. In addition there is a very small deviation at the critical edge in the XRR fit. This could be caused by the prerequisite of the model to take as many previously known densities as possible, or it could be due to misalignment of the sample in the X-ray diffractometer. No such deviation is observed in the neutron fits and so the model is not corrected for this. Methods to improve this type of modelling involve inserting additional layers to account for interfacial effects such as intermixing and magnetic dead layers. Additionally it is not uncommon to add oxide layers at the surface (and occasionally on the substrate) of the structure. As the top Au layer is generally robust to oxidation, and in an effort to avoid adding any more complexity, these routes were avoided.

Table 6.1 shows the structural parameters that went into the model. The nominal 'as grown' structure is identical to that in Section 6.2. As can be seen there is a good agreement with the expected as-grown structure. The error in these extracted values is difficult to ro-

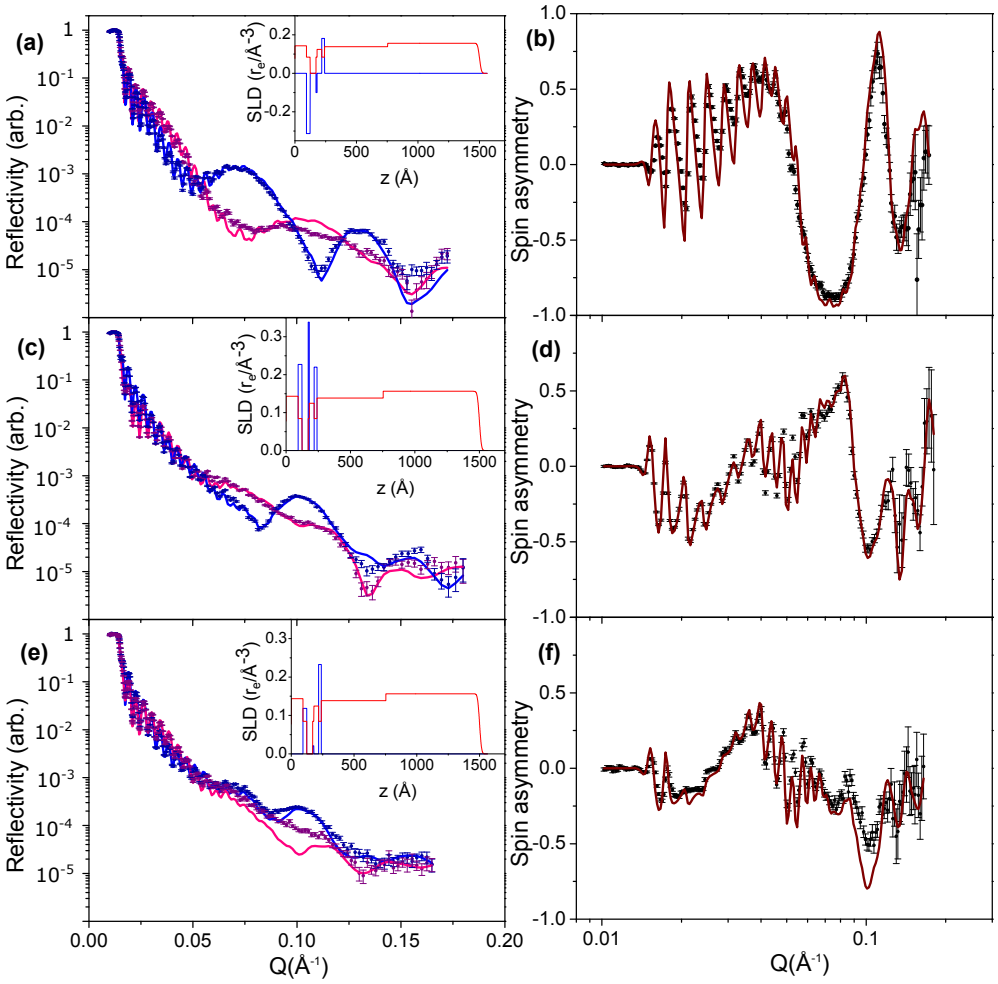

Figure 6.3: **(a),(c),(e)** Polarised neutron reflectometry of the spin valve. The two neutron spin states are shown (u - blue, d - red) along with the corresponding fit. The insets show the SLD profiles where the red corresponds to structural information and the blue magnetic. **(b),(d),(f)** The spin asymmetry (see text) extracted from the PNR curves with corresponding fit. With applied field **(a),(b)** antiparallel, **(c),(d)** parallel and **(e),(f)** perpendicular to the pinning direction.

Layer	Density (f.u./Å^3)	Thickness (Å)	Roughness (Å)
Au	0.0543	747	14
Nb	0.0520	514	8
Co	0.0899	22.5	2
Nb	0.0520	37.5	5
Co	0.0899	9.12	3
IrMn	0.001*	47.2	3
Co	0.0899	30.2	4
Ta	0.0550	93.7	6
Si (sub)	0.0497	∞	8

Table 6.1: Material parameters for the PNR and XRR model of the data shown in Figures 6.2 and 6.3. The error in the extracted values is difficult to robustly quantify and is discussed further in the text. *The total SLD for this alloy is close to zero due to the positive Ir cancelling with the negative Mn, so a density cannot be found.

bustly quantify. For each individual data set one can determine a parameters impact on the returned figure of merit. This would indicate that the values have error of order 10%. This does not, however, take into account the impact changing a layer would have on the other six data sets which are being fitted by an identical structural model. The values in Table 6.1 should therefore be treated as one possible physical model which can be used to fit all seven datasets, rather than returned absolute values from a fit.

6.4 Evidence for Magnetic Induction in the S/F Heterostructure

6.4.1 Expected Results

The traditional inverse proximity effect at the S/F interface is predicted to show an increase in moment inside the F layer and an induced moment in the S layer of opposite sign to the F layers exchange field [74]. Covered in more detail in Chapter 2, the naive description of this effect is that the F layer allows one spin state of the Cooper pair to enter, while the other is stuck on the S side of the interface. This would result in an induced moment largest at the S/F interface, decaying exponentially away with the coherence length. The profile of Bergeret type induced moment from the inverse proximity effect is shown in Figure 2.4.

A small number of reports attribute observations to this effect, however in almost all

cases the technique employed did not have adequate statistics or the required spatial sensitivity to characterise the effect in detail [77–80]. A further report by M. G. Flokstra *et al.* utilising the LEM technique, which possesses the required spatial resolution, found the expected induced moment in the S layer, but with a length scale of only 1 -2 nm. This is far shorter than the coherence length inside the Nb S layer (about 10 nm) [33]. This report either suggests that the key length scale of the induced moment is an order of magnitude shorter than expected, and actually closer to the effective coherence length of a Cooper pair inside the ferromagnet, or that a rather different interfacial mechanism is at play in that work, and possibly others.

The spin valve structures employed in this work have two key features which are different from those reported in reference [33]. Firstly, the ability to tune the angle between ferromagnets with the application of a small field. This allows the study of proximity effects with controlled generation of LTRC. It has been shown using careful electrical transport measurements (see Chapter 2 and reference [22]) that the structures used in this work are capable of producing the LRTC. Secondly, the presence of a thick capping layer placed directly on top of the superconductor. In previous work a ferromagnet was placed between the cap and superconductor to move the S/F interface higher in the structure. While initially this appeared a trivial choice, it turned out to be a key experimental consideration.

A very recent report claims the observation with the LEM technique of an 'inverse Meissner screening' effect created by the LRTC [34]. This observation however is tiny, with the poor statistical fidelity and incomplete data sets making it impossible to attribute the observed effect to the onset of superconductivity, as opposed to changes in the ferromagnets magnetisation (for example). If confirmed, this observation is not contradictory to the type of ferromagnetic induced moment which is the aim of this chapter, as it has a different fundamental origin, being created by screening currents.

6.4.2 Using LEμSR Technique

To study the flux profile B<y> as a function of depth, y, in the superconducting spin-valves first the LEμSR technique is employed. The technique, outlined in Section 3.8, uses muons as a local magnetic probe.

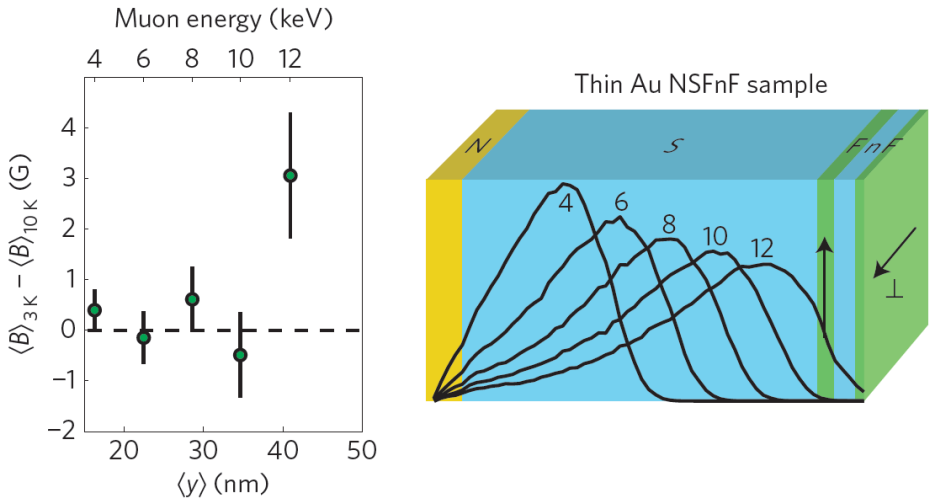

Figure 6.4: The change in local field upon cooling through the superconductors T_c as a function of implantation depth into the heterostructure. Schematic to show the stopping profiles from Monte Carlo simulation inside the heterostructure. Reproduced from [231].

5 nm Gold Cap

The first sample presented has a very thin Au cap, the only job of which is to protect the Nb layer from oxidation. When the Nb is in the superconducting state, it is expected the Au will be fully proximitised by its neighbour, as its thickness is much less than the effective ξ. At this thickness there is very little moderation of the incoming muons, reducing the available energy range. The consequence of this is that the Nb layer can be studied with negligible contribution from the Au layer.

This very thin Au thickness allows detailed probing inside the superconductor and specifically at the S/F interface. This sample geometry is the best chance to observe induced magnetisation of the inverse proximity type at the S/F interface. Figure 6.4 shows the result of this study. No significant difference in the field profile with temperature is observed for muons which probe the superconducting layer. For the highest energy muons, the stopping profile extends into the bottom F_1/F_2 spin valve structure. At this energy a small contribution of an additional positive magnetisation was detected. This is probably due to a redistribution of stray fields in this region when the Nb becomes superconducting, with similar mechanism as discussed in Chapter 2.

The other important feature of this sample is the lack of Meissner screening in the Nb

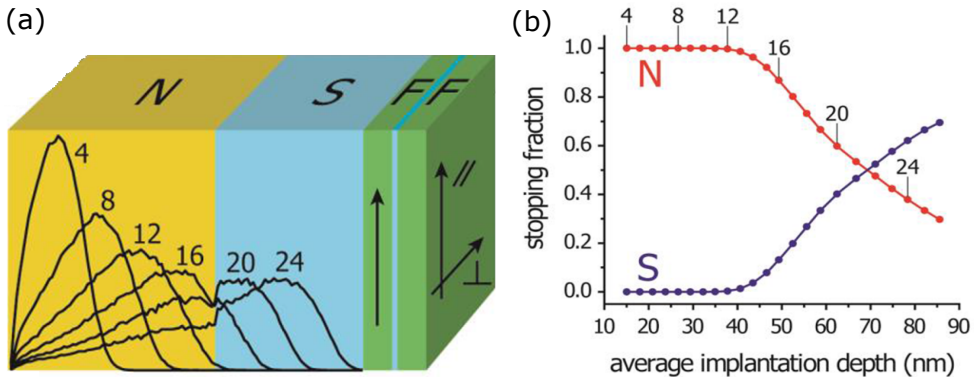

Figure 6.5: Resulting Monte Carlo simulations for (a) the stopping profile of accelerated muons entering the sample and (b) the fraction of muons stopped in the N (Au) and S (Nb) layers. Adapted from an early draft of [231].

layer. At a thickness of 50 nm the Nb layer is significantly thinner than the penetration depth. From the errors in Figure 6.4 an upper limit can be set that any Meissner screening contributes less than 1 G (or less than 1% of the applied field) to the measured signal.

73 nm Gold Cap

The next sample considered has a 73 nm Au capping layer. At this thickness the Au provides strong moderation of the incoming muons energy, allowing for measurements purely inside the Au, or at higher energies a stopping profile which peaks inside the Nb layer. Figure 6.5 shows the calculated stopping profiles and extracted stopping fractions for this sample.

Performing the same measurements as that of the thin Au sample immediately shows a large difference between 10 and 3 K. Figure 6.6 shows that in this sample, at all measured energies, there is a lowering of the local field value upon cooling through T_c.

It is next important to establish that the observed effect is indeed due to the onset of superconductivity in the sample. To do this, a single energy of muon implantation is chosen (12 keV) and the measurement is performed at many fields. This is shown in Figure 6.7, where at the onset of superconductivity at 7.5 K, an immediate reduction in the local field occurs. By comparison, above T_c the field is constant from 25 to 8 K. For the chosen ferromagnet (Co) there is no change in magnetisation in this temperature range, allowing the attribution of the observed effect to be due entirely to the onset of superconductivity.

At the chosen energy value of 12 keV the stopping fraction of muons is entirely inside

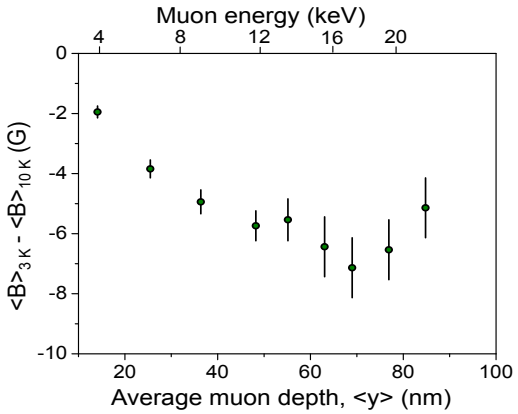

Figure 6.6: The change in local field upon cooling through the superconductors T_c as a function of implantation depth into the heterostructure.

the Au layer, suggesting that the observed effect is much more complicated than Meissner expulsion from within the superconducting layer. It is therefore important next to calculate the profile of the induced magnetisation responsible for the lowering of the local field value below T_c.

So far data analysis has been performed on the individual data sets corresponding to each energy and temperature value. While fitting each of these asymmetries separately provides a good indication of the local field, it is not a particularly powerful method to extract an overall field profile, due to the large spread of stopping positions and overlapping in stopping profiles between progressive implantation energies.

The data is therefore treated with the muon fitting program developed by Dr. M. G. Flokstra, as outlined in Chapter 3 and detailed in references [203, 231]. It is now possible to fit a function to all datasets simultaneously. Goodness of fit is returned by χ^2 analysis.

In the fitting program, the Au/Nb interface is defined from the known thicknesses. The two layers are treated separately, where any induced moment is allowed to either grow or decay with any length in a Gaussian type profile from this defined interface. Additionally, the interface can be arbitrarily moved.

Employing this analysis returns a best fit for the profile of induced moment shown in Figure 6.8. Here the red and blue lines correspond to the returned fit to the 10 K (red) and 3 K (blue) data. The black curve shows the profile of induced magnetisation corresponding to the fit. In addition, the returned field values from the fitting of individual asymmetries is shown as the circles. Good agreement between the fit and circles show the accuracy of the

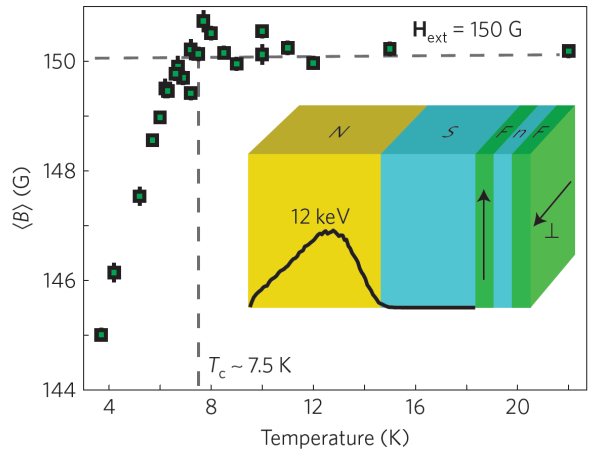

Figure 6.7: Measured local field with temperature, showing no change above the superconducting transition and sharp decrease at the onset of superconductivity. Inset: the stopping profile at 12 keV where the measurements were performed. Reproduced from [231]

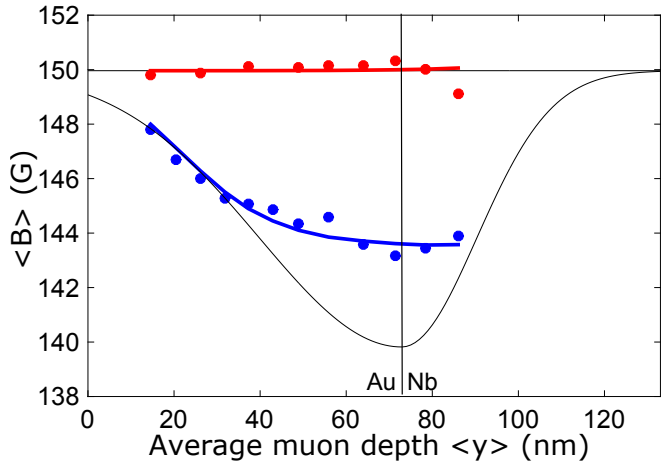

Figure 6.8: Returned best fits (solid coloured lines) to the experimental data (represented by the circles). The black curve indicates the profile of induced magnetisation corresponding to the fit.

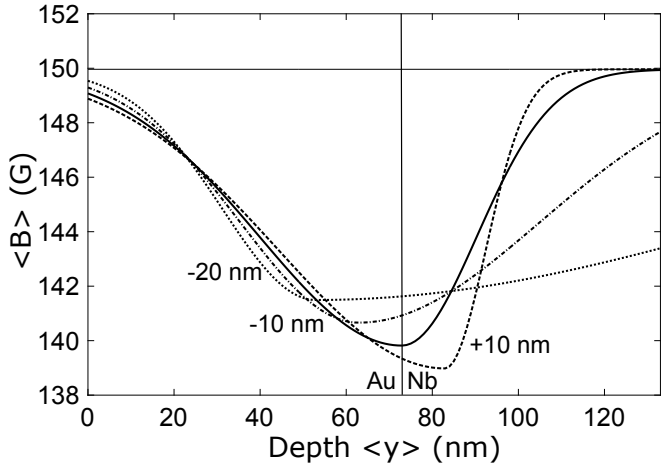

Figure 6.9: The returned best fit to the experimental data showed a peak at the Au/Nb interface (Figure 6.8 and solid curve). It is important to establish if this peak truly exists at the interface by allowing the peak position to vary. Here, the range in induced magnetisation profiles returned by fixing the peak location and fitting the experimental data are shown. The returned χ^2 analysis in this range is shown in Figure 6.10.

proposed profile of induced magnetisation.

Above T_c, at all measured energies no change is seen in the induced moment. This is reflected in the flat red field profile showing only the applied field of 150 K. Below T_c there is an additional magnetic contribution from the sample, which opposes the applied field and lowers the measured field value. This is caused by an additional induced moment inside the sample.

Below T_c, the returned induced magnetisation profile shows the additional induced magnetisation has a maximum at the Au/Nb interface. The moment decays inside the Au with a length scale of approximately 30 nm. Inside the Nb layer, the moment decays approximately twice as quickly and is zero at the Nb/Co interface.

Next, it is important to check that the induced moment is truly maximum at the Au/Nb interface. This can be done by artificially moving the interface in the model and examining the returned induced magnetisation profiles, which are plotted in Figure 6.9. This effectively changes the location of the maximum induced moment.

Moving the location of the maximum induced moment has a drastic effect on the profile of the induced magnetisation. Moving into the Nb layer increases the peak moment and decay length into the Au layer. The consequence of this is a much sharper decay into the Nb

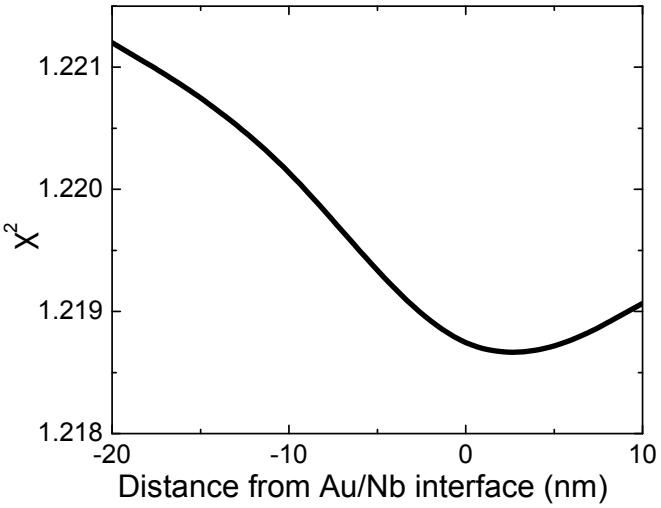

Figure 6.10: Returned χ^2 in the range of the possible profiles in Figure 6.9. The minimum in χ^2 confirms that the peak in induced moment exists at the Au/Nb interface.

layer (to keep the total induced moment approximately the same in all possible profiles).

Moving into the Au layer does the opposite to the induced magnetisation profile. Placing the peak in moment at 10 nm into the Au makes the decay lengths in the two layers symmetric (traditional Meissner type response inside a superconductor). Moving further into the Au drastically increases the decay length and total moment inside the Nb layer.

To establish where the peak in induced moment exists, χ^2 analysis is applied to each model to find the best fit to the experimental data. Figure 6.10 shows the returned χ^2 value obtained by changing the location of the peak in moment in the previous figure. The lowest χ^2 is returned for the peak in moment being located at the Au/Nb interface (within the error of the known thicknesses of the two layers).

6.4.3 Using PNR Technique

The profile of the induced magnetism Au/Nb interface has been extracted from the muon data. This technique has shown this induced moment is reproducible across multiple samples, next it is important to establish if the effect can be observed in other techniques. PNR has already been employed to characterise the spin valves, and a physical model of the device structure has been extracted. To see if the induced moment can be observed in this technique, the following experimental procedure was undertaken; set up the magnetic config-

uration of the spin valve and take a high fidelity measurement above T_c (10 K). The error bar on each point is governed purely by Poisson statistics, hence requiring long measurement times (in the order of 1 day) for detecting subtle effects. The sample was cooled through T_c and the measurement repeated at the base temperature of the cryostat to look for differences created by the superconducting state.

PNR has the additional benefit of being able to probe buried interfaces, so if there was additional induced moment elsewhere in the structure this should be visible. The 'usual' sensitivity of PNR is around 0.05 μ_B/atom, which from simulations would be on the limit in terms of observing the effect. In order to maximise the chance of observing any effect, the POLREF beamline at ISIS was used due to its improved background and resolution. The general model of the 70 nm gold capped spin valve from Section 6.3 was employed in the normal state, with small modifications made to take into account for the improved reflectometry data now available and the changes to the magnetic layers between room temperature and 10 K (although these changes were typically only 10 %).

Figure 6.11 **(a)** shows the spin asymmetry of the two measured temperatures, 10 K (red) and 3 K (blue), for the acquired reflectivity data (positive offset) and model (negative offset). The range shown encompasses the critical edge (which is sensitive to changes in the total magnetisation) and the length scale of the effective coherence lengths inside the superconducting system (where any signals from superconducting effects should be largest). Considering first the positive offset data. The spin asymmetry is, to a first approximation, independent of the structural parameters and depends only on the magnetic structure, thus the changes seen between the datasets are indicative of a magnetic response caused by the onset of superconductivity.

The negative offset 10 K model is the best possible fit to the 10 K reflectivity which satisfies the prerequisites of the physical model outlined before. The differences in reflectivity are too subtle to allow quantitative fitting, so instead a magnetic response in the Au capping layer consistent with the profile obtained from the muon fitting was superimposed onto the fit. In the neutron model this corresponds to an induced moment of 0.015 μ_B/atom with a decay length of 20 nm and is shown as the negative offset 3 K (blue) line.

The position, size and direction of the differences between the 10 K fit and 3 K model agree very well with the differences in the datasets. This is demonstrated further in Figure 6.11 **(b)**. Here a Δ spin asymmetry is defined as the differences between 10 K and 3 K datasets and is plotted as the square points which are joined by the thin solid line for clarity. In order

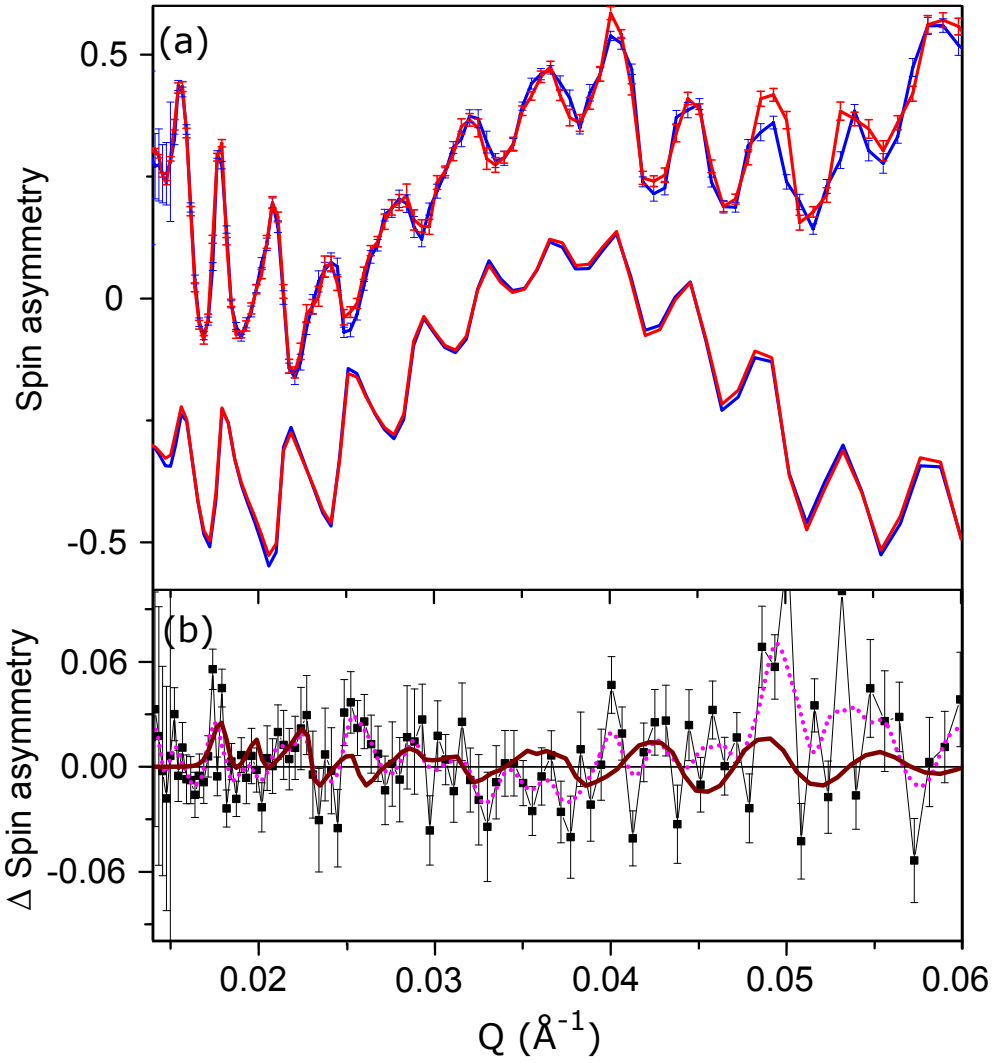

Figure 6.11: **(a)** The spin asymmetry at 10 K (red) and 3 K (blue) with positive (negative) offset for the the reflectivity data (model - see text). **(b)** The changes in the spin asymmetry between 10 K and 3 K with a guide of the eye (connected squares and dotted line) and the change in the model's spin asymmetry when introducing the induced magnetisation profile (solid line).

to aid the reading of the dataset, a next nearest neighbour smoothing function is applied to the dataset and is plotted as the pink dotted line. The purpose of this line is only as a guide for the eye through the general trend of the dataset. On top of the dataset a further solid line is plotted showing the differences between the 10 K fit and the 3 K model.

It is striking, especially at lower Q, how closely the model follows the trends seen in the dataset. While the magnitude of the peaks may be slightly different, up until approximately 0.035 $Å^{-1}$ the peak positions match that of the smoothed data set. In the region corresponding to 0.035-0.045 $Å^{-1}$ the model begins to deviate from the smoothed dataset. Examination of the data points show that the Δ spin asymmetry in this region is generally positive. The model reproduces this trend, and peaks with the cluster of data points around 0.0425 $Å^{-1}$. There is also strong correlation with the large Δ spin asymmetry observed at around 0.05 $Å^{-1}$. At higher Q the error bars become larger and so no further information can be extracted from the trends in Δ spin asymmetry.

Clearly an induced moment of 0.015 μ_B/atom is well below the PNR techniques accepted sensitivity of 0.05 μ_B/atom. The reason that this effect is observable at all is due to the extremely high fidelity of the acquired data and the length scale of the induced moment. Additionally, when in this perpendicular magnetic configuration, PNR is insensitive to two of the three magnetic layers. Comparing the absolute magnetism above and below T_c, the induced moment decaying over the long length scale contributes to approximately a 10 % change to the 'total' magnetism.

6.5 Comparison to Theory

Chapter 2 outlined three possible theoretical descriptions for the profile of induced magnetic response in S/F systems. Here comparison of the experimental data to theory are presented with possible mechanisms outside of established theory proposed.

6.5.1 Differences from Expected Theory

Firstly considering traditional Meissner screening as the origin of the effect. In order for Meissner screening to take place in the plane of the sample (the direction of these measurements sensitivity), the thickness of the superconductor must be comparable in size to the magnetic penetration depth. For thick Nb films $\lambda_{GL} \approx 95$ nm, or about twice the layer thickness [34]. In the thickness regime studied here it is very likely longer than this. If one

were to create a system of adequate thickness to establish a screening current, the expected profile would be largest at the centre of the superconductor, decaying at the interfaces, as observed in reference [34]. It is also worth noting that the size of the Meissner screening effect in previous work (for example [34] where the Nb layer which is over twice as thick as in this chapter) is smaller than the effect observed here. It is possible for a small amount of screening current to enter the normal metal, however any screening inside the normal metal would be small. It is highly unlikely for a Meissner screening profile to have maximum at the interface with, or so close to, a normal metal.

When considering the inverse Meissner screening effect [81–85] with relevance to this work, what is clear is that this effect does not manifest from the location of LRTC generation, or where the LRTC would be a maximum. The effect manifests at the N/S interface, which is inconsistent with the expected spatial variation of screening currents and the observed temperature dependence shows no oscillations in sign. This theory cannot explain the observations of this work. It is therefore concluded to be an induced ferromagnetism.

Considering the inverse proximity theory of Bergeret *et al.* [74] a couple of similarities can be seen. The moment is induced in the opposite direction to the ferromagnetic moment. It is largest at the interface and decays exponentially over the effective coherence length of the material. However, the induced moment manifests at the wrong interface. It is expected that the inverse proximity effect occurs at the S/F interface, instead the induced magnetisation appears at the N/S interface. In fact, no induced moment is observed at the S/F interface in any measurements during this study.

The same is true when considering the theory of Löfwander *et al.* [63]. The maximum triplet generation will be at the S/F interface. Any induced moment should be at a maximum here.

6.6 Possible Mechanisms

What is observed, in two complementary techniques, is a type of induced magnetism not currently attributable to the established theory of superconductivity. Having ruled out the traditional mechanisms for induced moment in S/F proximity structures it is important to identify possible routes for a complete theoretical description of this effect. The key question to address here is how the remote magnetisation in the normal metal layer can be provided by the superconductivity of the interlayer.

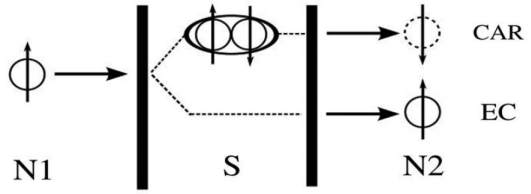

Figure 6.12: Nonlocal correlations near the N1/S/N2 structure. Pure spin current is injected from N1 and a finite spin current is generated in N2 by CAR and EC. One should note that the direction of the spin currents attributed to CAR and EC are in the same direction and there is no net spin accumulation in the superconductor. Adapted from [232].

6.6.1 Spin Transfer Across the Superconducting Interlayer

Andreev reflections into singlet Cooper pairs at a S/N interface cannot transfer a net spin across the interface. When the superconductor has multiple interfaces which are (relatively) close to one another (on the length scale of a few ξ_s), nonlocal effects such as crossed Andreev reflection (CAR) and elastic co-tunnelling (EC) become possible [232].

Considering two normal metals in contact with a superconductor (an N/S/N multilayer). In CAR, an electron with one spin orientation, e.g., spin up, is injected from the first normal metal into the superconductor, resulting in a hole with spin down being injected from the superconductor into the second normal metal, with generation of a Cooper pair in the superconductor. In the second process, EC, the incoming spin up electron from the first normal metal enters the superconductor by pairing with a spin down electron from an already existing Cooper pair, which in turn simultaneously donates its original spin up electron to the second normal metal layer [232]. These processes are shown schematically in Figure 6.12.

Modifying this process to a F/S/N structure changes this picture slightly. Here a spontaneous spin accumulation is needed to create an energy-dependent imbalance between the spin density on either side of the superconductor. This imbalance can result from the inverse proximity effect of Bergeret *et al.* where electrons aligned with the ferromagnet will preferentially enter the ferromagnet, creating a spin imbalance. Although the induced magnetisation from inverse proximity effect was not observed in this system, there is a suppression of T_c when the superconductor is grown next to the ferromagnet. This is evidence of a weakened order parameter at the S/F interface, one signature of inverse proximity in a superconducting heterostructure. It has also been shown by transport measurements on the

structures that triplet proximity effects do exist in these samples which necessarily means the presence of spin aligned Cooper pairs at the S/F interface. Theoretically it is proposed that spin currents appear in SFF spin valves with non-collinear spin alignment, even in an unbiased structure, but disappear in the collinear alignment [233, 234].

The presence of spin imbalance from any of the above mechanisms limits the possible CAR and EC processes. For CAR a Cooper pair can only be created by taking a spin down electron from the F layer, or annihilated by donating a spin up electron to the F layer. For EC spin down electrons can only move from F to N and spin up electrons can only move from N to F. All possible processes result in a net spin down on the N side and a net spin up on the F side, thus effectively transferring spin across the S layer.

6.6.2 Anomalous Meissner Screening

An upper limit on the size of the traditional Meissner screening contribution has been measured as 1% of the applied field. Traditional Meissner screening would be maximum at the centre of the superconducting layer, not the S/N interface. It is possible however, that the addition of the thick Au layer on top of the Nb has modified the system enough that anomalous Meissner screening occurs.

There exists a small number of experimental reports that normal metals coupled to bulk superconductors can exhibit large Meissner screening [235, 236]. Although it has not been observed in the thin film, or in a technique with the spatial sensitivity of the neutron and muon techniques employed in this work, it is at least possible that the Au coupled to the superconducting Nb can exhibit an anomalous Meissner screening response. Theoretically, under certain limits, it is possible for normal metals coupled to superconductors to show Meissner screening [237–240]. While this screening effect can have influence over a long range, it is not clear if the screening inside the normal metal would be significantly higher in comparison to the adjacent superconductor or if it could occur even when screening was not observed in the superconductor on its own, as it was in this chapter. None of these works consider the addition of the ferromagnetic layers in the heterostructure, which is important in these structures.

6.7 Conclusions

In this Chapter the local magnetic profile of superconducting spin valves were studied. Using lab based transport techniques there was considerable evidence for triplet proximity effects in the samples. Muon and neutron techniques were used to search for the three possible signals attributable to the presence of triplet Cooper pairs in the heterostructure.

None of the samples measured using the muon or neutron facilities showed induced moment immediately attributable to the accepted proposal of triplet superconductivity. It was also possible to rule out traditional Meissner expulsion as the origin of observed effect.

Two possible mechanisms that would account for the observations were introduced, however of all the theories discussed, none are satisfactory for explaining the observations. It is therefore of importance for new theoretical work to explain why the three measurement techniques on the same sample don't agree on the nature of the triplet pair at the S/F interface.

Chapter 7

Conclusions, Further Work and Future Outlook

Proximity effects at the superconductor/ferromagnet interface provide a wealth of new physical phenomena. The triplet Cooper pair has been the source of theoretical and experimental interest since the first observation 10 years ago, with the publication of over 300 research papers in that time. This thesis set out with two aims. To provide new candidate materials in which to study S/F proximity effects, and to probe the nature of the triplet Cooper pair. Here the important steps leading to, and the results obtained in addressing, these aims are summarised.

7.1 Conclusion

With the aim of providing new candidate materials for super-spintronics, this thesis reported the successful growth and integration into devices of thin film Er in Chapter 4. The epitaxial Er films were found, in the thickest regime studied, to retain all bulk-like magnetic phases, including the ferromagnetic conical phase not observed in thin film before. Upon reduction of thickness the lower temperature magnetic phases began to be suppressed, but even in the thinnest film studied there was some evidence that the spiral magnetic state was retained. The growth of Er is preceded by a Nb buffer layer. This is advantageous when considering the creation of super-spintronic devices for application due to the favourable T_c and popularity of Nb in established superconducting logic [5].

A prototypical Nb/Er bilayer device was fabricated in Chapter 5. Two control mechanisms for the control of T_c in the bilayer were demonstrated. First it was shown that as a function of Er thickness a re-entrant type of oscillatory T_c may be observed. While maintaining similar features to such oscillations caused by the FFLO state at superconductor / homogeneous ferromagnet interfaces, the Nb/Er bilayer is more complicated, and could not be fitted by established theory. This was most likely due to generation and mixing of the LRTC at the interface with the inhomogeneous magnetism competing with the FFLO oscillations.

A second type of bilayer was fabricated with a thicker Er layer, to allow access to more of the metastable magnetic phases. By manipulation of the metastable magnetic state of the Er at remanence, a superconducting 'switch' was realised. Such a switch satisfied the requirements of the cryogenic memory element first proposed by Oh *et al.* [14] with several key advantages. Firstly, once the state was set the information about the state was retained at remanence. Secondly, unlike the proposed spin-valve structure, no rotation of the device in a field was needed. Finally, the observed suppression in T_c of 140 mK was larger than that

seen in the superconducting spin valve.

Chapter 6 considered the local magnetic state of the superconducting spin valve, the prototypical device for super-spintronics. In these structures the response of the superconducting layer to rotation of the ferromagnets was consistent with established theory. The same theoretical framework predicted an inducted magnet moment at the superconductor / ferromagnet interface from triplet Cooper pairs. While studying these interfaces the predicted moment was not observed. Rather, a new induced moment at a remote normal metal / superconductor interface was found using the LEμSR and PNR techniques. This moment decayed away from this interface and was not present at the superconductor / ferromagnet interface. Finally, possible mechanisms towards a complete theoretical description of this new effect were presented.

In conclusion, direct observation of a long ranged triplet component to the superconducting condensate was not explicitly observed in this thesis. While any contribution to the studied samples ferromagnetism could have been too small, the presence of a hitherto unpredicted ferromagnetism present inside a normal metal capping layer suggests that the results of this thesis require a re-formulation of established theory.

7.2 Further Work and Outlook

7.2.1 Erbium Characterisation

Due to time constraints on the neutron beamline, it was not possible to perform all the measurements one would ideally want to fully characterise the magnetic state of the Er. Given further opportunities to investigate this topic it would be interesting to examine a wider sample set.

To help with the interpretation of Chapter 5, work understanding the field history dependence of the magnetic structure should be undertaken. This could be performed with the PNR or neutron diffraction techniques in a large applied field. The neutron diffraction measurements would be able to detect the breakdown of the meta-stable magnetic states and give a definitive identification of the post-saturation state. It would also be interesting to perform PNR at saturation of the thinnest Er sample, to understand the complete unwinding and re-zipping of the spiral magnetisation.

Additionally, it would be interesting to study in more detail the crossover in thickness from saturation in-plane having the largest magnetisation, to the out-of-plane component

becoming the larger at saturation.

7.2.2 Nb/Er Bilayer Devices

The most important aspects of the bilayers results which need further work are the confirmation of the oscillation period, and the confirmation that the observed oscillation is of the type seen in standard S/F bilayers. It also remains to fit a model which accurately reproduces all of the features.

Trivial origins of the stepped transition observed in Nb/Er bilayers have been effectively ruled out, leaving the possibility that these steps originate from the proximity effect.

7.2.3 The Superconducting Spin-Valve

The discovery of an induced moment appearing in a normal metal coupled to a superconducting spin valve is perhaps the most surprising and least understood result in this thesis. The largest open questions are:

1) What is the origin of this effect?

The presented mechanisms for spin transfer through a superconductor are expected to have dependence on superconductor thickness, decaying on the length scale of the coherence length. It would therefore be of great interest to perform measurements of the effect as a function of superconductor thickness. Care would have to be taken to avoid Meissner screening which would become larger with thicker films.

To probe the question of anomalous Meissner screening, removing layers from the structure to simplify it to the point the effect disappears would be interesting to try. This could also be done by placing insulating layers throughout the structure, to remove key interfaces without changing the stray fields in the system.

2) Does it work with other metals?

Gold was chosen because it does not oxidise and hence makes a good capping material. From the perspective of superconducting proximity in the thin film, it is not a particularly well studied system. There are competing reports in literature on the length scale and nature of the proximity effect [241, 242]. Substituting for other normal metal caps with different electrical properties (such as mean free path and spin diffusion length) could help in understanding the key length scale involved in the effect.

The allocation of beamtime means that only one experiment to study this effect more using LEμSR can be undertaken in a year. It would therefore be an important discovery

to find signatures of the effect which are detectable in electrical transport of nano-devices. These have the potential for measurement in the lab, and are more readily converted to super-spintronic logic device application.

REFERENCES

[1] World Energy Council, World energy resources: 2013 survey, *Survey of Energy Resources* (2013)

[2] M. P. Mills, The cloud begins with coal, *Digital Power Group* (2013)

[3] G. Cook, How clean is your cloud? Catalysing an energy revolution, *Greenpeace International* (2012)

[4] W. Chen, A. Rylyakov, V. Patel, J. Lukens and K. Likharev, Rapid single flux quantum t-flip flop operating up to 770 GHz, *Applied Superconductivity, IEEE Transactions on* **9**, 3212 (1999)

[5] D. S. Holmes, A. L. Ripple and M. Manheimer, Energy-efficient superconducting computing–power budgets and requirements, *Applied Superconductivity, IEEE Transactions on* **23**, 1701610 (2013)

[6] M. Eschrig, Spin-polarized supercurrents for spintronics, *Physics Today* **64**, 43 (2011)

[7] I. Žutić, J. Fabian and S. D. Sarma, Spintronics: Fundamentals and applications, *Reviews of modern physics* **76**, 323 (2004)

[8] J. Linder and J. W. A. Robinson, Superconducting spintronics, *Nature Physics* **11**, 307 (2015)

[9] A. G. Mal'shukov and A. Brataas, Triplet supercurrent in ferromagnetic Josephson junctions by spin injection, *Phys. Rev. B* **86**, 094517 (2012)

[10] C. H. L. Quay, D. Chevallier, C. Bena and M. Aprili, Spin imbalance and spin-charge separation in a mesoscopic superconductor, *Nature Physics* **9**, 84 (2013)

[11] F. Giazotto and F. S. Bergeret, Quantum interference hybrid spin-current injector, *Applied Physics Letters* **102**, 162406 (2013)

[12] T. Yamashita, K. Tanikawa, S. Takahashi and S. Maekawa, Superconducting π qubit with a ferromagnetic Josephson junction, *Phys. Rev. Lett.* **95**, 097001 (2005)

[13] I. V. Vernik, V. V. Bol'ginov, S. V. Bakurskiy, A. A. Golubov, M. Y. Kupriyanov et al., Magnetic Josephson junctions with superconducting interlayer for cryogenic memory, *Applied Superconductivity, IEEE Transactions on* **23**, 1701208 (2013)

[14] S. Oh, D. Youm and M. R. Beasley, A superconductive magnetoresistive memory element using controlled exchange interaction, *Applied Physics Letters* **71**, 2376 (1997)

[15] E. Goldobin, H. Sickinger, M. Weides, N. Ruppelt, H. Kohlstedt et al., Memory cell based on a φ Josephson junction, *Applied Physics Letters* **102**, 242602 (2013)

[16] B. Baek, W. H. Rippard, S. P. Benz, S. E. Russek and P. D. Dresselhaus, Hybrid superconducting-magnetic memory device using competing order parameters, *Nat. Commun.* **5** (2014)

[17] B. Niedzielski, S. Diesch, E. Gingrich, Y. Wang, R. Loloee et al., Use of Pd-Fe and Ni-Fe-Nb as soft magnetic layers in ferromagnetic Josephson junctions for nonvolatile cryogenic memory, *IEEE Transactions on Applied Superconductivity* **24**, 1 (2014)

[18] E. C. Gingrich, B. M. Niedzielski, J. A. Glick, Y. Wang, D. L. Miller et al., Controllable 0-π Josephson junctions containing a ferromagnetic spin valve., *Nature Physics* p. doi:10.1038/nphys3681 (2016)

[19] P. V. Leksin, N. N. Garif'yanov, I. A. Garifullin, Y. V. Fominov, J. Schumann et al., Evidence for Triplet Superconductivity in a Superconductor-Ferromagnet Spin Valve, *Phys. Rev. Lett.* **109**, 057005 (2012)

[20] A. A. Jara, C. Safranski, I. N. Krivorotov, C.-T. Wu, A. N. Malmi-Kakkada et al., Angular dependence of superconductivity in superconductor/spin-valve heterostructures, *Phys. Rev. B* **89**, 184502 (2014)

[21] X. L. Wang, A. Di Bernardo, N. Banerjee, A. Wells, F. S. Bergeret et al., Giant triplet proximity effect in superconducting pseudo spin valves with engineered anisotropy, *Phys. Rev. B* **89**, 140508 (2014)

[22] M. G. Flokstra, T. C. Cunningham, J. Kim, N. Satchell, G. Burnell et al., Controlled suppression of superconductivity by the generation of polarized Cooper pairs in spin-valve structures, *Phys. Rev. B* **91**, 060501 (2015)

[23] N. W. Ashcroft and N. D. Mermin, *Solid State Physics*, Brooks/Cole (1976)

[24] S. Blundell, *Magnetism in Condensed Matter*, OUP Oxford, new edition (2001)

[25] M. Tinkham, *Introduction to Superconductivity: Second Edition (Dover Books on Physics)*, Dover Publications, 2 edition (2004)

[26] J. F. Annett, *Superconductivity, superfluids, and condensates*, Oxford University Press (2004)

[27] M. Howson, Magnetism of thin films and multilayers, *Contemporary Physics* **35**, 347 (1994)

[28] E. C. Stoner, Collective electron ferromagnetism, *Proceedings of the Royal Society of London. Series A, Mathematical and Physical Sciences* pp. 372–414 (1938)

[29] S. S. Parkin, M. Hayashi and L. Thomas, Magnetic domain-wall racetrack memory, *Science* **320**, 190 (2008)

[30] H. Kamerlingh-Onnes, *Leiden Comm.* **120b, 122b, 124c** (1911)

[31] F. London and H. London, The electromagnetic equations of the supraconductor, *Proceedings of the Royal Society of London A: Mathematical, Physical and Engineering Sciences* **149**, 71 (1935)

[32] L. P. Gor'kov, Microscopic derivation of the Ginzburg-Landau equations in the theory of superconductivity, *Sov. Phys. JETP* **9**, 1364 (1959)

[33] M. G. Flokstra, S. J. Ray, S. J. Lister, J. Aarts, H. Luetkens et al., Measurement of the spatial extent of inverse proximity in a Py/Nb/Py superconducting trilayer using low-energy muon-spin rotation, *Phys. Rev. B* **89**, 054510 (2014)

[34] A. Di Bernardo, Z. Salman, X. Wang, M. Amado, M. Egilmez et al., Intrinsic Paramagnetic Meissner Effect Due to *s*-Wave Odd-Frequency Superconductivity, *Phys. Rev. X* **5**, 041021 (2015)

[35] J. Bardeen, L. N. Cooper and J. R. Schrieffer, Theory of Superconductivity, *Phys. Rev.* **108**, 1175 (1957)

[36] J. Bardeen, L. N. Cooper and J. R. Schrieffer, Microscopic Theory of Superconductivity, *Phys. Rev.* **106**, 162 (1957)

[37] L. N. Cooper, Bound electron pairs in a degenerate fermi gas, *Physical Review* **104**, 1189 (1956)

[38] A. P. Mackenzie and Y. Maeno, The superconductivity of Sr_2RuO_4 and the physics of spin-triplet pairing, *Rev. Mod. Phys.* **75**, 657 (2003)

[39] V. L. Berezinskii, New model of the anisotropic phase of superfluid ^{3}He, *JETP Lett.* **20**, 287 (1974)

[40] F. Bergeret, A. Volkov and K. Efetov, Long-Range Proximity Effects in Superconductor-Ferromagnet Structures, *Phys. Rev. Lett.* **86**, 4096 (2001)

[41] A. I. Buzdin, Proximity effects in superconductor-ferromagnet heterostructures, *Rev. Mod. Phys.* **77**, 935 (2005)

[42] F. S. Bergeret, A. F. Volkov and K. B. Efetov, Odd triplet superconductivity and related phenomena in superconductor-ferromagnet structures, *Rev. Mod. Phys.* **77**, 1321 (2005)

[43] M. Eschrig, Spin-polarized supercurrents for spintronics: a review of current progress, *Reports on Progress in Physics* **78**, 104501 (2015)

[44] P. G. de Gennes, Boundary effects in superconductors, *Rev. Mod. Phys.* **36**, 225 (1964)

[45] P. de Gennes, *Superconductivity of Metals and Alloys*, Advanced book classics, Addison-Wesley (1994)

[46] A. Andreev, Thermal conductivity of the intermediate state of superconductors, *Zh. Eksperim. i Teor. Fiz.* **46** (1964)

[47] M. Eschrig, Theory of Andreev Bound States in S-F-S Junctions and S-F Proximity Devices, *arXiv:1509.07818 [cond-mat]* (2015), arXiv: 1509.07818

[48] P. Fulde and R. A. Ferrell, Superconductivity in a Strong Spin-Exchange Field, *Phys. Rev.* **135**, A550 (1964)

[49] A. Larkin and Y. Ovchinnikov, Nonuniform state of superconductors, *Sov. Phys. JETP* **20** (1965)

[50] M. Eschrig and T. Löfwander, Triplet supercurrents in clean and disordered half-metallic ferromagnets, *Nature Physics* **4**, 138 (2008)

[51] J. W. A. Robinson, J. D. S. Witt and M. G. Blamire, Controlled Injection of Spin-Triplet Supercurrents into a Strong Ferromagnet, *Science* **329**, 59 (2010)

[52] M. S. Anwar, F. Czeschka, M. Hesselberth, M. Porcu and J. Aarts, Long-range supercurrents through half-metallic ferromagnetic CrO_2, *Phys. Rev. B* **82**, 100501 (2010)

[53] M. Eschrig, J. Kopu, A. Konstandin, J. C. Cuevas, M. Fogelström et al., Singlet-triplet mixing in superconductor-ferromagnet hybrid devices, in *Advances in Solid State Physics*, Springer, pp. 533–545 (2004)

[54] T. Champel and M. Eschrig, Switching superconductivity in superconductor/ferromagnet bilayers by multiple-domain structures, *Phys. Rev. B* **71**, 220506 (2005)

[55] D. Fritsch and J. F. Annett, Triplet superconductivity and proximity effect induced by Bloch and Néel domain walls, *Supercond. Sci. Technol.* **28**, 085015 (2015)

[56] I. Sosnin, H. Cho, V. T. Petrashov and A. F. Volkov, Superconducting Phase Coherent Electron Transport in Proximity Conical Ferromagnets, *Phys. Rev. Lett.* **96**, 157002 (2006)

[57] C.-T. Wu, O. T. Valls and K. Halterman, Reentrant Superconducting Phase in Conical-Ferromagnet/Superconductor Nanostructures, *Phys. Rev. Lett.* **108**, 117005 (2012)

[58] C.-T. Wu, O. T. Valls and K. Halterman, Proximity effects in conical-ferromagnet/superconductor bilayers, *Phys. Rev. B* **86**, 184517 (2012)

[59] D. Fritsch and J. F. Annett, Proximity effect in superconductor/conical magnet/ferromagnet heterostructures, *New J. Phys.* **16**, 055005 (2014)

[60] D. Fritsch and J. F. Annett, Proximity effect in superconductor/conical magnet heterostructures, *J. Phys.: Condens. Matter* **26**, 274212 (2014)

[61] D. Fritsch and J. F. Annett, Spin-flipping with Holmium: case study of proximity effect in superconductor/ferromagnet/superconductor heterostructures, *Philosophical Magazine* **0**, 1 (2014)

[62] A. F. Volkov, F. S. Bergeret and K. B. Efetov, Odd Triplet Superconductivity in Superconductor-Ferromagnet Multilayered Structures, *Phys. Rev. Lett.* **90**, 117006 (2003)

[63] T. Löfwander, T. Champel, J. Durst and M. Eschrig, Interplay of Magnetic and Superconducting Proximity Effects in Ferromagnet-Superconductor-Ferromagnet Trilayers, *Phys. Rev. Lett.* **95**, 187003 (2005)

[64] K. B. Efetov, I. A. Garifullin, A. F. Volkov and K. Westerholt, Proximity effects in ferromagnet/superconductor heterostructures, in *Magnetic Heterostructures*, Springer, pp. 251–290 (2008)

[65] Y. V. Fominov, A. A. Golubov, T. Y. Karminskaya, M. Y. Kupriyanov, R. G. Deminov et al., Superconducting triplet spin valve, *JETP Lett.* **91**, 308 (2010)

[66] M. A. Silaev, Possibility of a long-range proximity effect in a ferromagnetic nanoparticle, *Phys. Rev. B* **79**, 184505 (2009)

[67] M. S. Kalenkov, A. D. Zaikin and V. T. Petrashov, Triplet Superconductivity in a Ferromagnetic Vortex, *Phys. Rev. Lett.* **107**, 087003 (2011)

[68] F. S. Bergeret and I. V. Tokatly, Singlet-Triplet Conversion and the Long-Range Proximity Effect in Superconductor-Ferromagnet Structures with Generic Spin Dependent Fields, *Phys. Rev. Lett.* **110**, 117003 (2013)

[69] S. H. Jacobsen and J. Linder, Giant triplet proximity effect in π-biased Josephson junctions with spin-orbit coupling, *Phys. Rev. B* **92**, 024501 (2015)

[70] S. Nakosai, Y. Tanaka and N. Nagaosa, Two-dimensional p-wave superconducting states with magnetic moments on a conventional s-wave superconductor, *Phys. Rev. B* **88**, 180503 (2013)

[71] T. Yokoyama and J. Linder, Josephson effect through magnetic skyrmions, *Phys. Rev. B* **92**, 060503 (2015)

[72] M. Hübener, D. Tikhonov, I. Garifullin, K. Westerholt and H. Zabel, The antiferromagnet/superconductor proximity effect in Cr/V/Cr trilayers, *J. Phys.: Condens. Matter* **14**, 8687 (2002)

[73] C. Bell, E. J. Tarte, G. Burnell, C. W. Leung, D.-J. Kang et al., Proximity and Josephson effects in superconductor/antiferromagnetic Nb/γ-$Fe_{50}Mn_{50}$ heterostructures, *Phys. Rev. B* **68**, 144517 (2003)

[74] F. S. Bergeret, A. F. Volkov and K. B. Efetov, Induced ferromagnetism due to superconductivity in superconductor-ferromagnet structures, *Phys. Rev. B* **69**, 174504 (2004)

[75] A. Scherz, H. Wende, P. Poulopoulos, J. Lindner, K. Baberschke et al., Induced V and reduced Fe moments at the interface of Fe/V(001) superlattices, *Phys. Rev. B* **64**, 180407 (2001)

[76] P. Fuchs, K. Totland and M. Landolt, Induced magnetization in thin epitaxial V films on Fe (100), *Phys. Rev. B* **53**, 9123 (1996)

[77] R. I. Salikhov, I. A. Garifullin, N. N. Garif'yanov, L. R. Tagirov, K. Theis-Bröhl et al., Experimental Observation of the Spin Screening Effect in Superconductor/Ferromagnet Thin Film Heterostructures, *Phys. Rev. Lett.* **102**, 087003 (2009)

[78] J. Xia, V. Shelukhin, M. Karpovski, A. Kapitulnik and A. Palevski, Inverse Proximity Effect in Superconductor-Ferromagnet Bilayer Structures, *Phys. Rev. Lett.* **102**, 087004 (2009)

[79] Y. N. Khaydukov, V. Aksenov, Y. V. Nikitenko, K. Zhernenkov, B. Nagy et al., Magnetic proximity effects in V/Fe superconductor/ferromagnet single bilayer revealed by waveguide-enhanced polarized neutron reflectometry, *Journal of superconductivity and novel magnetism* **24**, 961 (2011)

[80] Y. N. Khaydukov, B. Nagy, J.-H. Kim, T. Keller, A. Rühm et al., On the feasibility to study inverse proximity effect in a single S/F bilayer by polarized neutron reflectometry, *JETP Lett.* **98**, 107 (2013)

[81] F. S. Bergeret and N. García, Spin screening and antiscreening in a ferromagnet/superconductor heterojunction, *Phys. Rev. B* **70**, 052507 (2004)

[82] T. Yokoyama, Y. Tanaka and N. Nagaosa, Anomalous Meissner Effect in a Normal-Metal-Superconductor Junction with a Spin-Active Interface, *Phys. Rev. Lett.* **106**, 246601 (2011)

[83] S. Mironov, A. Mel'nikov and A. Buzdin, Vanishing Meissner effect as a Hallmark of in-Plane Fulde-Ferrell-Larkin-Ovchinnikov Instability in Superconductor-Ferromagnet Layered Systems, *Phys. Rev. Lett.* **109**, 237002 (2012)

[84] M. Alidoust, K. Halterman and J. Linder, Meissner effect probing of odd-frequency triplet pairing in superconducting spin valves, *Phys. Rev. B* **89**, 054508 (2014)

[85] C. Espedal, T. Yokoyama and J. Linder, Anisotropic paramagnetic meissner effect by spin-orbit coupling, *arXiv preprint arXiv:1601.03404* (2016)

[86] A. Buzdin and M. Y. Kupriyanov, Transition temperature of a superconductor-ferromagnet superlattice, *JETP Lett.* **52** (1990)

[87] Z. Radović, M. Ledvij, L. Dobrosavljević-Grujić, A. Buzdin and J. R. Clem, Transition temperatures of superconductor-ferromagnet superlattices, *Phys. Rev. B* **44**, 759 (1991)

[88] J. Jiang, D. Davidović, D. H. Reich and C. Chien, Oscillatory superconducting transition temperature in Nb/Gd multilayers, *Phys. Rev. Lett.* **74**, 314 (1995)

[89] L. Mercaldo, C. Attanasio, C. Coccorese, L. Maritato, S. Prischepa et al., Superconducting-critical-temperature oscillations in Nb/CuMn multilayers, *Phys. Rev. B* **53**, 14040 (1996)

[90] Y. Obi, M. Ikebe, T. Kubo and H. Fujimori, Oscillation phenomenon of transition temperatures in Nb/Co and V/Co superconductor/ferromagnet multilayers, *Physica C: Superconductivity* **317**, 149 (1999)

[91] A. Sidorenko, V. Zdravkov, A. Prepelitsa, C. Helbig, Y. Luo et al., Oscillations of the critical temperature in superconducting Nb/Ni bilayers, *Annalen der Physik* **12**, 37 (2003)

[92] I. A. Garifullin, D. A. Tikhonov, N. N. Garif'yanov, L. Lazar, Y. V. Goryunov et al., Reentrant superconductivity in the superconductor/ferromagnet V/Fe layered system, *Phys. Rev. B* **66**, 020505 (2002)

[93] T. Mühge, N. Garif'yanov, Y. V. Goryunov, G. Khaliullin, L. Tagirov et al., Possible origin for oscillatory superconducting transition temperature in superconductor/ferromagnet multilayers, *Phys. Rev. Lett.* **77**, 1857 (1996)

[94] M. Vélez, M. Cyrille, S. Kim, I. Schuller and J. Vicent, Influence of magnetic order in the superconducting properties of Nb/Fe/Cu multilayers, *Journal of magnetism and magnetic materials* **203**, 233 (1999)

[95] L. Lazar, K. Westerholt, H. Zabel, L. Tagirov, Y. V. Goryunov et al., Superconductor/ferromagnet proximity effect in Fe/Pb/Fe trilayers, *Phys. Rev. B* **61**, 3711 (2000)

[96] V. A. Oboznov, V. V. Bol'ginov, A. K. Feofanov, V. V. Ryazanov and A. I. Buzdin, Thickness Dependence of the Josephson Ground States of Superconductor-Ferromagnet-Superconductor Junctions, *Phys. Rev. Lett.* **96**, 197003 (2006)

[97] J. W. A. Robinson, S. Piano, G. Burnell, C. Bell and M. G. Blamire, Critical Current Oscillations in Strong Ferromagnetic π Junctions, *Phys. Rev. Lett.* **97**, 177003 (2006)

[98] M. Giroud, H. Courtois, K. Hasselbach, D. Mailly and B. Pannetier, Superconducting proximity effect in a mesoscopic ferromagnetic wire, *Phys. Rev. B* **58**, R11872 (1998)

[99] V. T. Petrashov, I. A. Sosnin, I. Cox, A. Parsons and C. Troadec, Giant Mutual Proximity Effects in Ferromagnetic/Superconducting Nanostructures, *Phys. Rev. Lett.* **83**, 3281 (1999)

[100] J. Wang, M. Singh, M. Tian, N. Kumar, B. Liu et al., Interplay between superconductivity and ferromagnetism in crystalline nanowires, *Nature Physics* **6**, 389 (2010)

[101] R. S. Keizer, S. T. B. Goennenwein, T. M. Klapwijk, G. Miao, G. Xiao et al., A spin triplet supercurrent through the half-metallic ferromagnet CrO_2, *Nature* **439**, 825 (2006)

[102] T. S. Khaire, M. A. Khasawneh, W. P. Pratt and N. O. Birge, Observation of Spin-Triplet Superconductivity in Co-Based Josephson Junctions, *Phys. Rev. Lett.* **104**, 137002 (2010)

[103] D. Sprungmann, K. Westerholt, H. Zabel, M. Weides and H. Kohlstedt, Evidence for triplet superconductivity in Josephson junctions with barriers of the ferromagnetic Heusler alloy Cu_2MnAl, *Phys. Rev. B* **82**, 060505 (2010)

[104] M. S. Anwar, M. Veldhorst, A. Brinkman and J. Aarts, Long range supercurrents in ferromagnetic CrO_2 using a multilayer contact structure, *Applied Physics Letters* **100**, 052602 (2012)

[105] C. Klose, T. S. Khaire, Y. Wang, W. P. Pratt, N. O. Birge et al., Optimization of Spin-Triplet Supercurrent in Ferromagnetic Josephson Junctions, *Phys. Rev. Lett.* **108**, 127002 (2012)

[106] E. Gingrich, P. Quarterman, Y. Wang, R. Loloee, W. Pratt Jr et al., Spin-triplet supercurrent in Co/Ni multilayer Josephson junctions with perpendicular anisotropy, *Phys. Rev. B* **86**, 224506 (2012)

[107] W. Martinez, J. Pratt and N. O. Birge, Amplitude control of spin-triplet supercurrent in S/F/S Josephson junctions, *arXiv:1510.02144 [cond-mat]* (2015), arXiv: 1510.02144

[108] J. D. S. Witt, T. P. A. Hase, R. Fan, C. J. Kinane, T. R. Charlton et al., Strain dependent selection of spin-slip phases in sputter deposited thin-film epitaxial holmium, *J. Phys.: Condens. Matter* **23**, 416006 (2011)

[109] J. W. A. Robinson, F. Chiodi, M. Egilmez, G. B. Halász and M. G. Blamire, Supercurrent enhancement in Bloch domain walls, *Scientific Reports* **2** (2012)

[110] J. W. A. Robinson, N. Banerjee and M. G. Blamire, Triplet pair correlations and non-monotonic supercurrent decay with Cr thickness in Nb/Cr/Fe/Nb Josephson devices, *Phys. Rev. B* **89**, 104505 (2014)

[111] N. Banerjee, J. W. A. Robinson and M. G. Blamire, Reversible control of spin-polarized supercurrents in ferromagnetic Josephson junctions, *Nat. Commun.* **5** (2014)

[112] A. F. Volkov and K. B. Efetov, Proximity Effect and Its Enhancement by Ferromagnetism in High-Temperature Superconductor-Ferromagnet Structures, *Phys. Rev. Lett.* **102**, 077002 (2009)

[113] V. Peña, Z. Sefrioui, D. Arias, C. Leon, J. Santamaria et al., Coupling of superconductors through a half-metallic ferromagnet: Evidence for a long-range proximity effect, *Phys. Rev. B* **69**, 224502 (2004)

[114] Z. Sefrioui, D. Arias, V. Peña, J. E. Villegas, M. Varela et al., Ferromagnetic/superconducting proximity effect in $La_{0.7}Ca_{0.3}MnO_3/YBa_2Cu_3O_{7-\delta}$ superlattices, *Phys. Rev. B* **67**, 214511 (2003)

[115] Y. Kalcheim, I. Felner, O. Millo, T. Kirzhner, G. Koren et al., Magnetic field dependence of the proximity-induced triplet superconductivity at ferromagnet/superconductor interfaces, *Phys. Rev. B* **89**, 180506 (2014)

[116] Y. N. Khaydukov, G. A. Ovsyannikov, A. E. Sheyerman, K. Y. Constantinian, L. Mustafa et al., Evidence for spin-triplet superconducting correlations in metal-oxide heterostructures with noncollinear magnetization, *Phys. Rev. B* **90**, 035130 (2014)

[117] M. S. Anwar, Y. J. Shin, S. R. Lee, S. Yonezawa, T. W. Noh et al., Prototype hybrid of a ferromagnet and a spin triplet superconductor, *arXiv:1403.0345 [cond-mat]* (2014)

[118] L. R. Tagirov, Low-Field Superconducting Spin Switch Based on a Superconductor /Ferromagnet Multilayer, *Phys. Rev. Lett.* **83**, 2058 (1999)

[119] A. I. Buzdin, A. V. Vedyayev and N. V. Ryzhanova, Spin-orientation–dependent superconductivity in F/S/F structures, *EPL* **48**, 686 (1999)

[120] I. Baladié and A. Buzdin, Local quasiparticle density of states in ferromagnet/superconductor nanostructures, *Phys. Rev. B* **64**, 224514 (2001)

[121] J. Y. Gu, C.-Y. You, J. S. Jiang, J. Pearson, Y. B. Bazaliy et al., Magnetization-Orientation Dependence of the Superconducting Transition Temperature in the Ferromagnet-Superconductor-Ferromagnet System: CuNi/Nb/CuNi, *Phys. Rev. Lett.* **89**, 267001 (2002)

[122] A. Potenza and C. H. Marrows, Superconductor-ferromagnet CuNi/Nb/CuNi trilayers as superconducting spin-valve core structures, *Phys. Rev. B* **71**, 180503 (2005)

[123] K. Westerholt, D. Sprungmann, H. Zabel, R. Brucas, B. Hjörvarsson et al., Superconducting Spin Valve Effect of a V Layer Coupled to an Antiferromagnetic [Fe/V] Superlattice, *Phys. Rev. Lett.* **95**, 097003 (2005)

[124] R. Steiner and P. Ziemann, Magnetic switching of the superconducting transition temperature in layered ferromagnetic/superconducting hybrids: Spin switch versus stray field effects, *Phys. Rev. B* **74**, 094504 (2006)

[125] A. Singh, C. Sürgers and H. v. Löhneysen, Superconducting spin switch with perpendicular magnetic anisotropy, *Phys. Rev. B* **75**, 024513 (2007)

[126] G. Nowak, H. Zabel, K. Westerholt, I. Garifullin, M. Marcellini et al., Superconducting spin valves based on epitaxial Fe/V superlattices, *Phys. Rev. B* **78**, 134520 (2008)

[127] A. Y. Rusanov, S. Habraken and J. Aarts, Inverse spin switch effects in ferromagnet-superconductor-ferromagnet trilayers with strong ferromagnets, *Phys. Rev. B* **73**, 060505 (2006)

[128] P. V. Leksin and R. I. Salikhov, Observation of the “inverse" spin valve effect in a Ni/V/Ni trilayer system, *JETP Lett.* **90**, 59 (2012)

[129] N. Banerjee, C. B. Smiet, R. G. J. Smits, A. Ozaeta, F. S. Bergeret et al., Evidence for spin selectivity of triplet pairs in superconducting spin valves, *Nat. Commun.* **5** (2014)

[130] S. Takahashi, H. Imamura and S. Maekawa, Spin Imbalance and Magnetoresistance in Ferromagnet/Superconductor/Ferromagnet Double Tunnel Junctions, *Phys. Rev. Lett.* **82**, 3911 (1999)

[131] P. Leksin, N. Garif'yanov, I. Garifullin, J. Schumann, H. Vinzelberg et al., Full spin switch effect for the superconducting current in a superconductor/ferromagnet thin film heterostructure, *Applied Physics Letters* **97**, 102505 (2010)

[132] P. V. Leksin, N. N. Garif'yanov, I. A. Garifullin, J. Schumann, V. Kataev et al., Physical properties of the superconducting spin-valve Fe/Cu/Fe/In heterostructure, *Phys. Rev. B* **85**, 024502 (2012)

[133] B. Li, N. Roschewsky, B. A. Assaf, M. Eich, M. Epstein-Martin et al., Superconducting Spin Switch with Infinite Magnetoresistance Induced by an Internal Exchange Field, *Phys. Rev. Lett.* **110**, 097001 (2013)

[134] Y. Gu, G. Halász, J. Robinson and M. Blamire, Large Superconducting Spin Valve Effect and Ultrasmall Exchange Splitting in Epitaxial Rare-Earth-Niobium Trilayers, *Phys. Rev. Lett.* **115**, 067201 (2015)

[135] S. V. Mironov and A. Buzdin, Standard, inverse, and triplet spin-valve effects in $F_1/S/F_2$ systems, *Phys. Rev. B* **89**, 144505 (2014)

[136] P. Leksin, A. Kamashev, N. Garif'yanov, I. Garifullin, Y. V. Fominov et al., Peculiarities of performance of the spin valve for the superconducting current, *JETP lett.* **97**, 478 (2013)

[137] P. V. Leksin, A. A. Kamashev, J. Schumann, V. Kataev, J. Thomas et al., Boosting the superconducting spin valve effect in a metallic superconductor/ferromagnet heterostructure, *arXiv:1510.04846 [cond-mat]* (2015), arXiv: 1510.04846

[138] Y. Khaydukov, R. Morari, O. Soltwedel, T. Keller, G. Christiani et al., Interfacial roughness and proximity effects in superconductor/ferromagnet CuNi/Nb heterostructures, *Journal of Applied Physics* **118**, 213905 (2015)

[139] P. V. Leksin, N. N. Garifyanov, A. A. Kamashev, A. A. Validov, Y. V. Fominov et al., "Isolation" of the proximity-induced triplet pairing channel in the superconductor/ferromagnet spin valve, *arXiv:1510.05392 [cond-mat]* (2015), arXiv: 1510.05392

[140] V. Zdravkov, D. Lenk, R. Morari, A. Ullrich, G. Obermeier et al., Memory effect and triplet pairing generation in the superconducting exchange biased $Co/CoO_x/Cu_{41}Ni_{59}/Nb/Cu_{41}Ni_{59}$ layered heterostructure, *Applied Physics Letters* **103**, 062604 (2013)

[141] A. Singh, S. Voltan, K. Lahabi and J. Aarts, Colossal proximity effect in a superconducting triplet spin valve based on the half-metallic ferromagnet CrO_2, *Phys. Rev. X* **5**, 021019 (2015)

[142] J. Zhu, I. N. Krivorotov, K. Halterman and O. T. Valls, Angular Dependence of the Superconducting Transition Temperature in Ferromagnet-Superconductor-Ferromagnet Trilayers, *Phys. Rev. Lett.* **105** (2010)

[143] L. Y. Zhu, Y. Liu, F. S. Bergeret, J. E. Pearson, S. G. E. te Velthuis et al., Unanticipated Proximity Behaviour in Ferromagnet-Superconductor Heterostructures with Controlled Magnetic Noncollinearity, *Phys. Rev. Lett.* **110**, 177001 (2013)

[144] T. Yokoyama, Y. Tanaka and A. Golubov, Manifestation of the odd-frequency spin-triplet pairing state in diffusive ferromagnet/superconductor junctions, *Phys. Rev. B* **75**, 134510 (2007)

[145] J. Linder, A. Sudbø, T. Yokoyama, R. Grein and M. Eschrig, Signature of odd-frequency pairing correlations induced by a magnetic interface, *Phys. Rev. B* **81**, 214504 (2010)

[146] M. Alidoust, K. Halterman and O. T. Valls, Zero-energy peak and triplet correlations in nanoscale superconductor/ferromagnet/ferromagnet spin valves, *Phys. Rev. B* **92**, 014508 (2015)

[147] C. Visani, Z. Sefrioui, J. Tornos, C. Leon, J. Briatico et al., Equal-spin Andreev reflection and long-range coherent transport in high-temperature superconductor/half-metallic ferromagnet junctions, *Nature Physics* **8**, 539 (2012)

[148] C. Visani, F. Cuellar, A. Pérez-Muñoz, Z. Sefrioui, C. León et al., Magnetic field influence on the proximity effect at $YBa_2Cu_3O_7/La_{2/3}Ca_{1/3}MnO_3$ superconductor/half-metal interfaces, *Phys. Rev. B* **92**, 014519 (2015)

[149] G. Koren and T. Kirzhner, Zero-energy bound states in tunneling conductance spectra at the interface of an *s*-wave superconductor and a topological insulator in NbN/Bi_2Se_3/Au thin-film junctions, *Phys. Rev. B* **86**, 144508 (2012)

[150] G. Koren, T. Kirzhner, Y. Kalcheim and O. Millo, Signature of proximity-induced $p_x + ip_y$ triplet pairing in the doped topological insulator Bi_2Se_3 by the *s*-wave superconductor NbN, *EPL* **103**, 67010 (2013)

[151] A. Di Bernardo, S. Diesch, Y. Gu, J. Linder, G. Divitini et al., Signature of magnetic-dependent gapless odd frequency states at superconductor/ferromagnet interfaces, *Nat. Commun.* **6** (2015)

[152] H. F. Hess, R. B. Robinson, R. C. Dynes, J. M. Valles and J. V. Waszczak, Scanning-tunneling-microscope observation of the abrikosov flux lattice and the density of states near and inside a fluxoid, *Phys. Rev. Lett.* **62**, 214 (1989)

[153] H. F. Hess, R. B. Robinson and J. V. Waszczak, Vortex-core structure observed with a scanning tunneling microscope, *Phys. Rev. Lett.* **64**, 2711 (1990)

[154] J. D. Shore, M. Huang, A. T. Dorsey and J. P. Sethna, Density of states in a vortex core and the zero-bias tunneling peak, *Phys. Rev. Lett.* **62**, 3089 (1989)

[155] G. Xin-Xin, Z. He-Xin, X. Peng-Chao, Y. Di, Z. Kai et al., Possible *p*-wave superconductivity in epitaxial Bi/Ni bilayers, *Chinese Physics Letters* **32**, 067402 (2015)

[156] J. Moodera and R. Meservey, Superconducting phases of Bi and Ga induced by deposition on a Ni sublayer, *Phys. Rev. B* **42**, 179 (1990)

[157] P. LeClair, J. Moodera, J. Philip and D. Heiman, Coexistence of ferromagnetism and superconductivity in Ni/Bi bilayers, *Phys. Rev. Lett.* **94**, 037006 (2005)

[158] V. Siva, P. C. Pradhan, G. S. Babu, M. Nayak, P. K. Sahoo et al., Superconducting proximity effect in $NiBi_3$-Ni-$NiBi_3$ trilayer system with sharp superconductor-ferromagnet boundaries, *Journal of Applied Physics* **119**, 063902 (2016)

[159] J. D. S. Witt, *Superconductivity and Non-homogeneous Magnetism*, Ph.D. thesis, Department of Materials Science and Metallurgy, University of Cambridge (2012)

[160] F. Chiodi, J. D. S. Witt, R. G. J. Smits, L. Qu, G. B. Halász et al., Supra-oscillatory critical temperature dependence of Nb-Ho bilayers, *EPL* **101**, 37002 (2013)

[161] S. A. Kivelson and D. S. Rokhsar, Bogoliubov quasiparticles, spinons, and spin-charge decoupling in superconductors, *Phys. Rev. B* **41**, 11693 (1990)

[162] T. Yamashita, S. Takahashi, H. Imamura and S. Maekawa, Spin transport and relaxation in superconductors, *Phys. Rev. B* **65**, 172509 (2002)

[163] J. P. Morten, A. Brataas and W. Belzig, Spin transport in diffusive superconductors, *Phys. Rev. B* **70**, 212508 (2004)

[164] F. Giazotto and F. Taddei, Superconductors as spin sources for spintronics, *Phys. Rev. B* **77**, 132501 (2008)

[165] E. Zhao and J. A. Sauls, Theory of nonequilibrium spin transport and spin-transfer torque in superconducting-ferromagnetic nanostructures, *Phys. Rev. B* **78**, 174511 (2008)

[166] T. Yokoyama and Y. Tserkovnyak, Tuning odd triplet superconductivity by spin pumping, *Phys. Rev. B* **80**, 104416 (2009)

[167] H. Yang, S.-H. Yang, S. Takahashi, S. Maekawa and S. S. P. Parkin, Extremely long quasiparticle spin lifetimes in superconducting aluminium using MgO tunnel spin injectors, *Nat. Mater.* **9**, 586 (2010)

[168] F. Hübler, M. J. Wolf, D. Beckmann and H. v. Löhneysen, Long-Range Spin-Polarized Quasiparticle Transport in Mesoscopic Al Superconductors with a Zeeman Splitting, *Phys. Rev. Lett.* **109**, 207001 (2012)

[169] N. Poli, J. P. Morten, M. Urech, A. Brataas, D. B. Haviland et al., Spin Injection and Relaxation in a Mesoscopic Superconductor, *Phys. Rev. Lett.* **100**, 136601 (2008)

[170] T. Wakamura, N. Hasegawa, K. Ohnishi, Y. Niimi and Y. Otani, Spin Injection into a Superconductor with Strong Spin-Orbit Coupling, *Phys. Rev. Lett.* **112**, 036602 (2014)

[171] L. Y. Zhu, T. Y. Chen and C. L. Chien, Altering the Superconductor Transition Temperature by Domain-Wall Arrangements in Hybrid Ferromagnet-Superconductor Structures, *Phys. Rev. Lett.* **101**, 017004 (2008)

[172] A. Y. Rusanov, M. Hesselberth, J. Aarts and A. I. Buzdin, Enhancement of the Superconducting Transition Temperature in Nb/Permalloy Bilayers by Controlling the Domain State of the Ferromagnet, *Phys. Rev. Lett.* **93**, 057002 (2004)

[173] M. Flokstra and J. Aarts, Domain-wall enhancement of superconductivity in superconductor/ferromagnet hybrids: Case of weak ferromagnets, *Phys. Rev. B* **80**, 144513 (2009)

[174] J. Fritzsche, R. B. G. Kramer and V. V. Moshchalkov, Visualization of the vortex-mediated pinning of ferromagnetic domains in superconductor-ferromagnet hybrids, *Phys. Rev. B* **79**, 132501 (2009)

[175] S. V. Dubonos, A. K. Geim, K. S. Novoselov and I. V. Grigorieva, Spontaneous magnetization changes and nonlocal effects in mesoscopic ferromagnet-superconductor structures, *Phys. Rev. B* **65**, 220513 (2002)

[176] C. Monton, F. de la Cruz and J. Guimpel, Magnetic state modification induced by superconducting response in ferromagnet/superconductor Nb/Co superlattices, *Phys. Rev. B* **77**, 104521 (2008)

[177] T. Tamegai, Y. Nakao, S. Mohan and Y. Nakajima, Experimental demonstration of shrinkage of magnetic domains in a superconductor/ferromagnet bilayer, *Superconductor Science and Technology* **24**, 024015 (2011)

[178] P. J. Curran, J. Kim, N. Satchell, J. D. S. Witt, G. Burnell et al., Irreversible magnetization switching at the onset of superconductivity in a superconductor ferromagnet hybrid, *Applied Physics Letters* **107**, 262602 (2015)

[179] N. A. of Sciences, *Biographical Memoirs V.70*, The National Academies Press, Washington, DC (1996)

[180] J. T. Batley, *Spin Transport in Lateral Spin Valves*, Ph.D. thesis, School of Physics and Astronomy, University of Leeds (2015)

[181] N. A. Porter, *Magnetoresistance in n-type Silicon*, Ph.D. thesis, School of Physics and Astronomy, University of Leeds (2010)

[182] S. Foner, Versatile and sensitive vibrating-sample magnetometer, *Review of Scientific Instruments* **30**, 548 (1959)

[183] M. A. Garcia, E. F. Pinel, J. de la Venta, A. Quesada, V. Bouzas et al., Sources of experimental errors in the observation of nanoscale magnetism, *Journal of Applied Physics* **105**, 013925 (2009)

[184] D. S. Sivia, *Elementary Scattering Theory: For X-ray and Neutron Users*, OUP Oxford (2011)

[185] P. Scherrer, Bestimmung der größe und der inneren struktur von kolloidteilchen mittels röntgenstrahlen, *Nachrichten von der Gesellschaft der Wissenschaften zu Göttingen, Mathematisch-Physikalische Klasse* **1918**, 98 (1918)

[186] J. I. Langford and A. J. C. Wilson, Scherrer after sixty years: a survey and some new results in the determination of crystallite size, *Journal of Applied Crystallography* **11**, 102 (1978)

[187] H. Kiessig, Interferenz von Röntgenstrahlen an dünnen Schichten, *Ann Phys* **10**, 769 (1931)

[188] S. J. Blundell and J. A. C. Bland, Polarized neutron reflection as a probe of magnetic films and multilayers, *Phys. Rev. B* **46**, 3391 (1992)

[189] C. Majkrzak, Neutron scattering studies of magnetic thin films and multilayers, *Physica B: Condensed Matter* **221**, 342 (1996)

[190] M. R. Fitzsimmons, S. Bader, J. Borchers, G. Felcher, J. Furdyna et al., Neutron scattering studies of nanomagnetism and artificially structured materials, *Journal of Magnetism and Magnetic Materials* **271**, 103 (2004)

[191] H. Zabel, Neutron reflectivity of spintronic materials, *Materials Today* **9**, 42 (2006)

[192] F. Ott, Neutron scattering on magnetic surfaces, *Comptes Rendus Physique* **8**, 763 (2007)

[193] C. J. Kinane, *The interplay of Magnetism and Structure in Patterned Multilayer Thin Films*, Ph.D. thesis, School of Physics and Astronomy, University of Leeds (2008)

[194] M. Björck and G. Andersson, GenX: an extensible X-ray reflectivity refinement program utilizing differential evolution, *Journal of Applied Crystallography* **40**, 1174 (2007)

[195] M. Björck, Fitting with differential evolution: an introduction and evaluation, *Journal of Applied Crystallography* **44**, 1198 (2011)

[196] V. F. Sears, Neutron scattering lengths and cross sections, *Neutron news* **3**, 26 (1992)

[197] B. L. Henke, E. M. Gullikson and J. C. Davis, X-ray interactions: photoabsorption, scattering, transmission, and reflection at E= 50-30,000 ev, Z= 1-92, *Atomic data and nuclear data tables* **54**, 181 (1993)

[198] J. Als-Nielsen and D. McMorrow, *Elements of modern X-ray physics*, John Wiley & Sons (2011)

[199] L. Nevot and P. Croce, Caractérisation des surfaces par réflexion rasante de rayons X. Application à l'étude du polissage de quelques verres silicates, *Revue de Physique appliquée* **15**, 761 (1980)

[200] S. J. Blundell, Spin-polarized muons in condensed matter physics, *Contemporary Physics* **40**, 175 (1999)

[201] P. Bakule and E. Morenzoni, Generation and applications of slow polarized muons, *Contemporary Physics* **45**, 203 (2004)

[202] W. H. Press, *Numerical recipes 3rd edition: The art of scientific computing*, Cambridge university press (2007)

[203] M. G. Flokstra et al., *Proximity effects in superconducting spin-valve structures*, Ph.D. thesis, Faculty of Science, Leiden University (2010)

[204] A. J. Drew, M. W. Wisemayer, D. O. G. Heron, S. Lister, S. L. Lee et al., Using spin-polarized neutron reflectivity to probe mesoscopic vortex states in a Pb thin-film superconductor, *Phys. Rev. B* **80**, 134510 (2009)

[205] O. Wessely, B. Skubic and L. Nordström, Current Driven Magnetization Dynamics in Helical Spin Density Waves, *Phys. Rev. Lett.* **96**, 256601 (2006)

[206] M. A. Ruderman and C. Kittel, Indirect exchange coupling of nuclear magnetic moments by conduction electrons, *Physical Review* **96**, 99 (1954)

[207] T. Kasuya, A theory of metallic ferro-and antiferromagnetism on zener's model, *Progress of theoretical physics* **16**, 45 (1956)

[208] K. Yosida, Magnetic properties of Cu-Mn alloys, *Physical Review* **106**, 893 (1957)

[209] R. A. Cowley and J. Jensen, Magnetic structures and interactions in erbium, *J. Phys.: Condens. Matter* **4**, 9673 (1992)

[210] J. W. Cable, E. O. Wollan, W. C. Koehler and M. K. Wilkinson, Magnetic Structures of Metallic Erbium, *Phys. Rev.* **140**, A1896 (1965)

[211] M. Habenschuss, C. Stassis, S. K. Sinha, H. W. Deckman and F. H. Spedding, Neutron diffraction study of the magnetic structure of erbium, *Phys. Rev. B* **10**, 1020 (1974)

[212] D. Gibbs, J. Bohr, J. D. Axe, D. E. Moncton and K. L. D'Amico, Magnetic structure of erbium, *Phys. Rev. B* **34**, 8182 (1986)

[213] H. Lin, M. F. Collins, T. M. Holden and W. Wei, Magnetic structure of erbium, *Phys. Rev. B* **45**, 12873 (1992)

[214] D. A. Jehan, D. F. McMorrow, J. A. Simpson, R. A. Cowley, P. P. Swaddling et al., Collapsing cycloidal structures in the magnetic phase diagram of erbium, *Phys. Rev. B* **50**, 3085 (1994)

[215] B. Watson and N. Ali, Magnetic transitions in single-crystal erbium, *J. Phys.: Condens. Matter* **7**, 4713 (1995)

[216] B. Watson and N. Ali, The b-axis magnetic phase diagram of erbium, *J. Phys.: Condens. Matter* **8**, 1797 (1996)

[217] B. H. Frazer, J. R. Gebhardt and N. Ali, Magnetic phase diagrams of erbium, *Journal of Applied Physics* **85**, 6100 (1999)

[218] J. Borchers, M. Salamon, R. Erwin, J. Rhyne, R. Du et al., Structural and magnetic properties of Er thin films and Er/Y superlattices: Magnetoelastic effects, *Phys. Rev. B* **43**, 3123 (1991)

[219] J. Borchers, M. Salamon, R. Erwin, J. Rhyne, G. Nieuwenhuys et al., Structural and magnetic properties of Er thin films and Er/Y superlattices. II. Modification of the commensurate spin states, *Phys. Rev. B* **44**, 11814 (1991)

[220] H. Savaloni and M. A. Player, Influence of deposition conditions and of substrate on the structure of uhv deposited erbium films, *Vacuum* **46**, 167 (1995)

[221] G. Helgesen, M. Conover, D. Gibbs and C. Flynn, Magnetic and structural measurements of lattice-matched erbium films on sapphire 110 and 001 substrates, *Journal of Magnetism and Magnetic Materials* **192**, 11 (1999)

[222] J. Kwo, M. Hong and S. Nakahara, Growth of rare-earth single crystals by molecular beam epitaxy: The epitaxial relationship between hcp rare earth and bcc niobium, *Applied Physics Letters* **49**, 319 (1986)

[223] O. leybold vacuum, *Fundamentals of Vacuum Technology*, Oerlikon Leybold Vacuum, 1st edition edition (2007)

[224] F. Herman and R. Schrieffer, Generalized Ruderman-Kittel-Kasuya-Yosida theory of oscillatory exchange coupling in magnetic multilayers, *Phys. Rev. B* **46**, 5806 (1992)

[225] D. M. Deaven, D. S. Rokhsar and M. Johnson, Simple theory of exchange coupling in transition-metal magnetic multilayers, *Phys. Rev. B* **44**, 5977 (1991)

[226] C. Chappert and J. P. Renard, Long-period oscillating interactions between ferromagnetic layers separated by a nonmagnetic metal: a simple physical picture, *EPL (Europhysics Letters)* **15**, 553 (1991)

[227] P. Bruno and C. Chappert, Oscillatory coupling between ferromagnetic layers separated by a nonmagnetic metal spacer, *Phys. Rev. Lett.* **67**, 1602 (1991)

[228] R. Coehoorn, Period of oscillatory exchange interactions in Co/Cu and Fe/Cu multilayer systems, *Phys. Rev. B* **44**, 9331 (1991)

[229] J. D. S. Witt, J. F. K. Cooper, N. Satchell, C. J. Kinane, P. J. Curran et al., Magnetic phases of sputter deposited thin-film erbium, *Submitted to Scientific Reports* (2016)

[230] Y. Gu, J. W. A. Robinson, M. Bianchetti, N. A. Stelmashenko, D. Astill et al., Magnetic state controllable critical temperature in epitaxial Ho/Nb bilayers, *APL Materials* **2**, 046103 (2014)

[231] M. G. Flokstra, N. Satchell, J. Kim, G. Burnell, P. J. Curran et al., Remotely induced magnetism in a normal metal using a superconducting spin-valve, *Nature Physics* **12**, 57 (2016)

[232] T. Noh, M. Houzet, J. S. Meyer and V. Chandrasekhar, Nonlocal spin correlations mediated by a superconductor, *Phys. Rev. B* **87**, 220502 (2013)

[233] R. Grein, M. Eschrig, G. Metalidis and G. Schön, Spin-Dependent Cooper Pair Phase and Pure Spin Supercurrents in Strongly Polarized Ferromagnets, *Phys. Rev. Lett.* **102**, 227005 (2009)

[234] M. Alidoust, J. Linder, G. Rashedi, T. Yokoyama and A. Sudbø, Spin-polarized Josephson current in superconductor/ferromagnet/superconductor junctions with inhomogeneous magnetization, *Phys. Rev. B* **81**, 014512 (2010)

[235] H. Stalzer, A. Cosceev, C. Sürgers and H. v. Löhneysen, Field-screening properties of proximity-coupled Nb/Ag double layers, *EPL (Europhysics Letters)* **76**, 121 (2006)

[236] Y. Oda and H. Nagano, Meissner effect in Cu of thick Cu clad Nb, *Solid State Communications* **35**, 631 (1980)

[237] O. Narikiyo and H. Fukuyama, Proximity induced meissner effect in dirty normal metals, *Journal of the Physical Society of Japan* **58**, 4557 (1989)

[238] S. Higashitani and K. Nagai, Meissner effect in normal-superconducting proximity-contact double layers, *Journal of the Physical Society of Japan* **64**, 549 (1995)

[239] W. Belzig, C. Bruder and G. Schön, Diamagnetic response of normal-metal–superconductor double layers, *Phys. Rev. B* **53**, 5727 (1996)

[240] W. Belzig, C. Bruder and A. L. Fauchère, Diamagnetic response of a normal-metal–superconductor proximity system at arbitrary impurity concentration, *Phys. Rev. B* **58**, 14531 (1998)

[241] J. Kim, Y.-J. Doh, K. Char, H. Doh and H.-Y. Choi, Proximity effect in Nb/Au/CoFe trilayers, *Phys. Rev. B* **71**, 214519 (2005)

[242] H. Yamazaki, N. Shannon and H. Takagi, Superconducting proximity effect in epitaxial Nb (110)/Au (111)/Nb (110) trilayers, *arXiv preprint arXiv:1602.05790* (2016)